Effect of Magnetic Shear and Heating on Electromagnetic Micro-instability and Turbulent Transport in Global Toroidal System(Dissertation_全文)

AUTHOR(S):

Qin, Zhihao

Effect of Magnetic Shear and Heating on Electromagnetic Micro-instability and Turbulent Transport in Global Toroidal System

大域的トロイダル系における電磁的な微視的不安定性と乱流輸送に対する磁気シアと加熱の効果

ZHIHAO QIN
秦　志豪

Acknowledgments

Firstly, I would like to express all my gratitude to my supervisor Prof. Yasuaki Kishimoto and Prof. Kenji Imadera for their continuous encouragement and guide of my research to the proper direction for five years in Kyoto University. The path towards the completion of this PhD was long and full of uncertainties but their advice and support helped me find my way. This thesis would be never completed without their help.

I would like to appreciate Prof. Jiquan Li and and Prof. Ishizawa for their continuous support over five years. In the course of this work, they provided me a constant source of advice and encouragement. My sincere thanks also go to Ms. Takahashi and R.Matsui for helping me a lot making sense of Japan and understanding everyday life in this country. I would also like to thank Wei Wang for his variable discussion and comments in numerical simulation.

More generally, I would like to thank all the members of Kishimoto laboratory who I had the opportunity to meet over the years. Although I was not the most social member of the lab, I really enjoyed the atmosphere and had many great conversations there.

Abstract

Transport barriers (TBs) characterized by a steep pressure gradient is widely recognized as contribution to suppress anomalous transport driven by various types of micro-instabilities. What has been observed in many experiments is that auxiliary heating is benefit for building the Internal Transport Barrier (ITB). However, the auxiliary heating also feeds some micro-instabilities which could lead ITB collapse in turn. On the other hand, the safety factor profile with a negative shear or weak positive shear also plays a important role for the formation of ITB. We investigated the behavior of the dominant micro-instabilities in presence of the auxiliary heating and/or flat q-profile by means of gyro-kinetic global simulation.

The simulations using the experimental profiles (density, temperature ,safety factor) present a new type of density gradient driven drift mode which is expected to be responsible for the collapse of ion-ITB, which real frequency is low and changes the sign from electron diamagnetic direction to that of ion continuously as the poloidal wavenumber increases. Collisionless is acceptable widely in high temperature thermonuclear fusion plasma. Therefore, the particle distribution in $v_{\parallel}$ is different from that in $v_{\perp}$, but we assume that the particle distribution still subjects to thermodynamic equilibrium distribution. For describing this anisotropy, we introduce two temperatures, $T_{\parallel}$ and another is $T_{\perp}$, into physical model of Gyro-kinetic based Numerical Experiment of Tokamaks (GKNET). The instability is found to be sensitive to the perpendicular ion/electron temperature $T_{i,e_{\perp}}$. It is excited by the increasing $T_{e_{\perp}}$ and suppressed by the increasing $T_{i_{\perp}}$. Further, like the ion temperature gradient mode, this kind of low frequency instability presents a potential changing into the kinetic ballooning mode with electromagnetic perturbation being taken into account. What could be acceptable is that: the presented low frequency instability was suppressed by neutral beams injection. This suppression is helpful to build the ITB. But the more powerful electron cyclotron resonance heating enhanced the instability even the neutral beams injection. was being kept. This change made the ITB to be collapsed.

In the case of nearly flat safety factor profile, we study linear micro-instability and non-linear evolution in high-β plasmas. We found that an infernal type of mode is induced at the radial location of the maximum pressure gradient. However, the linear dispersion, i.e., eigen frequency and linear growth rate, and also nonlinear turbulent

spectrum exhibit hardly deterministic complex corrugated structure with respect to consecutive toroidal mode number n. Furthermore, the turbulence is dominated by a large-scale structure corresponding to lower toroidal mode numbers causing large heat and particle fluxes. For explaining such complex behaviors for plasmas with a flat safety factor profile, we study the mechanism under the hypothesis that the instability strength is regulated by the resonance mismatch $\Delta\mu \equiv M_\theta - nq_c$ with M_θ the dominat poloidal mode number and present a law prescribing the linear dispersion by rearranging consecutive toroidal mode number n to a set of plural discrete dispersion groups regulated by an arithmetic progression which commom difference is evaluated from the non-integer residual of the constant safety factor value q_c, i.e. $\delta q_\mu = q_c - \mathrm{int}(q_c)$. Through this procedure, a corrugated structure of the dispersion is found to be disappeared in each group exhibiting smooth function including secondary unstable modes. Such a discrete dispersion regrouped by an arithmetic progression with respect to toroidal mode number causes a new class of turbulence due to selective and directional energy flows across different groups. It is interesting to note that the turbulent energy is condensed to the lowest mode number in a specific group, which exhibits quasi-coherent homogenized structures leading to larger fluxes.

Contents

1 Introduction

1.1 World energy scenario and role of fusion

Humans are always in pursuit of a better quality of life which can be measured by the Human Development Index (HDI) based on various reports by the United Nations Development Programme (UNDP) [1]. The HDI is found to be correlated with the per capita use of energy as shown in Fig 1-1 [2]. The relationship shows the evidence of saturation which means the further improvements in HDI require much more energy consumption at the expense. How are we going to produce such vast amount of energy it needs? In the absence of new developments, the workhorse is likely to be based on fossil fuels. However, the fossil fuel reserves have started depleting. There are several political and military conflicts for control of oil and gas over the last decades. On the other hand, the use of fossil fuels as the major source of energy has emitted a lot of greenhouse gases which is considered to lead to significant global warming. Massive use of coal also causes serious air pollution, particularly China, which is suffering. In order to reduce greenhouse gas emissions, electrification reforms have been initiated on the consumer side, such as vehicle. This drives electricity demand further increase.

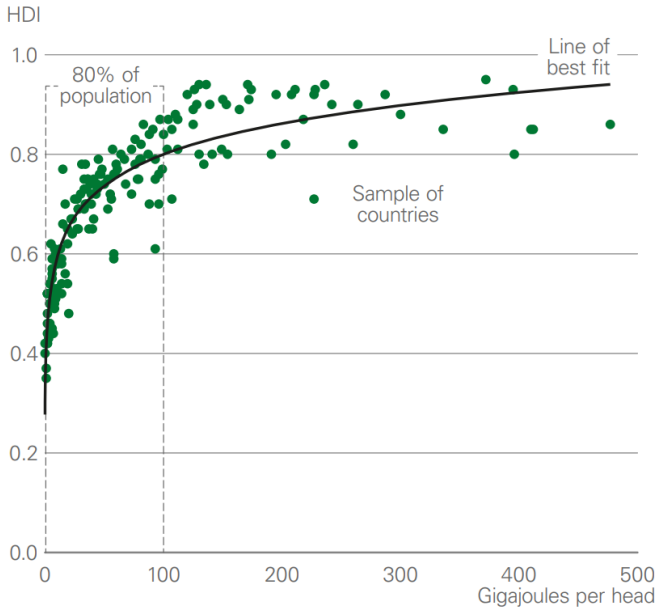

Fig. 1-1 Human Development [1].

There are several ways for producing electricity without greenhouse gas

emissions like the conventional hydroelectric power plant, the nuclear fission, some kinds of renewable energy sources – for the most part solar panels and wind turbines. But they all have disadvantages that cannot be ignored. As for the nuclear fission, although it plays an important supportive role (or even dominant role in countries such as France), as well-known that we have faced serious public opposition because of concerns of proliferation, radioactive hazardous wastes. In particular since the tragic 2010 Fukushima incident, the share of nuclear fission power generation has decreased significantly. The renewable energies have the potential of a major energy source. Before that, we have to address issues of energy density, efficiency and cost of production. In addition, their irregularity is a serious threat to the stability of the power grid system, especially after its share increases. Thus, we are at a critical juncture today, when we have to quickly develop a viable alternative source of energy which is clean, safe and virtually unlimited that can lead to Sustainable Development Goals (SDGs) set up in 2015 by the United Nations General Assembly.

Tracing back to the energy we are using, even traditional fossil fuels, they are all come from sun. the difference is just the time that the solar, wind and hydroelectric power come from present sun while the fossil fuels store the energy that come from the past sun. The energy of sun is produced by nuclear fusion. In contrast to the renewables, its energy density satisfies the needs of urban industrial complexes. On the other hand, comparing with the nuclear fission, it has the prospect of considerably reduced long lived radioactive emission and inherent operational safety. Thus, fusion power will get much more public acceptance, or it is more likely that people are looking forward to its commercialize. The nuclear fusion is likely to give us a wonderful solution.

Our Sun is the brightest and natural example of fusion around us which has been burning for billions of years. The energy of fusion is produced by the difference in material mass before and after fusion. Specifically, the light elements are brought together so that fuse to form heavier elements. The resulting heavier elements have slightly less mass than the fusing elements. This mass difference results in the release of energy. The overall process of fusion within the Sun can be broken down into several simple 3 steps as follow: in the first stage two protons ^{1}H combine and one of them converts into a neutron to form a positron, an electronic neutrino, and a nucleus of the heavy isotope of hydrogen known as deuterium ^{2}D. The positron will annihilate with an electron from the environment into two gamma rays with 1.022MeV [3]. once this

initial step has occurred, the deuterium produced in the first step can fuse with another proton to produce the helium-3 ${}^{3}He$ nucleus. This process is due to it is mediated by the strong nuclear force rather than the weak force. Once the helium-3 ${}^{3}He$ has been produced, there are four possible paths to generate ${}^{4}He$. the most likely one in our Sun is shown in formula Eq. (1-1)

$$\begin{aligned} 2\,{}^{1}H &\rightarrow {}^{2}D + e^{+} + \nu_e + 0.42\text{MeV} \\ {}^{2}D + {}^{1}H &\rightarrow {}^{3}He + \gamma + 5.49\text{MeV} \\ 2\,{}^{3}H &\rightarrow {}^{4}He + 2\,{}^{1}H + 12.86\text{MeV} \end{aligned} \quad . \qquad (1\text{-}1)$$

For fusion to occur, the protons or nuclei must be heated to have very high kinetic energy enough to overcome the electrostatic repulsion and come close enough to the point where the nuclear force is working. For an example of deuterium and tritium nuclei, the temperature of the order of ~10 keV.

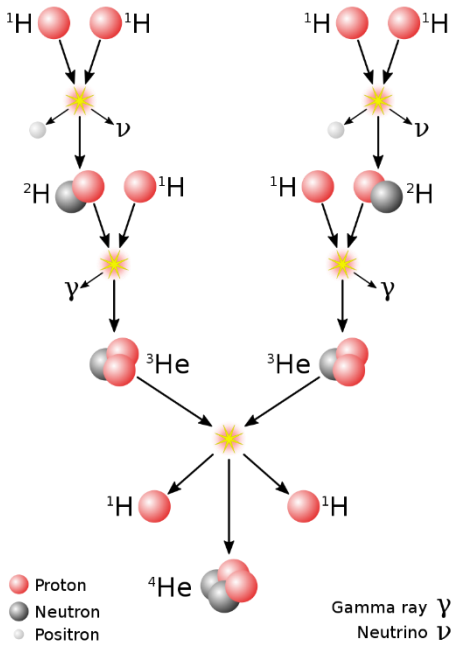

Fig. 1-2 The proton-proton chain reaction P-P I, which dominates in our Sun, turning 4 protons into a helium-4 nucleus and releasing energy. [Image credit: Adapted from Wikimedia Commons.]

It is true that nuclear fusion can yield tremendous energy, but its conditions are also extremely demanding. In the sun or starts, the tremendous gravity keeping the fusing protons together against the de-confining tendency due to thermal expansion. At the core, the crushing pressure and extreme temperatures and pressure are so strong that make them can overcome the electric repulsion and reach the fusion conditions. We

have achieved the uncontrolled fusion reactions in the form of explosions using deuterium and tritium, but the plasma is unconfined. The biggest challenge is achieving fusion in a controlled manner in a confined plasma on Earth.

1.2 Approaches to fusion

Given the extreme temperature of the fusion plasma, containment via physical contact is not possible with any know substance. On top of that, the natural condition of gravitational confinement in stars cannot be reproduced in laboratories. Thus, other means of confinement are necessary, and the two main approaches to achieve controlled fusion are inertial confinement and magnetic confinement.

1.2.1 Inertial confinement fusion

Inertial confinement fusion (ICF) is achieved by heating and compressing a small fuel pellet, typically composed of a deuterium-tritium mixture. Its original idea was derived from the working mechanism of a hydrogen bomb, which is an application of uncontrolled fusion. Within a hydrogen bomb, a fission bomb is placed to initiate fusion. The energy released in this so-called primary explosion is transferred to the fusion fuels via different mechanisms, among which x-ray heating is primary. The fusion fuel in the secondary section is rapidly heated, leading to an outward explosion. As every action has an equal but opposite reaction, the remaining fusion fuels are compressed inward, before reaching the temperature and density at which fusion reaction can occur. The fusion energy released is almost entirely shared between the product alpha particles and the product neutrons. The charged alpha particles interact with the high-density fusion fuels and quickly thermalize. The additional kinetic energy of the fast alpha particles heats up fusion fuels, sustaining the fusion reaction. Enormous energy is released in a hydrogen bomb explosion. However, it is demonstrated that power generation with hydrogen bomb explosions is not feasible. This is due to both the high cost of fission bomb production and a physical limit in the primary fission bomb size.

John Nuckolls explored the energy needed to trigger fusion in a scaled-down secondary. He discovered a minimum size of the order of milligram, where below this size the product alpha particles would escape before reaching thermal equilibrium. The energy to initiate fusion for this secondary is in the megajoule range, which is much lower even than the smallest fission bomb. Then, the remaining question is how to deliver energy to the secondary at a distance, and this brought the idea of a ‘driver’. In

general, a single laser is used whose beam is split. The split beams are all amplified by at least a trillion times. Mirrors are applied to direct the beams towards the target chamber. The target is heated and through a similar mechanism to the hydrogen bomb, the outer layer explodes with tremendous velocity. The remaining fusion materials are forced inward reaching huge density, around a thousand times the density of water. On top of that, shock waves from all directions enter the fusion fuel and when they meet at the center, the core density is brought up significantly such that fusion reaction takes place at a useful rate. The product alpha particles then heat up the fusion fuel, sustaining further reactions.

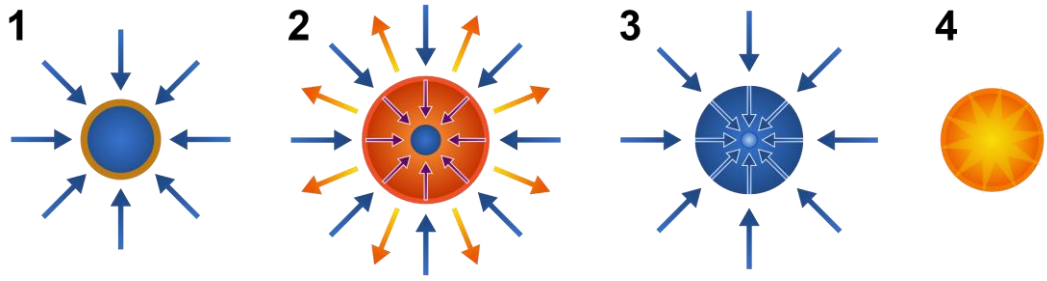

Fig. 1-3 Inertial confinement fusion explained in steps. 1. laser beam hits the outer laser of plasma; 2. explosion and implosion resulting in plasma density increase; 3. shock wave meets at plasma center leading to core density increase; 4. usion reaction takes place. [Image credit: Adapted from Wikimedia Commons.]

1.2.2 Magnetic confinement fusion

The other controlled fusion strategy is the magnetic confinement fusion. As the plasma is composed of charged particles that feel force in magnetic fields, by balancing the Lorentz force and pressure, confinement could be achieved. In contrast to the inertial confinement fusion whose development started in the 1970s, early magnetic confinement devices were built in the 1940s. A major research area in the early years was confinement through the magnetic mirror. A magnetic mirror is composed of a series of electromagnets which are configured so that when charged particles move away from the confinement area the strength of the magnetic field increases, forcing particles back to the confinement area. Although the magnetic mirror is leaky, meaning that only particles with a limited range of velocities are trapped, by continuously adding fusion fuels, the problem was expected to be overcome. However, it was later demonstrated that instability would develop in the region of the convex magnetic field. This so-called flute instability could be resolved by modifying the engineering design, but the theoretical thermal energy output barely compensates the electrical energy input

to run the electromagnets. In the 1970s, another design was suggested with a larger confinement area, thus in principle produces more energy. Based on this design, the construction of Mirror Fusion Test Facility (MFTF) was schedule. However, during the construction of MFTF, new findings showed that the performance goals could not be reached and the MFTF was modified the downgraded MFTF-B then quickly abandoned after completion. This brought fusion via magnetic mirror to a dead end [4].

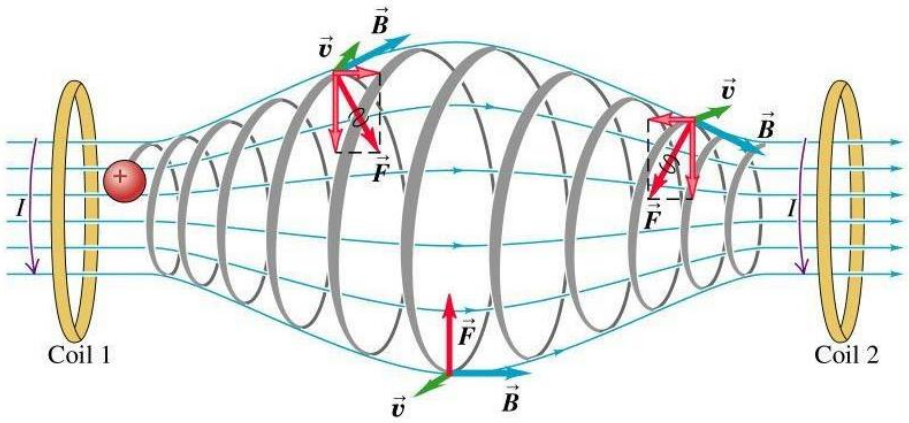

Fig. 1-4 Magnetic field within a magnetic mirror and the force exerted on plasma particles. Plasma particles not in the center of the confinement area with a non-zero horizontal velocity feels a restoring force. [Image credit: Adapted from Physics Forums.]

Another type of magnetic confinement fusion in the early stage of development is the z-pinch. A transformer is placed outside the plasma container to induce current. The induced plasma current gives rise to a magnetic field that pinch the plasma into a ring, thereby achieving confinement. By a combination of Ohmic heating and adiabatic heating, temperature could rise to the required range for fusion to take place. However, various instabilities were observed, notably the kink instability. Due to the kink instability, plasma hits the container wall before reaching the required temperature range. Even devices built based on the improved stabilized pinch design are susceptible to the instabilities, implying a doomed future of the z-pinch approach.

A stellarator is another type of confinement fusion device besides the magnetic mirror and the z-pinch. The early generations of stellarators were in the shape of '8' where a torus is divided in half and reconnected by straight crossover sections. The advantage of this design is that nuclei propagate from inside to outside, cancelling the

across-axis drift. Shortly after the construction of early stellarators, research demonstrated that in a circular arrangement, with the addition of a second set of magnets on each side, the same confinement effect could be achieved. This newer design has the merit of increasing shear, which suppresses the plasma turbulence. However, from the operation of large stellarators, degraded confinement than expectation was observed. In addition, the size of a stellarator power plant was calculated to be enormous, vastly increasing the construction difficulty. As a result, the research was halted until the turn of the second millennium. Stellarator regained focus as it is immune to several problems in tokamaks [5].

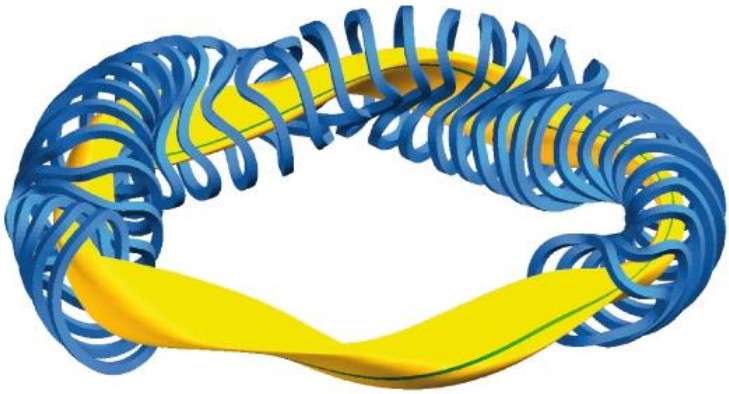

Fig. 1-5 Geometry of a circular stellarator . [Image credit: Max-Planck-Institut für Plasmaphysik.]

Moving on to the present, tokamak is the leading magnetic confinement machine. To understand the confining mechanism of a tokamak, first consider a solenoid which is the simplest confinement device. In a solenoid, charged particles gyrate around the magnetic lines. However, edge losses cannot be prevented. A natural idea is to bend the solenoid so that two ends connect. This solves the edge loss problem, but due to pure geometric reasons, the field on the inside is stronger than the field on the outside. Due to this asymmetry, particles drift and hit the container wall, ruining confinement. The solution is to introduce a poloidal field, in addition to the toroidal field which run around the torus. The resultant field line twist around the torus in a helical shape, such that the drift directions of particles when they are on the inside and outside are opposite, roughly cancelling out each other. This explains the basis working mechanism of a tokamak.

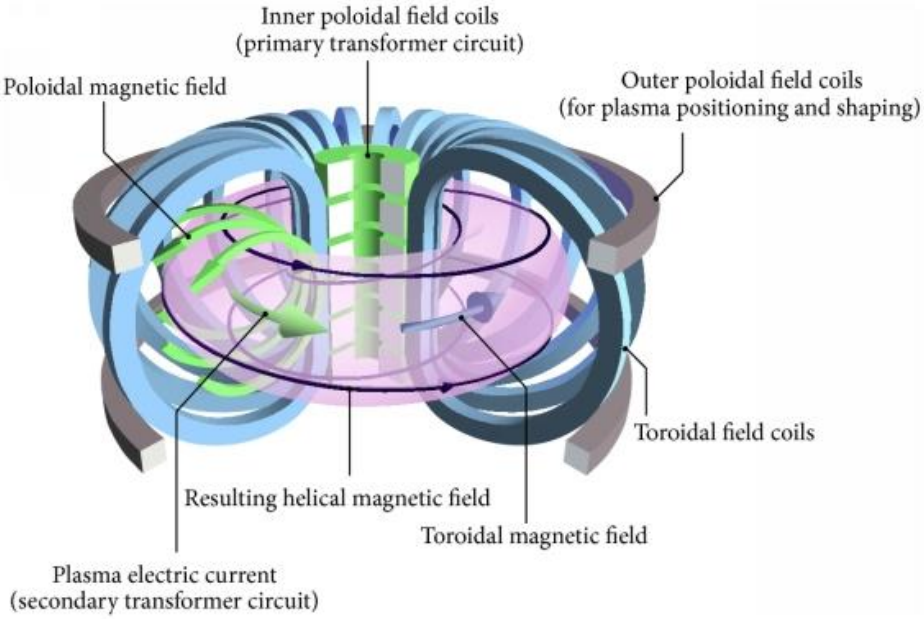

Fig. 1-6 The structure of a tokamak, with helical magnetic field lines. [Image credit: EUROFusion.]

The physical layout of a tokamak and a z-pinch is essentially the same. What differentiate tokamak from the z-pinch is the concept called safety factor. Safety factor describes the degree of twist of the magnetic lines. It is defined by the number of turns in the toroidal direction when the field line returns to its origin position in the poloidal direction. A device with a larger safety factor is shown to be more stable. Comparing to the earlier devices whose operational safety factor is around a third, in a tokamak this value is more than one, leading to an improvement in stability by a few orders of magnitude. The kink instability that plagued z-pinch is also strongly suppressed, allowing tokamak to operate with a higher plasma temperature.

The gain factor is an important measure as tokamaks are aimed to be used for power generation. One of the first goal is to achieve a gain factor of 1, or breakeven, where the thermal energy released is equal to the energy input to sustain fusion reaction going. After reaching this goal, the ultimate target is ignition, where fusion reaction could be self-sustained by the alpha particle heating alone. A series of facilities were built targeting breakeven, including Tokamak Fusion Test Reactor (TFTR) and Joint European Torus (JET), which keeps the record of fusion power output of 16MW. However, even these machines showed problems that limit their performance. To solve these new problems, a larger and more expensive machine has to be built which require

international cooperation. Following the agreement between the US and Soviet leaders in the year 1985, the construction of International Thermonuclear Experimental Reactor (ITER) was scheduled and it has since been the primary tokamak design effort.

1.2.3 Magnetic configuration of tokamak

Tokamak is a toroidal plasma confinement system. The plasma is confined by a magnetic field. The principal magnetic field is the toroidal field $\boldsymbol{B}_{\varphi}$. It is produced by currents in numerous toroidal field coils wrapped around the torus (light blue) as shown in Fig. 1-6. However, this field alone is not enough to confine the plasma. Because the charged particles suffer various types of drift velocity across magnetic field lines. The gradient and curvature of magnetic field will produce a drift velocity which are opposite between the electron and ion. Thereby, electrostatic field will be produced and leads a drift velocity outward as presented in Fig. 1-7 (a). In order to cancel this outward drift, a poloidal magnetic field $\boldsymbol{B}_{\theta}$ is added. Then, the total magnetic field become helical configuration which is enable the charged particles go through both inside and outside of torus. The drifts inside and outside cancel with each other. The poloidal magnetic field $\boldsymbol{B}_{\theta}$ is expected to be produced mainly by current in the plasma itself, so-called bootstrap current. Before that the poloidal magnetic field can be the central ohmic transformer (green) stands in the hole of the torus. When traversed by a variable electric current, a toroidal flow of charged particles is created in the plasma, in turn generating a poloidal magnetic field.

For axisymmetric configuration, that means magnetic field is independent of the toroidal angle φ. Thereby, the torus in Fig. 1-7 (a) can be stretched to a cylindrical configuration as shown in Fig. 1-7 (b). the magnetic field lines lie in the nested magnetic surface. It is important to note that normally the magnetic field on two surfaces are not parallel as the green lines and purple lines in Fig. 1-7 (b). In each magnetic surface, the field line follows a helical path as it goes round the torus on its associated magnetic surface. Starting from a certain poloidal angle θ_0, the field also has a certain position in toroidal plane φ_0, the field line goes through torus over a ring ($2\pi R$) and then will return to the toroidal position φ_0 after change of poloidal angle $\Delta\theta$ as shown in Fig. 1-7 (b). The ratio between the angles through the toroidal and poloidal direction is defined as the safety factor of field line,

$$q = \frac{2\pi}{\Delta\theta}. \tag{1-2}$$

And

$$\tan(\Delta\theta) = \frac{B_\theta}{B_\varphi} = \frac{\Delta\theta \times r}{2\pi \times R}. \quad (1\text{-}3)$$

Thus, the safety factor can be rewritten as

$$q = \frac{r}{R}\frac{B_\varphi}{B_\theta}. \quad (1\text{-}4)$$

If a magnetic field line returns to its starting position after exactly one rotation round the torus, then $q = 1$. Since magnetic fields are generally not parallel on adjacent magnetic surfaces, the safety factor changes with magnetic surface (minor radius) as shown in Fig. 1-7 (c). It also appears as a crucial parameter in transport theory and relates to the ITB formation. In normal magnetic configuration, the minimum q locates at or close to the magnetic axis and increases outwards. For estimating this kind of change, another parameter, magnetic shear, is introduced

$$s(r) = \frac{r}{q(r)}\frac{\partial q(r)}{\partial r}. \quad (1\text{-}5)$$

A large shear (absolute) means safety factor changes with minor radius rapidly, in contrast, small shear (absolute) means the change is gradual. Positive shear means the safety factor increases with minor radius and negative shear means decreases with minor radius.

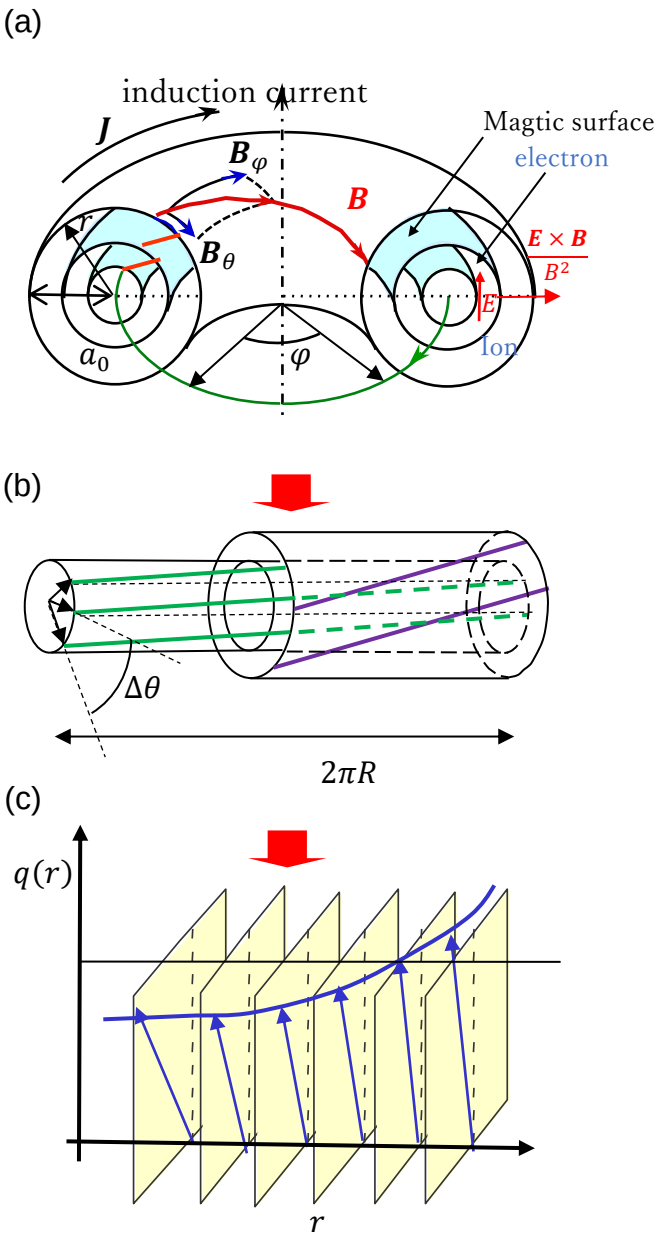

Fig. 1-7 The magnetic configuration in tokamak (a), the magnetic surface after torus being stretched (b), and safety factor over minor radius (c) [courtesy of Y.kishimoto].

1.3 Modelling and simulating magnetically confined fusion plasmas

In magnetized plasma, the electric field $\boldsymbol{E}$ and magnetic field $\boldsymbol{B}$ field are not prescribed exactly but depends on the positions and motions of the charges themselves. In other words, it is a self-consistent problem that the particles will generate or modify the fields as they move along their orbits and the fields ($\boldsymbol{E}$, $\boldsymbol{B}$) will cause the particles to move in those exact orbits. And this must be done in a time-varying situation.

1.3.1 Fluid description of plasma

It is hopeless to predict the plasma's behavior by solving each particles' equation of motion. Fortunately, this is not usually necessary. In fact, fluid model is compatible for plasma if the density is large enough and/or collisions are frequent enough. Specifically, the mean free path of particles must be far less than the characteristic length of the fluid element. Moreover, the thermodynamic equilibrium will be quickly restored by the collision or Coulomb interaction between particles when the external perturbation deviates from the thermodynamic equilibrium, due to the other characteristic times in the fluid element change is much greater than the mean free time of the particles. In magnetically confined plasma, the long-range Coulomb interaction between charged particles makes the energy and momentum exchange between particles frequently, and due the role of Lorenz force, the charged particles in the direction of the cross-magnetic field are limited in the range of the cyclotron radius. Therefore, as long as the magnetic fluid element of the cross-magnetic field direction of the characteristic length is much greater than the cyclotron radius can be applied to the fluid description. It can be seen that the magnetically confined plasma is more suitable for fluid approximation than neutral gas.

The Magnetohydrodynamics (MHD)

A reduced fluid model for plasma is the Magnetohydrodynamics (MHD) which considers plasma is not viscous but adiabatic. The Navier-Stokes equations is used for representing its fluid nature, meanwhile, Maxwell's equations take into account of its electromagnetic properties. In this reduced model, we must solve a large number of unknowns. For instance, in the case of the single fluid model, mass density ρ, the fluid velocity $\boldsymbol{u}$, the current $\boldsymbol{J}$, the pressure P, the electric field $\boldsymbol{E}$ and the magnetic field $\boldsymbol{B}$. All. They are governed by a set of equations as follow

the continuity equation	$\frac{\partial \rho}{\partial t} + \nabla \cdot (\rho \boldsymbol{u}) = 0$	(1-6)
the momentum equation	$\rho \frac{d\boldsymbol{u}}{dt} = -\nabla P + \boldsymbol{J} \times \boldsymbol{B}$	(1-7)
the Maxwell-Faraday equation	$\nabla \times \boldsymbol{E} = -\frac{\partial \boldsymbol{B}}{\partial t}$	(1-8)
the Maxwell-Ampère equation	$\nabla \times \boldsymbol{B} = \mu_0 \boldsymbol{J}$	(1-9)
Ohm's law	$\boldsymbol{J} = \sigma(\boldsymbol{u} \times \boldsymbol{B} + \boldsymbol{E})$	(1-10)

the closure equation $$p\rho^{-\gamma} = \text{cons.} \tag{1-11}$$

with the 2 additional parameters: the conductivity σ and the adiabatic index (heat capacity ratio) γ. Particular values for those two parameters can lead to common approximations such as ideal MHD ($\sigma \to \infty$) otherwise resistive MHD and incompressibility ($\gamma = 0$). Another important parameter of MHD, the parameter beta β, is the ratio of the plasma pressure P over the magnetic pressure $B^2/2\mu_0$, and is an important characteristic for fusion reactor design as beta reflects the efficiency of the confinement for the strength of electromagnets used.

1.3.2 Kinetic description of plasma

The fluid theory is the simplest description of a plasma and sufficiently accurate to describe the majority of observed phenomena. However, the limitation of MHD arising from the assumption is strongly collisional (discussed above). In the actual operation of tokamak, with the increase of temperature, the characteristic time of fluid element change is getting shorter and shorter. On the other hand, the mean free path of particles is proportional to the square of temperature T^2 due to the long-range Coulomb interaction between charged particles. Therefore, , the collision frequency falls as well as the resistivity which varies with temperature as $T^{-3/2}$. That means the mean free time of the particles become longer. The result is that whether from the spatial scale or the time scale, high-temperature plasma is no longer suitable for MHD approximation approximate treatment. In addition, plasma may deviate from the thermodynamic equilibrium for relatively long time. For these, we need to consider the distribution function in velocity space $f_s(\boldsymbol{r}, \boldsymbol{v}, t)$ where s means the species of charged particles; this treatment is called kinetic theory. It is governed by the Boltzmann equation,

$$\frac{\partial f_s}{\partial t} + \boldsymbol{v} \cdot \frac{\partial f_s}{\partial \boldsymbol{r}} + \frac{e_s}{m_s}(\boldsymbol{E} + \boldsymbol{v} \times \boldsymbol{B}) \cdot \frac{\partial f_s}{\partial \boldsymbol{v}} = \left(\frac{\partial f_s}{\partial t}\right)_c. \tag{1-12}$$

In a sufficiently hot plasma, collisions can be neglected., the Boltzmann equation Eq. (1-12) is reduced to so called Vlasov equation,

$$\frac{\partial f_s}{\partial t} + \boldsymbol{v} \cdot \frac{\partial f_s}{\partial \boldsymbol{r}} + \frac{e_s}{m_s}(\boldsymbol{E} + \boldsymbol{v} \times \boldsymbol{B}) \cdot \frac{\partial f_s}{\partial \boldsymbol{v}} = 0. \tag{1-13}$$

Formally, instead of the mass distribution, temperature, pressure, velocity of fluid element and electric current found in MHD, kinetic theory describes the plasma's state through distribution function over a 6-dimensional phase space (3 spatial dimensions

and 3 velocity dimensions). In the magnetically confined plasma, the trajectory of charged particles is a helix that winds around the field line. Based on the so-called gyro-ordering, this trajectory can be decomposed into a relatively slow motion of the guiding center along the field line and a fast circular motion, called gyromotion. Since the gyromotion is irrelevant for most plasma behavior, averaging over this gyromotion is feasible, which reduces the equation (1-13) to five dimensions (3 spatial dimensions and 2 velocity dimensions). This theoretical framework is so-called gyro-kinetic and introduced in chapter 2.

1.4 Plasma heating in tokamak

In order to achieve fusion conditions, we must first heat the electrically neutral 'fuel' until it is ionized. That means the required plasma temperature is in the range of 10–30 keV. Initially, the fuel is neutral gases with a high resistance, so that the ohmic heating through an inducted electric field is a good choice in the first stage. Then the plasmas initially are produced by ohmic heating ($P_\Omega \sim \eta_R j$, where j is the current density and η_R is the resistivity). At low temperatures ohmic heating is quite efficient and, in large tokamaks, easily produces temperatures of a few KeV. However, as the temperature increases, the collision frequency falls as well as the resistivity which varies with temperature as $T_e^{-3/2}$. It becomes less effective at high temperatures. Thus, to reach the temperature required for ignition it is necessary to provide some forms of heating.

There are several proposed methods of achieving this. The two main ways which are envisaged for heating to ignition temperatures are the energetic Neutral Beams Injection (NBI) and the resonant absorption of Radio Frequency (RF) electromagnetic waves. With the level of confinement found experimentally, all of these methods would in principle be able to provide heating of the required magnitude.

1.4.1 Neutral Beams Injection (NBI)

Since the high temperature plasma is confined by a strong magnetic field, injection of energetic ions from outside to heat the plasma would be reflected due to the Lorenz force. The most efficient way to heat the plasma by energetic particles is to inject high energy 'neutrals'. NBI with a beam energy much above the average kinetic energy of the plasma electrons or ions is used (beam energy typically ~40 keV – 1 MeV). This heating scheme is as simple as warming up cold water by pouring in hot

water. In the plasma the neutral particles become charged again and as a result are confined by the magnetic field. They are then slowed by collisions with the plasma particles. The energy transfer from ionized beam fast ions to thermal ions and electrons is basically through classical Coulomb collision processes. The basic processes of Coulomb collision between beam ions and a thermal plasma are slowing down and diffusion in the velocity space.

Since the mass of ion is much larger than that of electron $m_i/m_e \gg 1$, the scattering of the beam ions caused by the collisions with the plasma electrons is exceedingly small. In other words, the direction of beam ion velocity will be same after the collisions with plasma electron. Consequently, the heating of the electron is given by,

$$P_e = -F_{b-e} v_b. \tag{1-14}$$

The force F_{b-e} transmit to the beam ion is given by the rate of momentum loss,

$$F_{b-e} = -\frac{m_b v_b}{\tau_{se}}. \tag{1-15}$$

Where m_b is the mass of the beam ions and τ_{se} is the corresponding slowing down time. Considering the plasma electron thermal velocity is much larger than velocity of beam ions namely $v_b \ll v_{e_T}$, the slowing down time is,

$$\tau_{se} = \frac{3(2\pi)^{1/2} T_e^{3/2}}{m_e^{1/2} m_b A_D}, \tag{1-16}$$

with $A_D = \frac{ne^4 \ln\Lambda}{2\pi\varepsilon_0^2 m_b^2}$. where ε_0 is vacuum permittivity and $\ln\Lambda \sim (10 \sim 20)$ in normal fusion plasma. So that, the electron heating power is,

$$P_e = \frac{2m_e^{1/2} m_b A_D \mathcal{E}_b}{3(2\pi)^{1/2} T_e^{3/2}}, \tag{1-17}$$

Where $\mathcal{E}_b = \frac{1}{2} m_b v_b^2$ is the beam energy.

As regard the heating power on plasma ions, because the mass of plasma ions m_i is comparable with that of beam ions, the slowing down of the beam ions is accompanied by a scattering of the beam ion velocities principally perpendicular to the initial direction of beam. this spreading of perpendicular velocities also constitutes a 'heating' of beam ions.

$$P_i = -F_{b-i}v_b - \frac{1}{2}m_b\bar{v}_\perp^2 \tag{1-18}$$

Similar to the F_{b-e},

$$F_{b-i} = -\frac{m_b v_b}{\tau_{si}} \tag{1-19}$$

While $\tau_{si} = \frac{2v_b^3}{A_D}\frac{m_i}{m_b+m_i}$ due to the plasma ion thermal velocity is much smaller than velocity of beam ions namely $v_b \gg v_{e_T}$. Thus,

$$-F_{b-i}v_b = \frac{m_b A_D}{2v_b}\frac{m_b+m_i}{m_i} \tag{1-20}$$

Combining with

$$\frac{1}{2}m_b\bar{v}_\perp^2 = \frac{m_b A_D}{2v_b} \tag{1-21}$$

The direct heating power of plasma ions is given by

$$P_i = \frac{m_b^{5/2}A_D}{2^{3/2}m_i\mathcal{E}_b^{1/2}} \tag{1-22}$$

It is right only the fraction $m_b/(m_i+m_b)$ of $F_{b-i}v_b$.

Then the total direct heating per beam ion P_T is

$$P_T = m_b A_D\left(\frac{2m_e^{1/2}\mathcal{E}_b}{3(2\pi)^{1/2}T_e^{3/2}} + \frac{m_e^{3/2}}{2^{3/2}m_i\mathcal{E}_b^{1/2}}\right) = \frac{2m_e^{\frac{1}{2}}m_b A_D}{3(2\pi)^{\frac{1}{2}}T_e^{\frac{3}{2}}}\mathcal{E}_b\left(1+\left(\frac{\mathcal{E}_c}{\mathcal{E}_b}\right)^{\frac{3}{2}}\right) \tag{1-23}$$

$$\mathcal{E}_c = \left(\frac{3\sqrt{\pi}}{4}\right)^{2/3}\left(\frac{m_i}{m_e}\right)^{1/3}\frac{m_b}{m_i}T_e \tag{1-24}$$

The first term in right side of Eq. (1-23) is plasma electron heating which is proportional to the beam energy $\mathcal{E}_b$ and the second term in right side of Eq. (1-23) is plasma ions heating which will take over as the beam ions lose energy. The beam speed v_b is usually much larger than the ion thermal speed v_{i_T} due to the heating objective and much less than the electron thermal speed , v_{e_T} due to the large mass ratio, $v_{i_T} \ll v_b \ll v_{e_T}$. If the beam energy $\mathcal{E}_b$ is higher than $\mathcal{E}_c$, the energy transfer to ions is smaller than that to electrons, while the energy transfer to ions becomes dominant when $\mathcal{E}_b$ becomes less than $\mathcal{E}_c$. This is the reason why $\mathcal{E}_c$ is called the “critical energy”. The instantaneous ion heating fraction is given by,

$$F_i\left(\frac{\varepsilon_b}{\varepsilon_c}\right) = \frac{1}{1+\left(\frac{\varepsilon_b}{\varepsilon_c}\right)^{3/2}} \tag{1-25}$$

On the other hand, the neutral beam is directional and is injected into the plasma with not only energy, but also momentum. This causes heated particles (both plasma ions and electrons) in the plasma to momentarily offset the thermodynamic equilibrium. The charged particle distribution function is not symmetrical in the velocity space until the injected momentum is absorbed by fusion machines. Because the magnetic confinement system is a torus and the tokamak has a toroidal plasma current maintaining the poloidal magnetic field $\boldsymbol{B}_\theta$, there are three injection geometries, namely co-tangential, counter-tangential and perpendicular injection, as shown schematically in Fig. 1-8. 'Co-' means that beam is injected parallel to the toroidal plasma current, while 'counter' means that beam is injected anti-parallel to the plasma current. 'Perpendicular' means that beam is injected (nearly) perpendicular to the magnetic field. The asymmetry of the distribution function occurs in which direction, depending on the injection angle of the NBI. perpendicular injection means the equilibrium distribution function $F(v_\parallel, v_\perp)$ is asymmetrical in perpendicular velocity $v_\perp$ space.

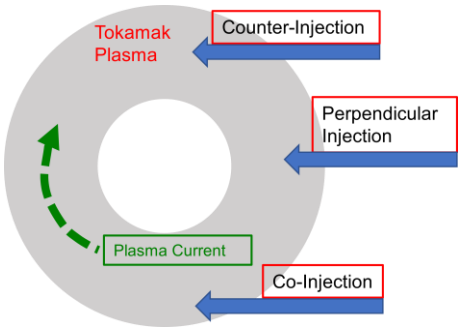

Fig. 1-8 Three injection geometries of NBI

NBI has proven to be one of the most promising and best understood methods to heat a dense plasma and to drive plasma current in fusion machines. A fundamental feature of heating by a neutral beam was clarified by Stix [6]. The concept of using energetic neutral beams for heating the plasma was proposed in the 1950s [7]and the first beam injection experiments were performed in mirror machines using PHOENIX [8], OGRA [9] and ALICE [9] in the 1960s.

1.4.2 Electron/Ion Cyclotron Resonance Heating (ECRH/ICRH)

Radio frequency heating transfers energy from an external source to the plasma by means of electromagnetic waves. When an electromagnetic wave propagates through a plasma the electric field of the wave accelerates the charged particles which then heat the plasma through collisions The collisional absorption scales as $T_e^{-3/2}$ so that, just as for ohmic heating, collisional absorption of electromagnetic waves is ineffective as a direct heating mechanism for hot plasmas. However, electromagnetic waves in plasma are subject to resonant absorption which is a collisionless process and produces strong heating. A magnetized, multispecies plasma has a number of resonant frequencies which give rise to absorption of energy of an incident field, each resonance is associated not only with absorption but also reflection, that is resonant reflection. Thus, when the wave approaches the resonance from the high magnetic field side strong absorption takes place. When the wave approaches from the low magnetic field side strong reflection may occur.

Current drive may be due to direct momentum input by the RF waves, or asymmetric deformation of the electron distribution function either by quasi-linear diffusion of resonant particles, or asymmetric heating, or scattering of trapped particles into circulating ones. Absorption of RF waves in different regions of the plasma cross-section may be affected by special resonant layers (e.g., cyclotron resonance) or by local conditions which depend on the Landau resonance of particles with the waves with matching parallel phase velocity $\omega/k_{\|}$ (determined by the index of refraction ,$N_{\|} = k_{\|}/\omega = 1/v_{ph,\|}$).

The two main methods which are envisaged for heating to ignition temperatures are the injection of energetic neutral beams and the resonant absorption of radio frequency (RF) electromagnetic waves. With the level of confinement found experimentally, all of these methods would in principle be capable of providing heating of the required magnitude, and both have been successfully tested at power levels or tens of MW.

$$\nabla \times \boldsymbol{E}_1 = -\frac{\partial \boldsymbol{B}_1}{\partial t} \tag{1-26}$$

$$\nabla \times \boldsymbol{B}_1 = \mu_0 \varepsilon_0 \frac{\partial \boldsymbol{E}_1}{\partial t} + \mu_0 \boldsymbol{j}_1 = \mu_0 \varepsilon_0 \overleftrightarrow{\boldsymbol{\varepsilon}} \cdot \frac{\partial \boldsymbol{E}_1}{\partial t} \tag{1-27}$$

Taking the curl of Eq. (1-26) and using Eq. (1-27), then obtains

$$\nabla \times (\nabla \times \boldsymbol{E}_1) = -\mu_0 \varepsilon_0 \overleftrightarrow{\boldsymbol{\varepsilon}} \cdot \frac{\partial^2 \boldsymbol{E}_1}{\partial t^2}, \tag{1-28}$$

assuming field perturbations of the Plane-wave solutions form $\exp[i(\boldsymbol{k} \cdot \boldsymbol{x} - \omega t)]$ and define index of refraction $\boldsymbol{N} = c\boldsymbol{k}/\omega$. The dielectric tensor defined as

$$\overleftrightarrow{\boldsymbol{\varepsilon}} = \overleftrightarrow{\boldsymbol{I}} + \frac{i}{\varepsilon_0 \omega} \overleftrightarrow{\boldsymbol{\sigma}}. \tag{1-29}$$

Eq. (1-28) can be rewritten as in a Cartesian coordinate system with $\boldsymbol{B}_0$ being in z direction.

$$\boldsymbol{N} \times (\boldsymbol{N} \times \boldsymbol{E}_1) + \overleftrightarrow{\boldsymbol{\varepsilon}} \cdot \boldsymbol{E}_1 = 0. \tag{1-30}$$

Assume the $\boldsymbol{k}$ lies in the $x - z$ plane, namely,

$$\boldsymbol{k} = \boldsymbol{k}_x + \boldsymbol{k}_z = k\sin\theta \boldsymbol{e}_x + k\sin\theta \boldsymbol{e}_x, \tag{1-31}$$

$$\boldsymbol{N} = \boldsymbol{N}_x + \boldsymbol{N}_z = N\sin\theta \boldsymbol{e}_x + N\sin\theta \boldsymbol{e}_x, \tag{1-32}$$

the dispersion relationship can be written in the following matrix form:

$$\begin{Bmatrix} \varepsilon_{xx} - N^2\cos^2\theta & \varepsilon_{xy} & \varepsilon_{xz} + N^2\cos\theta\sin\theta \\ \varepsilon_{yx} & \varepsilon_{yy} - N^2 & \varepsilon_{yz} \\ \varepsilon_{zx} + N^2\cos\theta\sin\theta & \varepsilon_{zy} - N^2 & \varepsilon_{zz} - N^2\sin^2\theta \end{Bmatrix} \begin{Bmatrix} E_x \\ E_y \\ E_z \end{Bmatrix} = 0. \tag{1-33}$$

For investigating the various types of waves in the plasma, here we further simplify the model to cold plasma. The reduced dispersion relationship is

$$\begin{Bmatrix} S - N^2\cos^2\theta & -iD & N^2\cos\theta\sin\theta \\ iD & \mathrm{S} - N^2 & 0 \\ N^2\cos\theta\sin\theta & 0 & P - N^2\sin^2\theta \end{Bmatrix} \begin{Bmatrix} E_x \\ E_y \\ E_z \end{Bmatrix} = 0, \tag{1-34}$$

which is written in the so-called Stix parameters [10], S, L, R, and D

$$\begin{cases} P = 1 - \sum_s \frac{\omega_{ps}^2}{\omega^2} \\ S = 1 - \sum_s \frac{\omega_{ps}^2}{\omega^2 - \Omega_s^2} \\ D = 1 - \sum_s \frac{\Omega_s}{\omega} \frac{\omega_{ps}^2}{\omega^2 - \Omega_s^2} \end{cases}, \tag{1-35}$$

$$\begin{cases} R = S + D = 1 - \sum_s \frac{\omega_{ps}^2}{\omega^2} \frac{\omega}{\omega + \Omega_s} \\ L = S - D = 1 - \sum_s \frac{\omega_{ps}^2}{\omega^2} \frac{\omega}{\omega - \Omega_s} \end{cases}, \tag{1-36}$$

Then we can obtain the polarization of the electric field perpendicular to the magnetic field ($\theta = \pi/2$, $\cos\theta = 0$) as

$$\frac{E_x}{E_y} = i\,\frac{S-N^2}{D} = \pm i = \exp\left(\pm i\frac{\pi}{2}\right). \tag{1-37}$$

$+1(-1)$ corresponds to Right (Left) Hand circularly Polarized waves (RHCP or LHCP), while a constant not equal to unity gives an elliptically polarized wave. Where $\omega_{p_s} = n_s e_s^2/m_s\varepsilon_0$ is the plasma frequency of particle species s, and $\Omega_s = e_s B/m_s$ is the corresponding cyclotron (gyro) frequency (e_s carrying the sign of the charge).

The dispersion relationship is obtained by setting the determinant of the above matrix equation, Eq. (1-34), to zero for making sure the equation has the non-zero solutions of the various electric field components. Then the dispersion relationships can be expanded as

$$AN^4 - BN^2 + C = 0, \tag{1-38}$$

where,

$$\begin{cases} A = P\cos^2\theta + S\sin^2\theta \\ B = SP(1+\cos^2\theta) + (S^2 - D^2)\sin^2\theta = SP(1+\cos^2\theta) + RL\sin^2\theta. \\ C = P(S^2 - D^2) = PRL \end{cases} \tag{1-39}$$

Further, equations can also be written in Alice form,

$$\mathrm{Tan}^2\,\theta = -\frac{P(N^2-R)(N^2-L)}{(SN^2-RL)(N^2-P)}. \tag{1-40}$$

It is found that particularly simple results are obtained in the limit of parallel propagation, namely for $\theta = 0$, when we can reduce the dispersion relationship, Eq. (1-38), to

$$P(N^2 - R)(N^2 - L) = 0. \tag{1-41}$$

There three solutions those $P = 0$, $N^2 = R$, $N^2 = L$ corresponding to three different patterns of fluctuation.

The pattern for $P = 0$ is the Langmuir wave or plasma oscillation $\omega = \left(\omega_{p_i}^2 + \omega_{p_e}^2\right)^{1/2} = \omega_p$. In following, we consider the plasma including only two particle species which are electron and one kind of ion with electric charge of e.

Then we investigate the wave when $N^2 = R$. The dispersion relationship is,

$$N^2 = 1 - \sum_j \frac{\omega_{pj}^2}{\omega^2}\frac{\omega}{\omega+\Omega_j} = 1 - \frac{\omega_p^2}{(\omega-|\Omega_e|)(\omega+\Omega_i)}. \quad (1\text{-}42)$$

The polarization of the electric field

$$\frac{E_x}{E_y} = i\,\frac{S-N^2}{D} = i\frac{S-R}{D} = -i. \quad (1\text{-}43)$$

Implying that it is right hand circularly polarized wave and consistent with the direction of electron cyclotron. From the dispersion relationship we know that when the wave frequency approaches to electron cyclotron frequency $\omega \to \Omega_e$ from smaller side the index of refraction N and/or wave vector $\boldsymbol{k}$ approaches to infinity. Namely, resonances or absorption take place. In the eyes of electrons, the fluctuating electric field is almost constant and can continuously accelerate the electrons. This can be used to heat the electron which is called Electron Cyclotron Resonance Heating (ECRH) . On the other hand, when $N^2 = L$, The dispersion relationship is

$$N^2 = 1 - \sum_j \frac{\omega_{pj}^2}{\omega^2}\frac{\omega}{\omega-\Omega_j} = 1 - \frac{\omega_p^2}{(\omega+|\Omega_e|)(\omega-\Omega_i)}. \quad (1\text{-}44)$$

The polarization of the electric field

$$\frac{E_x}{E_y} = i\,\frac{S-N^2}{D} = i\frac{S-L}{D} = i. \quad (1\text{-}45)$$

Similarly, we can get a left hand circularly polarized wave which is consistent with the direction of ion cyclotron. The resonances or absorption take place if wave frequency approaches to ion cyclotron frequency $\omega \to \Omega_i$, implying that it can be used to heat the ion which is called Ion Cyclotron Resonance Heating (ICRH).

When the wave propagates in direction perpendicular to the equilibrium magnetic field, $\theta = \pi/2$, the dispersion relationship is reduced to

$$(N^2 - P)(SN^2 - RL) = 0. \quad (1\text{-}46)$$

When $N^2 = P = 1 - \omega_p^2/\omega^2$, the perturbed electric field oscillates only in the direction parallel to equilibrium magnetic field. Namely the equilibrium magnetic field does not affect the wave which is so-called O-mode or ordinary mode of propagation without resonance. But it will be cut-off at frequency $\omega \to \omega_p$. The important branch is

$N^2 = P = RL/S$. The perturbed electric field oscillates only in the direction perpendicular to equilibrium magnetic field. It is so-called X-mode or extraordinary mode of propagation. It is obvious that this wave is resonant when

$$1 - \frac{\omega_{p_e}^2}{\omega^2 - \Omega_e^2} - \frac{\omega_{p_i}^2}{\omega^2 - \Omega_i^2} = 0 \tag{1-47}$$

Considering $\Omega_i \ll \omega$ and $\omega_{p_i} \ll \omega$, we get the so-called upper hybrid range of frequency

$$\omega_{\mathrm{HH}} = \sqrt{\Omega_e^2 + \omega_{p_e}^2}. \tag{1-48}$$

When the frequency of wave is much smaller than electro cyclotron frequency $\omega \ll \Omega_e$, the so-called lower hybrid range of frequency will be obtained as

$$\omega_{\mathrm{LH}} = \sqrt{\Omega_i^2 + \frac{\Omega_e^2 \omega_{p_i}^2}{\Omega_e^2 + \omega_{p_e}^2}}. \tag{1-49}$$

The lower hybrid frequency ω_{LH} is near the ion plasma frequency ω_{p_i}. On the other hand, the wave is cut-off when $R = 0$ or $L = 0$. Accordingly, the cutoff frequencies are derived

$$\begin{cases} \omega_{\mathrm{R}} = \sqrt{\omega_{p_e}^2 + \frac{\Omega_e^2}{4}} + \frac{\Omega_e}{2} \text{ Right hand circularly polarized wave} \\ \omega_{\mathrm{L}} = \sqrt{\omega_{p_e}^2 + \frac{\Omega_e^2}{4}} - \frac{\Omega_e}{2} \text{ Left hand circularly polarized wave} \end{cases}. \tag{1-50}$$

The magnetic confined plasma can be heated by the radio-frequency waves at a few resonant frequencies while the radio-frequency also could be cut-off. Since the cyclotron frequencies of ion and electron Ω_i, Ω_e are the function of equilibrium magnetic field (space) and the frequency of plasma oscillation is dependent on the particle density, the heating accessibility is complicated the details are summarized in his classic book [11].

1.5 About this thesis

1.5.1 Motivation

Transport barriers (TBs) characterized by a steep density and/or temperature gradient play an important role for achieving high-performance plasma in magnetic

fusion plasma since such TBs, which are emerged either in edge region (H-mode) or interior region (Internal Transport barrier) once conditions are satisfied, can suppress anomalous transport and reduce the thermal and/or particle diffusivity. Many experiments indicate that auxiliary heating, like ECRH ICRH NBI are benefit for the formation of ITB. On the other hand, ITB often appears in plasma with a reversed safety factor profile as well as flat one. The ITB and related anomalous transport are continually active subjects of research, whether from the theoretical or numerical point of view. Significant efforts have been done for understanding such TBs incorporated with those for understanding anomalous transport. As the candidate causing anomalous transport, various types of drift modes categorized as micro-instability have been studied. Ion temperature gradient (ITG) mode has been considered to be responsible for anomalous ion transport [12–17] whereas trapped electron mode (TEM) for anomalous electron transport. Both of which are in the range of ion gyro-radius. Furthermore, the ITG modes or TEM along with the respective kinds of turbulence are also altered in the presence of magnetic field fluctuations. The anomalous transport properties may thus be changed significantly due to the Kinetic Ballooning Mode (KBM).

Both current and future fusion devices require the highest feasible beta to operate at maximum efficiency. In the advanced tokamak experiments is highly desirable for a large fraction of noninductive current driven by bootstrap effects [18,19] by increasing beta. Since the bootstrap current is proportional to the pressure gradient [20]. This noninductive current density profile might make the safety factor profile flatten with almost zero magnetic shear even reversed shear in the core region. Such a change of the safety factor profile and magnetic shear influences the transport, sometimes leading to the confinement improvement. In discharge of the Tokamak Fusion Test Reactor (TFTR), the ITB foot appears outside the location of the q_{min} , which suggests that both negative shear and weak positive shear contribute to the reduction of transport [21]. The reversed magnetic shearing has been widely studied and it should be responsible for the formation of the ITB due to the breaking up of the toroidal coupling at $q_{\min}$ surface and produces a discontinuity (or gap) in wave excitation [22]. However, a different type of global eigenmodes is found which is excited across the $q_{\min}$-surface, then, diminish the performance of the transport barrier. Recently, a possible candidate appears in global gyrokinetic simulations with a high beta, which is excited at $q_{\min}$-surface and considered to be kinetic infernal mode (KIM) [23].

Infernal mode is mainly driven at the magnetic surface where magnetic shear vanishes. The coupling of KIM occurs in the low shear region, where the safety factor is close to a rational, namely $q = \frac{m_0}{n} + \delta q$ [24,25]. The destabilization is due to the combined effect of the pressure gradient and the closeness of q to the resonance m_0/n. So that, it could be stabilized by elimination of pressure gradients in the region of weak shear [23]. What is impressive is that the growth rate of infernal mode is shown to be an oscillatory function of the toroidal mode number n, if n is treated as a continuous parameter [26–31]. In Hastie and Taylor's study [26], they attribute the oscillations to a breakdown of the standard ballooning theory as the shear is reduced $n\left(\frac{rdq}{dr}\right)^2 \ll 1$. But it is not applicable for further reduced magnetic shear (zero shear) [27]. The oscillation in growth spectrum of KIM is not understood very well and the beta threshold is not sufficiently investigated.

For example, in recent HL-2A experiment [32], an ion-ITB is formed after NBI but disappears shortly after ECRH is applied in almost flat q-profile region. The present thesis aims at investigating the behavior of the dominant micro-instabilities in presence of the auxiliary heating and/or flat q-profile.

1.5.2 Organization of the chapters

For this purpose, several steps could be necessary, starting with the plasma heating in tokamak which has been introduced in Sec. 1.4. The general outline of the study and its chapters is given below.

In chapter 2, we introduce the gyro-kinetic theory briefly. The main points are the gyro-center coordinate system and the so-called gyro-averaging procedure in such coordinate system utilizing the very separation of time and space scales of charged particle motion. We then present how this approach can be used to derive the fundamental equation system used in a global gyrokinetic code Gyro-kinetic based Numerical Experiment of Tokamaks (GKNET), which consists of the gyrokinetic Vlasov equation and the associated field equations: the quasi-neutrality condition and Ampere's law.

In chapter 3, we study linear micro-instabilities using parameters referring to HL-2A plasma with ion ITB by means of the global toroidal gyrokinetic code GKNET including kinetic electron dynamics. It is found that a type of drift mode, which real

frequency is low and changes the sign from electron diamagnetic direction to that of ion continuously as the poloidal wavenumber increases, dominates plasmas with peaked density profile while with relatively flat ion/electron temperature profiles. The instability is found to be sensitive to the perpendicular ion/electron temperature $T_{i,e_\perp}$. It's excited by the increasing $T_{e_\perp}$ and suppressed by the increasing $T_{i_\perp}$ which is consistent with the observation of ion-ITB collapse after the ECRH which is more powerful than the NBI being kept during the whole process in the HL-2A experiment. Further, like the ion temperature gradient mode, this kind of low frequency instability presents a potential changing into the kinetic ballooning mode with electromagnetic perturbation being taken into account.

In chapter 4, linear micro-instability and non-linear evolution in high−β plasmas with a nearly flat safety factor profile $q(r)\sim q_c$, (constant) and then zero magnetic shear $\hat{s}\sim 0$ are studied using GKNET, where a pressure driven infernal type mode regulated by non-resonant free energy plays a dominant role, while linear dispersion and nonlinear turbulent spectrum exhibit complex corrugated structure for consecutive toroidal mode number n. By defining the resonance mismatch $\Delta\mu \equiv M_\theta - nq_c$ with M_θ the effective poloidal mode number, we present a new law prescribing the smooth dispersion including secondary unstable eigen-modes consisting of plural groups labeled by σ_{ij} with $i = (1,2\cdots\Delta n)$ specifying the primary group while $j = (1,2\cdots)$ the sub-group, each of which contains a discrete set of mode number with an arithmetic progression $n \equiv \{i + \Delta n \cdot \ell\}$. Here, the number of primary groups Δn is determined from $1/\delta q_\mu$ with δq_μ the non-integer residue for q_c. Such discrete dispersion leads to a new class of regrouped turbulent spectrum dominated by directional energy flows among different primary groups toward the lowest mode number $n = \Delta n$ in primary group $\sigma_{i=\Delta n,j=1}$ also the zonal mode $\sigma_{i=\Delta n,j=0}$, which exhibits quasi-coherent homogenized structures leading to larger fluxes.

2 Physical model of GKNET

As we mentioned previously, the magnetic confinement fusion plasma can be described by the kinetic equation like Eqs. (1-12) and/or (1-13). However, the numerical calculation of kinetic equation in the full-orbit costs most of the simulation time to solve the evolution of a six-dimensional distribution function. Fortunately, the dynamics of a charged particle in a strong magnetic field shows up a separation of spatio-temporal scales. The strong magnetic field means that the ion Larmor radius ρ_{i_T} is much smaller than the macroscopic length scale L of the equilibrium plasma and that the frequency being interested in ω is small compared to the ion cyclotron frequency Ω_i.

$$\begin{cases} \rho_{i_T} = \frac{v_{i_T}}{\Omega_i} \ll L \\ \omega \ll \Omega_i \end{cases} \tag{2-1}$$

which allows us to average all quantities over the Larmor orbits of charged particles. The full-orbit kinetic model is simplified due to the distribution function on gyrocenter coordinate is considered to be gyrocenter symmetric. Alternatively, the distribution function in gyro-center coordinate is independent on the gyro-phase. Thus, the dimension of the phase space in Vlasov equation is reduced from six to five through a transform from the particle coordinate to the gyrocenter coordinate. This coordinate transform is determined by the fact that the magnetic moment is an adiabatic quantity in terms of low frequency perturbations as presented in Eq. (2-4). The Lie transform perturbative method is widely applied to obtaining the coordinate transform [33–35]. The principle of the Lie transform is to derive a new Lagrangian 1-form independent of the gyrophase by introducing appropriate generators into the formal formula of the new Lagrangian 1-form, which is the solution of the covariant transform formula of the differential 1-form. These generators in turn determine the coordinate transform.

To derive the gyrokinetic equations, we order the time and length scales in the problem to separate fluctuating and equilibrium quantities. The remainder of this section defines this formal ordering and describes some simple consequences that follow from it. Two length scales are characteristic of gyrokinetics: the small length scale, which is the ion Larmor radius ρ_{i_T} , and the larger length scale L. Their ratio

defines the fundamental expansion parameter ϵ used in the formal ordering:

$$\rho_{i_T}\frac{\nabla B}{B}=\frac{\rho_{i_T}}{L_B}\sim\frac{\rho_{i_T}}{a_0}\sim\epsilon \tag{2-2}$$

Accordingly, two relevant timescales, or frequencies, of interest including the fast timescale is given by the ion cyclotron frequency Ω_i and the intermediate time scale corresponds to the frequency of the turbulent fluctuation. They satisfy the following relationship

$$\frac{\partial/\partial t}{\Omega_i}\sim\epsilon \tag{2-3}$$

In practice, the exact value of those ϵ varies depending on species and between places within the plasma but the ordering is always acceptable. Simple calculations using standard tokamak parameters yields $\epsilon\sim10^{-3}$.

2.1 Hamiltonian of a single charged particle in electromagnetic field

Based on the Hamiltonian mechanics, the movement of a charged particle is described by its Lagrangian

$$\mathcal{L}=\frac{1}{2}m_s|\dot{x}|^2+e_s\boldsymbol{A}\cdot\dot{\boldsymbol{x}}-e\phi, \tag{2-4}$$

Where ϕ is the electrostatic potential and $\boldsymbol{A}$ is the magnetic vector potential. Introducing the canonical conjugate momentum

$$\boldsymbol{p}=\frac{\partial\mathcal{L}}{\partial\dot{\boldsymbol{x}}}=m_s\dot{\boldsymbol{x}}+e_s\boldsymbol{A}, \tag{2-5}$$

The Hamiltonian of the charged particle is written as:

$$\mathcal{H}=\boldsymbol{p}\cdot\dot{\boldsymbol{x}}-\mathcal{L}=\frac{1}{2}m_sv^2+e_s\phi. \tag{2-6}$$

Then the concise equations of motions are expressed as a set of first-order differential equations

$$\begin{cases}\dot{\boldsymbol{x}}=\frac{\partial\mathcal{H}}{\partial\boldsymbol{p}}\\ \dot{\boldsymbol{p}}=\frac{\partial\mathcal{H}}{\partial\boldsymbol{x}}\end{cases}. \tag{2-7}$$

Although, at first glance, the equations are not easy to solve. They come from the more extensive theoretical framework which is a key accessing to advanced theoretical results and deeper properties of physical systems.

One-form representation of Hamiltonian

Here, the system's coordinates are gathered in a single variable with a superscript $\xi = (\xi^t, \xi^{\boldsymbol{x}}, \xi^{\boldsymbol{v}}) = (t, \boldsymbol{x}, \boldsymbol{v})$. For reducing the description of the advanced transformations on this system's coordinates, a one-form,

$$\psi = \boldsymbol{p} \cdot d\boldsymbol{x} - \mathcal{H}dt = [m_s \boldsymbol{v} + e_s \boldsymbol{A}(\boldsymbol{x})] \cdot d\boldsymbol{x} - \left(\frac{1}{2} m_s v^2 + e_s \phi\right) dt, \qquad (2\text{-}8)$$

is applied and each component can alternatively be denoted as

$$\begin{cases} \psi_{\boldsymbol{R}} = m_s \boldsymbol{v} + e_s \boldsymbol{A}(\boldsymbol{x}) \\ \psi_{\boldsymbol{v}} = 0 \\ \psi_t = -\mathcal{H} \end{cases}. \qquad (2\text{-}9)$$

Through this formalism the equations for particle motion are represented by means of the Euler-Lagrange:

$$\left(\frac{\partial \psi_{\boldsymbol{i}}}{\partial \xi^j} - \frac{\partial \psi_{\boldsymbol{j}}}{\partial \xi^i}\right) \frac{\partial \xi^i}{\partial t} = 0, \qquad (2\text{-}10)$$

where Einstein notations is used (implicit summations on ν), as well as the case in following. In one-form notation, the product $\psi_{\boldsymbol{i}} d\xi^i$ should be conserved in all coordinates systems and the one-form Ψ associated with a different set of coordinates $\mathbb{Z}$ verifies. The one-form being transformed, due to the change of coordinates, can be expressed as:

$$\Psi_i = \psi_{\boldsymbol{j}} \frac{d\xi^j}{d\mathbb{Z}^i} \Leftrightarrow \psi_{\boldsymbol{i}} d\xi^i = \Psi_i d\mathbb{Z}^i. \qquad (2\text{-}11)$$

In the next step, we will determine the one-form for the guiding-center coordinates which will neglect the short time scale of the gyromotion. But the small-scale perturbation will then be re-introduced in order to revert to the dynamics of the particle in gyro- center coordinates.

2.2 Gyro-averaged dynamics of the guiding-center

Let us introduce the guiding-center phase space with the following coordinate transformation:

$$\begin{cases} \boldsymbol{x} = \boldsymbol{R} + \boldsymbol{\rho}(\boldsymbol{x}) \\ \boldsymbol{v} = v_{\parallel} \boldsymbol{b}(\boldsymbol{x}) + v_{\perp} \boldsymbol{e}_{\perp} \\ \mu = \frac{m_s v_{\perp}^2}{2B(x)} \end{cases}, \qquad (2\text{-}12)$$

where $\boldsymbol{\rho} = \rho \boldsymbol{e}_\alpha$ and $\boldsymbol{e}_\alpha$ is the unit vector that points from the gyro-center to the particle. The unit vector along the direction of the gyromotion is $\boldsymbol{e}_\perp = \frac{\boldsymbol{v}_\perp}{v_\perp}$. It is important to highlight that ρ (and subsequently the magnetic field B contained in it) is evaluated at the guiding-center $\boldsymbol{R}$ while the vector $\boldsymbol{b}$ which guides $v_\parallel$ is evaluated at $\boldsymbol{x}$.

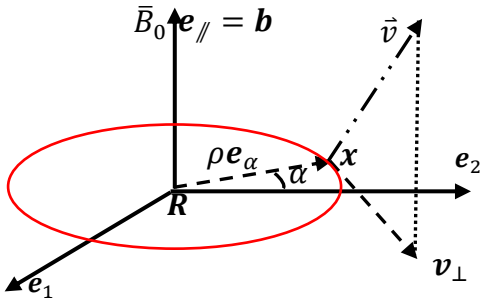

Fig. 2-1 Decomposition of this gyromotion as a parallel translation along the magnetic field line with a speed $v_\parallel$ and a gyration in the perpendicular plane at speed $v_\perp$

It is should be noted that the direct transformation is depends on the magnetic field at the particle's position. However, the particle position cannot be explicitly expressed due to the dependence of the Larmor-radius on $\boldsymbol{x}$. The coordinates are therefore Taylor- expanded around the guiding-center location $\boldsymbol{R}$

$$\rho(\boldsymbol{x}) = \rho(\boldsymbol{R}) + \left(\frac{\partial \rho(\boldsymbol{x})}{\partial \boldsymbol{x}}\right)_{\boldsymbol{x}} \rho(\boldsymbol{x}) \boldsymbol{e}_\alpha(\alpha) + \mathcal{O}((\rho(\boldsymbol{x}) \boldsymbol{e}_\alpha(\alpha))^2). \tag{2-13}$$

So that it is thus sufficient to keep only $\rho(\boldsymbol{x}) \approx \rho(\boldsymbol{R})$

$$\boldsymbol{x} \approx \boldsymbol{R} + \boldsymbol{\rho}(\boldsymbol{R}). \tag{2-14}$$

The particle velocity consists of the velocity along the magnetic field, the gyration velocity and the drift velocities. Recalling the Taylor expansion around $\boldsymbol{R}$

$$\boldsymbol{v}(\boldsymbol{R}, v_\parallel, \mu, \alpha) \approx v_\parallel \left[\boldsymbol{b}(\boldsymbol{R}) + \frac{\partial \boldsymbol{b}(\boldsymbol{R})}{\partial \boldsymbol{R}} \cdot \boldsymbol{e}_\alpha(\alpha) \rho(\boldsymbol{R}, \boldsymbol{\mu})\right] + \rho(\boldsymbol{R}, \boldsymbol{\mu}) \dot{\boldsymbol{e}}_\alpha(\alpha). \tag{2-15}$$

Since there is no transformation on time, we can directly use the expression formula before the transformation.

$$\Psi_t = \psi_{\boldsymbol{t}} = -\frac{1}{2} m_s v_\parallel^2 - \mu B - e_s \phi. \tag{2-16}$$

The $\boldsymbol{R}$ component is expanded into Taylor-series around $\boldsymbol{R}$**,** while keep the term up to first order in ρ

$$\begin{aligned}\Psi_{\boldsymbol{R}} = m_s v_{\parallel}\left[b_i(\boldsymbol{R}) + \frac{\partial \boldsymbol{b_i(R)}}{\partial \boldsymbol{R^j}} e_{\alpha}^{j}(\alpha)\rho(\boldsymbol{R},\mu)\right] + m_s\rho(\boldsymbol{R},\boldsymbol{\mu})\dot{e}_{\alpha_i}(\alpha) \\ + e_s\left[A_i(\boldsymbol{R}) + \frac{\partial \boldsymbol{A_i(R)}}{\partial \boldsymbol{R^j}} \boldsymbol{e_{\alpha}^{j}}(\alpha)\rho(\boldsymbol{R},\boldsymbol{\mu})\right] + e_s A_k(\boldsymbol{R})\frac{d\boldsymbol{\rho(R)}}{\partial \boldsymbol{R^i}} e_{\alpha}^{k}(\alpha)\end{aligned}. \quad (2\text{-}17)$$

The gyro-averaging on $\Psi_{\boldsymbol{R}}$ or any other component Ψ_i is represented by a simple integration over the gyro-angle α,

$$\langle \quad \rangle = \frac{1}{2\pi}\int_0^{2\pi} d\alpha. \quad (2\text{-}18)$$

The gyro-averaged $\boldsymbol{R}$ component is

$$\langle \Psi_{\boldsymbol{R}} \rangle = m_s v_{\parallel}\boldsymbol{b}(\boldsymbol{R}) + e_s\boldsymbol{A}(\boldsymbol{R}). \quad (2\text{-}19)$$

The other components are dealt with in a similar way. According to Eq. (2-11), the $v_{\parallel}$-component is

$$\Psi_{v_{\parallel}} = \psi_{\boldsymbol{j}}\frac{d\xi^j}{dv_{\parallel}} = \psi_{\boldsymbol{x^j}}\underbrace{\frac{dx^j}{dv_{\parallel}}}_{0} + \underbrace{\psi_{\boldsymbol{v^j}}}_{0}\frac{dv^j}{dv_{\parallel}} = 0, \quad (2\text{-}20)$$

which indicates this component remains zero in the guiding-center approximation.

The μ-component takes the form

$$\Psi_{\mu} = [m_s\boldsymbol{v} + e_s\boldsymbol{A}(\boldsymbol{x})]\cdot\frac{\partial \boldsymbol{\rho}}{\partial \mu}\boldsymbol{e}_{\alpha} = e_s\left[\boldsymbol{A_i}(\boldsymbol{R}) + \frac{\partial \boldsymbol{A_i(R)}}{\partial \boldsymbol{R^j}} e_{\alpha}^{j}(\alpha)\rho(\boldsymbol{R},\boldsymbol{\mu})\right]\frac{\partial \boldsymbol{\rho}(R,\boldsymbol{\mu})}{\partial \mu} e_{\alpha}^{i}. \quad (2\text{-}21)$$

Since $\frac{\partial \boldsymbol{\rho}}{\partial \mu} \sim \frac{\boldsymbol{\rho}}{2\mu}$, the term $\rho\frac{\partial \boldsymbol{\rho}}{\partial \mu}$ containing leads to second order terms which can be dropped. gyro-averaging gives

$$\langle \Psi_{\mu} \rangle = 0. \quad (2\text{-}22)$$

The $\dot{\boldsymbol{e}}_{\alpha}(\alpha) = \frac{\partial \boldsymbol{e}_{\alpha}(\alpha)}{\partial \alpha}\dot{\alpha}$ where $\dot{\alpha}$ is the cyclotron (gyro) frequency $\Omega_s = \frac{eB}{m_s}$. Then gyration velocity will be represented as $\frac{e_s}{|e_s|}v_{\perp} = \rho(\boldsymbol{R})\dot{\alpha}$. The α-component after gyro-average is

$$\langle \Psi_{\alpha} \rangle = \frac{2\mu B}{\Omega_s}. \quad (2\text{-}23)$$

Gathering the previous component presented by Eqs. (2-16), (2-19), (2-20), (2-22) and (2-23), we get the fundamental one-form in guiding-center coordinates

$$\begin{aligned}\langle\Psi\rangle = &[m_s v_\parallel \boldsymbol{b}(\boldsymbol{R}) + e_s \boldsymbol{A}(\boldsymbol{R})] \cdot d\boldsymbol{R} + \frac{2\mu B}{\Omega_s} d\alpha \\ &- \left[\frac{1}{2} m_s v_\parallel^2 + \mu B(\boldsymbol{R}) + e_s \phi(\boldsymbol{R})\right] dt\end{aligned} . \tag{2-24}$$

The equations of particle motion would be derived from Eq. (2-24) combining with the Euler-Lagrange equation Eq. (2-10). The results are the well-known drifts of the guiding center which completely ignores the gyromotion. A one-form which we want should take into account of it in the form of perturbation.

2.2.1 Gyro-center coordinates

In this section the fluctuations at the scale of the gyro-radius are added to the guiding-center Lagrangian, without the gyro-phase dependence of the perturbations up to first order in ε.

Perturbed guiding-center one-form

In order to distinguish the fluctuations from the ones calculated above as Eq. (2-24), let us introduce small scale perturbations of the electromagnetic fields in the form

$$\begin{cases} \boldsymbol{A} = \boldsymbol{A}_0 + \boldsymbol{A}_1 \\ \phi = \phi_0 + \phi_1 \end{cases}. \tag{2-25}$$

Following the gyro-kinetic ordering, the perturbations are first order: $\frac{A_1}{A_0} \sim \frac{\phi_1}{\phi_0} \sim \varepsilon$. Then, the initial one-form in particle coordinates in Eq. (2-8) is split into $\psi = \psi_0 + \psi_1$.

$$\begin{cases} \psi_0 = [m_s \boldsymbol{v} + e_s \boldsymbol{A_0}(\boldsymbol{x})] \cdot d\boldsymbol{x} - \left(\frac{1}{2} m_s v^2 + e_s \phi_0(\boldsymbol{x})\right) dt \\ \psi_1 = e_s \boldsymbol{A_1}(\boldsymbol{x}) \cdot d\boldsymbol{x} - e_s \phi_1(\boldsymbol{x}) dt \end{cases}. \tag{2-26}$$

Note that there is no equilibrium electric field in a stationary plasma. The total Lagrangian will be transformed first to the guiding-center and then to gyro-center phase space. The transformation of the equilibrium part ψ_0 is exactly as same as previously we got in Eq. (2-24). The transformation of the perturbed part goes through the same procedure. but because fluctuating quantities vary on a small length scale, Taylor expansion around the guiding-center is not applicable. The fluctuating quantities should be estimated at particle position, so that they are function of the gyro-angle α in guiding-center coordinates. This issue leads to requirement for the Lie transform [36] perturbation theory and tedious derivation can be found in the original work [37–39] . Here we quote their results directly.

The perturbed part of the one-form in the guiding-center phase space can be written as

$$\Psi_1 = e_s \boldsymbol{A_1}(\boldsymbol{x}) \cdot d\boldsymbol{R} + \frac{e_s}{|e_s|}\frac{\boldsymbol{A_1}(\boldsymbol{x})\cdot \boldsymbol{e_\alpha}}{\boldsymbol{v_\perp}} d\mu + \frac{e_s}{|e_s|}\frac{2\mu}{\boldsymbol{v_\perp}} \boldsymbol{A_1}(\boldsymbol{x}) \cdot \frac{d\boldsymbol{e_\alpha}}{d\alpha} d\mu - e_s \phi_1(\boldsymbol{x}) dt. \qquad (2\text{-}27)$$

The sum of Eqs. (2-24) and (2-27) is the complete guiding-center Lagrangian including perturbed part.

Gyro-center transformation

Since the perturbations are first order in ε, the complete one-form might be transformed into the gyro-center phase space for removeing the gyro-angle dependence from the fluctuations from the Lagrangian. Due to the transformation is an inverse pull-back operator, in other words, the new Lagrangian in the gyro-center phase space is expressed in guiding-center coordinates. The gyro-center Lagrangian is distinguished from its guiding-center counterpart with an overbar $\bar{\Psi}$. As a result, the total gyro-center Lagrangian becomes is

$$\begin{cases} \bar{\Psi}_0 = [m_s v_\parallel \boldsymbol{b}_0(\boldsymbol{R}) + e_s \boldsymbol{A}_0(\boldsymbol{R})] \cdot d\boldsymbol{R} + \frac{2\mu B}{\Omega_s} d\alpha \\ \qquad\quad - \left[\frac{1}{2} m_s v_\parallel^2 + \mu B_0(\boldsymbol{R}) + e_s \phi_1(\boldsymbol{R})\right] dt \\ \bar{\Psi}_1 = e_s \langle \boldsymbol{A_1}(\boldsymbol{x})\rangle \cdot d\boldsymbol{R} \\ \qquad\quad -[e_s \langle \phi_1(\boldsymbol{x})\rangle - e_s \langle \boldsymbol{A_1}(\boldsymbol{x}) \cdot \boldsymbol{v}_\perp(\boldsymbol{R}, \mu, \alpha)\rangle] dt \end{cases} . \qquad (2\text{-}28)$$

The oscillating quantities have been removed from the gyro-center Lagrangian and added to the gauge function. The components of the gyro-center Lagrangian becomes independent of the gyro-phase.

2.3 The gyrokinetic Vlasov equation in GKNET

An important property of Hamiltonian systems is the conservation of phase space measure. Another way stating this property is Liouville's theorem, which states the conservation the distribution function f_s (any function of it) along nonlinear characteristics. It well known that the time evolution of the distribution function in the phase space is described by the Vlasov equation which does not take into account of collisions in particle phase space.

$$\frac{\partial f_s}{\partial t} + \dot{\boldsymbol{R}} \frac{\partial f_s}{\partial \boldsymbol{R}} + \dot{v}_\parallel \frac{\partial f_s}{\partial v_\parallel} = 0 \qquad (2.29)$$

$$\frac{\partial f_s}{\partial t} + \dot{\boldsymbol{R}} \frac{\partial f_s}{\partial \boldsymbol{R}} + \dot{v}_\parallel \frac{\partial f_s}{\partial v_\parallel} = 0, \qquad (2\text{-}29)$$

where the gyro-angel is an ignorable coordinate, and the total time derivative of the gyro-center magnetic moment is zero $\dot{\mu} = -\frac{\Omega_s}{B}\frac{\partial \mathcal{H}}{\partial \alpha} = 0$.

Solving the Euler-Lagrange equation Eq. (2-10) applied to the guiding-center phase-space Lagrangian Eq. (2-28), the guiding-center Poisson bracket is constructed is expressed in terms of two arbitrary functions F and G of $(\boldsymbol{R}, v_\parallel, \mu, \alpha)$ as [39]

$$\{F, G\} \equiv \frac{e_s}{m_s}\left(\frac{\partial F}{\partial \alpha}\frac{\partial G}{\partial \mu} - \frac{\partial F}{\partial \mu}\frac{\partial G}{\partial \alpha}\right) + \frac{\boldsymbol{B}^*}{m_s B_\parallel^*}\left(\nabla F \frac{\partial G}{\partial v_\parallel} - \frac{\partial F}{\partial v_\parallel}\nabla G\right) - \frac{1}{e_s B_\parallel^*}\boldsymbol{b}\cdot\nabla F \times \nabla G, \tag{2-30}$$

where the generalized magnetic field is

$$\boldsymbol{B}^* = \boldsymbol{B_{eq}} + \frac{v_\parallel \nabla\times \boldsymbol{b}}{\Omega_s}\boldsymbol{B_{eq}} + \boldsymbol{B_1}, \tag{2-31}$$

$$\boldsymbol{B_1} = \nabla \times \boldsymbol{A_1}, \tag{2-32}$$

$$\boldsymbol{B}_\parallel^* = \boldsymbol{b}\cdot\boldsymbol{B}^*. \tag{2-33}$$

The Vlasov equation will be rewritten in form of Poisson bracket as

$$\frac{\partial f_s}{\partial t} + \{\boldsymbol{R}, \mathcal{H}\}\frac{\partial f_s}{\partial \boldsymbol{R}} + \{v_\parallel, \mathcal{H}\}\frac{\partial f_s}{\partial v_\parallel} = 0. \tag{2-34}$$

2.3.1 Electrostatic model

The Poisson-bracket structure is independent of the electromagnetic field while the Hamiltonian depends explicitly on the electromagnetic potentials $(\phi, \boldsymbol{A})$. However, in the noncanonical formalism, the Hamiltonian only retains its dependence on the electrostatic potential and derivatives of the magnetic potential $\boldsymbol{A} = \boldsymbol{A_0} + \boldsymbol{A_1}$ appear in the Poisson-bracket structure. The calculations of general electromagnetic perturbation are so complicated that, here, we will just show the derivation only considering a simple electrostatic perturbation $(\boldsymbol{A_1} = 0, \boldsymbol{A} = \boldsymbol{A_0})$ which is also able to briefly demonstrate the procedure.

$$\dot{\boldsymbol{R}} = \{\boldsymbol{R}, \mathcal{H}\} = \frac{\boldsymbol{B}^*}{m_s B_\parallel^*}\nabla R \frac{\partial \mathcal{H}}{\partial v_\parallel} - \frac{1}{e_s B_\parallel^*}\boldsymbol{b}\cdot\nabla R \times \nabla \mathcal{H} \tag{2-35}$$

$$\dot{\boldsymbol{v}}_\parallel = \{v_\parallel, \mathcal{H}\} = -\frac{\boldsymbol{B}^*}{m_s B_\parallel^*}\cdot\nabla\mathcal{H} \tag{2-36}$$

In a toroidal system of tokamak as shown in Fig. the coordinates $\boldsymbol{R} = (R_1, R_2, R_3)$ becomes. The (r, θ, φ) is the toroidal coordinates.

$$\begin{cases} R_1 = R = R_0 + r\cos\theta \\ R_2 = r\sin\theta \\ R_3 = R\varphi = (R_0 + r\cos\theta)\varphi \end{cases} \tag{2-37}$$

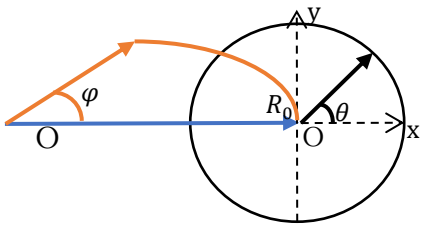

Fig. 2-2 The toroidal coordinate system in tokamak.

The Vlasov equation in form of toroidal coordinates is

$$\begin{aligned} &\frac{\partial f_s}{\partial t} + \frac{dr}{dt}\frac{\partial f_s}{\partial r} + \frac{d\theta}{dt}\frac{\partial f_s}{\partial \theta} + \frac{d\varphi}{dt}\frac{\partial f_s}{\partial \varphi} + \frac{dv_\parallel}{dt}\frac{\partial f_s}{\partial v_\parallel} = \\ &\frac{\partial f_s}{\partial t} + \{r, \mathcal{H}\}\frac{\partial f_s}{\partial r} + \{\theta, \mathcal{H}\}\frac{\partial f_s}{\partial \theta} + \{\varphi, \mathcal{H}\}\frac{\partial f_s}{\partial \varphi} + \{v_\parallel, \mathcal{H}\}\frac{\partial f_s}{\partial v_\parallel} = 0 \end{aligned}. \tag{2-38}$$

The rotation and gradient operators in toroidal coordinates are represented as

$$\begin{cases} \nabla = \boldsymbol{e_r}\frac{\partial}{\partial r} + \boldsymbol{e_\theta}\frac{\partial}{r\partial\theta} + \boldsymbol{e_\varphi}\frac{\partial}{R\partial\varphi} \\ \nabla \times \boldsymbol{A} = \frac{\boldsymbol{e_r}}{rR}\left[\frac{\partial(RA_\varphi)}{\partial\theta} - \frac{\partial(rA_\theta)}{\partial\varphi}\right] + \frac{\boldsymbol{e_\theta}}{R}\left[\frac{\partial A_r}{\partial\varphi} - \frac{\partial(RA_\varphi)}{\partial r}\right] + \frac{\boldsymbol{e_\varphi}}{r}\left[\frac{\partial(rA_\theta)}{\partial r} - \frac{\partial A_r}{\partial\theta}\right] \end{cases}. \tag{2-39}$$

Then the equilibrium magnetic field is

$$\begin{cases} \boldsymbol{B_{eq}} = \frac{R_0}{R}B_0\left(0, \frac{r}{qR_0}, 1\right) \\ B_{eq} = \frac{R_0}{R}B_0 \\ \boldsymbol{b} = \frac{\boldsymbol{B_{eq}}}{B_{eq}} = \left(0, \frac{r}{qR_0}, 1\right) \end{cases}. \tag{2-40}$$

The gradient of equilibrium magnetic field

$$\boldsymbol{\nabla} B = \begin{pmatrix} \frac{\partial B_{eq}}{\partial r} \\ \frac{1}{r}\frac{\partial B_{eq}}{\partial\theta} \\ \frac{1}{R_0 + r\cos\theta}\frac{\partial B_{eq}}{\partial\varphi} \end{pmatrix} = -\frac{B_{eq}}{R}\begin{pmatrix} \cos\theta \\ -\sin\theta \\ 0 \end{pmatrix}, \tag{2-41}$$

and curl of unit vector $\boldsymbol{b}$ is

$$\boldsymbol{\nabla}\times\boldsymbol{b}=\begin{pmatrix}-\frac{\sin\theta}{R}\\-\frac{\cos\theta}{R}\\\frac{2-\hat{s}}{qR_0}\end{pmatrix}, \tag{2-42}$$

where $\hat{s}$ is the magnetic shear

$$\hat{s}=\frac{r}{q}\frac{dq}{dr}. \tag{2-43}$$

The corresponding generalized magnetic field in Eqs. (2-31) and (2-33) are rewritten as

$$\begin{cases}\boldsymbol{B}^*=\boldsymbol{B}_{eq}+\frac{v_\parallel\nabla\times\boldsymbol{b}}{\Omega_s}B_{eq}=B_{eq}\left(-\frac{v_\parallel}{\Omega_s}\frac{\sin\theta}{R},\frac{r}{qR_0}-\frac{v_\parallel}{\Omega_s}\frac{\cos\theta}{R},1+\frac{v_\parallel}{\Omega_s}\frac{2-\hat{s}}{qR_0}\right)\\ B_\parallel^*=B_{eq}\left[\left(\frac{r}{qR_0}\right)^2-\frac{r}{qR_0}\frac{v_\parallel}{\Omega_s}\frac{\cos\theta}{R}+\frac{v_\parallel}{\Omega_s}\frac{2-\hat{s}}{qR_0}+1\right]\approx B_{eq}+B_{eq}\frac{v_\parallel}{\Omega_s}\frac{R_0-(1-\hat{s})R}{qRR_0}\end{cases}. \tag{2-44}$$

Thus, the total time derivative of toroidal coordinates is calculated as follow:

$$\begin{aligned}\dot{r}=\{r,\mathcal{H}\}=&\frac{B_{eq}}{m_sB_\parallel^*}\begin{pmatrix}-\frac{v_\parallel}{\Omega_s}\frac{\sin\theta}{R}\\\frac{r}{qR_0}-\frac{v_\parallel}{\Omega_s}\frac{\cos\theta}{R}\\1+\frac{v_\parallel}{\Omega_s}\frac{2-\hat{s}}{qR_0}\end{pmatrix}\cdot\begin{pmatrix}1\\0\\0\end{pmatrix}m_sv_\parallel\\&+\frac{\mu B_{eq}}{e_sB_\parallel^*R}\begin{vmatrix}0&\frac{r}{qR_0}&1\\1&0&0\\\cos\theta&-\sin\theta&0\end{vmatrix}-\frac{1}{B_\parallel^*}\begin{vmatrix}0&\frac{r}{qR_0}&1\\1&0&0\\\frac{\partial\langle\phi\rangle}{\partial r}&\frac{\partial\langle\phi\rangle}{r\partial\theta}&\frac{\partial\langle\phi\rangle}{R\partial\varphi}\end{vmatrix};\\=&-\frac{1}{B_\parallel^*}\frac{\partial\langle\phi\rangle}{r\partial\theta}+\frac{r}{B_\parallel^*qRR_0}\frac{\partial\langle\phi\rangle}{\partial\varphi}-\frac{B_{eq}}{B_\parallel^*}\frac{v_\parallel^2+\frac{v_\perp^2}{2}}{R\Omega_s}\sin\theta\end{aligned} \tag{2-45}$$

$$\begin{aligned}\dot{\theta}=\{\theta,\mathcal{H}\}=&\frac{B_{eq}}{m_sB_\parallel^*}\begin{pmatrix}-\frac{v_\parallel}{\Omega_s}\frac{\sin\theta}{R}\\\frac{r}{qR_0}-\frac{v_\parallel}{\Omega_s}\frac{\cos\theta}{R}\\1+\frac{v_\parallel}{\Omega_s}\frac{2-\hat{s}}{qR_0}\end{pmatrix}\cdot\begin{pmatrix}0\\\frac{1}{r}\\0\end{pmatrix}m_sv_\parallel\\&+\frac{\mu B_{eq}}{e_sB_\parallel^*R}\begin{vmatrix}0&\frac{r}{qR_0}&1\\0&\frac{1}{r}&0\\\cos\theta&-\sin\theta&0\end{vmatrix}-\frac{1}{B_\parallel^*}\begin{vmatrix}0&\frac{r}{qR_0}&1\\0&\frac{1}{r}&0\\\frac{\partial\langle\phi\rangle}{\partial r}&\frac{\partial\langle\phi\rangle}{r\partial\theta}&\frac{\partial\langle\phi\rangle}{R\partial\varphi}\end{vmatrix};\\=&\frac{1}{B_\parallel^*}\frac{\partial\langle\phi\rangle}{r\partial r}+\frac{B_{eq}v_\parallel}{B_\parallel^*qR_0}-\frac{B_{eq}}{B_\parallel^*}\frac{v_\parallel^2+\frac{v_\perp^2}{2}}{Rr\Omega_s}\cos\theta\end{aligned} \tag{2-46}$$

$$\dot{\varphi} = \{\varphi, \mathcal{H}\} = \frac{B_{eq}}{m_s B_\parallel^*} \begin{pmatrix} -\frac{v_\parallel}{\Omega_s}\frac{\sin\theta}{R} \\ \frac{r}{qR_0} - \frac{v_\parallel}{\Omega_s}\frac{\cos\theta}{R} \\ 1 + \frac{v_\parallel}{\Omega_s}\frac{2-\hat{s}}{qR_0} \end{pmatrix} \cdot \begin{pmatrix} 0 \\ 0 \\ \frac{1}{R} \end{pmatrix} m_s v_\parallel$$

$$+ \frac{\mu B_{eq}}{e_s B_\parallel^* R} \begin{vmatrix} 0 & \frac{r}{qR_0} & 1 \\ 0 & 0 & \frac{1}{R} \\ \cos\theta & -\sin\theta & 0 \end{vmatrix} - \frac{c}{B_\parallel^*} \begin{vmatrix} 0 & \frac{r}{qR_0} & 1 \\ 0 & 0 & \frac{1}{R} \\ \frac{\partial\langle\phi\rangle}{\partial r} & \frac{\partial\langle\phi\rangle}{r\partial\theta} & \frac{\partial\langle\phi\rangle}{R\partial\varphi} \end{vmatrix}; \tag{2-47}$$

$$= \frac{B_{eq} v_\parallel}{B_\parallel^* R}\left(1 + \frac{v_\parallel}{\Omega_s}\frac{2-\hat{s}}{qR_0}\right) - \frac{r}{B_\parallel^* qRR_0}\frac{\partial\langle\phi\rangle}{\partial r} + \frac{\frac{v_\perp^2}{2} B_{eq} r}{\Omega_s B_\parallel^* qRR_0}\frac{\cos\theta}{R}$$

The total time derivative of velocity is

$$\dot{v}_\parallel = \{v_\parallel, \mathcal{H}\} = \frac{B_{eq}}{m_s B_\parallel^*} \begin{pmatrix} -\frac{v_\parallel}{\Omega_s}\frac{\sin\theta}{R} \\ \frac{r}{qR_0} - \frac{v_\parallel}{\Omega_s}\frac{\cos\theta}{R} \\ 1 + \frac{v_\parallel}{\Omega_s}\frac{2-\hat{s}}{qR_0} \end{pmatrix} \cdot \left[-\frac{\mu B_{eq}}{R} \begin{pmatrix} \cos\theta \\ -\sin\theta \\ 0 \end{pmatrix} + q_s \begin{pmatrix} \frac{\partial\langle\phi\rangle}{\partial r} \\ \frac{\partial\langle\phi\rangle}{r\partial\theta} \\ \frac{\partial\langle\phi\rangle}{R\partial\varphi} \end{pmatrix} \right]. \tag{2-48}$$

$$= \frac{v_\parallel}{B_\parallel^*}\frac{\sin\theta}{R}\frac{\partial\langle\phi\rangle}{\partial r} + \frac{1}{B_\parallel^*}\left(\frac{v_\parallel\cos\theta}{R} - \frac{\Omega_s r}{qR_0}\right)\frac{\partial\langle\phi\rangle}{r\partial\theta}$$

$$= -\frac{1}{B_\parallel^*}\left(\Omega_s + v_\parallel\frac{2-\hat{s}}{qR_0}\right)\frac{\partial\langle\phi\rangle}{R\partial\varphi} - \frac{\frac{v_\perp^2}{2} B_{eq} r\sin\theta}{B_\parallel^* qRR_0}$$

In the linear model, drop the higher order terms in ε and retain the zeroth order and first order terms in ε, then the Eqs. (2-45), (2-46) and (2-47) are reduced to

$$\begin{cases} \dot{r} \approx -\frac{B_{eq}}{B_\parallel^*}\frac{v_\parallel^2 + \frac{v_\perp^2}{2}}{R\Omega_s}\sin\theta - \frac{1}{B_\parallel^*}\frac{\partial\langle\phi\rangle}{r\partial\theta} \\ \dot{\theta} \approx -\frac{B_{eq}}{B_\parallel^*}\frac{v_\parallel^2 + \frac{v_\perp^2}{2}}{Rr\Omega_s}\cos\theta + \frac{1}{B_\parallel^*}\frac{\partial\langle\phi\rangle}{\partial r} + \frac{B_{eq} v_\parallel}{B_\parallel^* qR_0}. \\ \dot{\varphi} \approx \frac{B_{eq} v_\parallel}{B_\parallel^* R} \end{cases} \tag{2-49}$$

In order to clarify the physical meaning of each term of velocity. They are gathered and reorganized as

$$\boldsymbol{v} = \dot{r}\boldsymbol{e}_r + \dot{\theta} r \boldsymbol{e}_\theta + \dot{\varphi} R \boldsymbol{e}_\varphi = \underbrace{\left(-\frac{B_{eq}}{B_\parallel^*} \frac{v_\parallel^2 + \frac{v_\perp^2}{2}}{R\Omega_s} \sin\theta \, \boldsymbol{e}_r - \frac{B_{eq}}{B_\parallel^*} \frac{v_\parallel^2 + \frac{v_\perp^2}{2}}{R\Omega_s} \cos\theta \, \boldsymbol{e}_\theta \right)}_{\substack{\text{magentic curvature and} \\ \text{gradient drift } v_{\mathrm{c}+\nabla B}}}$$
$$+ \underbrace{\left(\frac{1}{B_\parallel^*} \frac{\partial \langle \phi \rangle}{\partial r} \boldsymbol{e}_\theta - \frac{1}{B_\parallel^*} \frac{\partial \langle \phi \rangle}{r \partial \theta} \boldsymbol{e}_r \right)}_{\text{electric drfit } v_{E\times B}} \quad . \quad (2\text{-}50)$$
$$+ \underbrace{\left(\frac{B_{eq} r v_\parallel}{B_\parallel^* q R_0} \boldsymbol{e}_\theta + \frac{B_{eq} v_\parallel}{B_\parallel^*} \boldsymbol{e}_\varphi \right)}_{\substack{\text{streaming in poloidal} \\ \text{and toroidal direction}}}$$

The subsequent terms in the three lines in right side of Eq. (2-50) streaming along the curvature drift $\boldsymbol{v}_c$ and grad-B drifts $\boldsymbol{v}_{\nabla \mathrm{B}}$ from the inhomogeneous equilibrium magnetic field, electric drift $\boldsymbol{v}_{E\times B}$ due to the perturbed electrostatic field $\boldsymbol{E}_1 = -\nabla\boldsymbol{\phi}$ and equilibrium magnetic field $\boldsymbol{B}_{eq}$, the streaming in poloidal and toroidal direction, respectively.

Furthermore, the total velocity can be split into equilibrium velocity and a small perturbated part as

$$\boldsymbol{v} = \boldsymbol{v}_0 + \boldsymbol{v}_1, \quad (2\text{-}51)$$

$$\begin{cases} \boldsymbol{v}_0 = \boldsymbol{v}_{\mathrm{c}+\nabla B} + \frac{B_{eq} r v_\parallel}{B_\parallel^* q R_0} \boldsymbol{e}_\theta + \frac{B_{eq} v_\parallel}{B_\parallel^*} \boldsymbol{e}_\varphi \\ \boldsymbol{v}_1 = \boldsymbol{v}_{E\times B} \end{cases}. \quad (2\text{-}52)$$

The zeroth order velocity consists of the magnetic drift (curvature drift $\boldsymbol{v}_c$ and grad-B drifts $\boldsymbol{v}_{\nabla \mathrm{B}}$) and the streaming along magnetic line. The perturbed electric field provides a 1st-order electrostatic drift.

As well as the acceleration along the equilibrium magnetic field is

$$\dot{\boldsymbol{v}}_\parallel = \dot{\boldsymbol{v}}_{\parallel,0} + \dot{\boldsymbol{v}}_{\parallel,1}, \quad (2\text{-}53)$$

where

$$\begin{cases} \dot{\boldsymbol{v}}_{\parallel,0} = -\frac{\frac{v_\perp^2}{2} B_{eq} r \sin\theta}{B_\parallel^* q R R_0} \\ \dot{\boldsymbol{v}}_{\parallel,1} = \frac{v_\parallel}{B_\parallel^* R} \left(\frac{\partial \langle \phi \rangle}{\partial r} \sin\theta + \frac{\partial \langle \phi \rangle}{r \partial \theta} \cos\theta \right) - \frac{\Omega_s}{B_\parallel^*} \left(\frac{1}{q R_0} \frac{\partial \langle \phi \rangle}{\partial \theta} + \frac{1}{R} \frac{\partial \langle \phi \rangle}{\partial \varphi} \right) \end{cases}. \quad (2\text{-}54)$$

The acceleration comes from the magnetic mirror force of the equlibrium magnetic field causing particle trapping in a weak magnetic field region and coulomb force from the

perturbed electric field.

In a similar way, the particle distribution function is divided into the equilibrium part $F_s$and perturbed parts δf_s.

$$f_s = F_s + \delta f_s, \tag{2-55}$$

where equilibrium distribution function is

$$F_s = \frac{m_s^{\frac{1}{2}}}{\sqrt{2\pi T_s^3}} \exp\left(-\frac{m_s v_\parallel^2}{2T_s} - \frac{\mu B}{T_s}\right). \tag{2-56}$$

Substituting the equations Eqs. (2-49), (2-54) and (2-55) into Eq. (2-38), we obtain the linearized Vlasov equation in electrostatic model:

$$\begin{aligned}
&\frac{\partial \delta f_s}{\partial t} + \frac{B_{eq}}{B_\parallel^*}\frac{v_\parallel^2 + \frac{v_\perp^2}{2}}{R\Omega_s}\sin\theta\,\frac{\partial \delta f_s}{\partial \boldsymbol{r}} + \frac{B_{eq}v_\parallel}{B_\parallel^* R}\frac{\partial \delta f_s}{\partial \varphi} \\
&-\left(\frac{B_{eq}}{B_\parallel^*}\frac{v_\parallel^2 + \frac{v_\perp^2}{2}}{Rr\Omega_s}\cos\theta - \frac{B_{eq}v_\parallel}{B_\parallel^* qR_0}\right)\frac{\partial \delta f_s}{\partial \theta} - \frac{\frac{v_\perp^2}{2}B_{eq}r\sin\theta}{B_\parallel^* qRR_0}\frac{\partial \delta f_s}{\partial v_\parallel} \\
=\ &\frac{1}{B_\parallel^*}\frac{\partial\langle\phi\rangle}{r\partial\theta}\frac{\partial F_s}{\partial \boldsymbol{r}} - \frac{1}{B_\parallel^*}\frac{\partial\langle\phi\rangle}{\partial r}\frac{\partial F_s}{\partial \theta} \\
&-\left[\frac{v_\parallel}{B_\parallel^* R}\left(\frac{\partial\langle\phi\rangle}{\partial r}\sin\theta + \frac{\partial\langle\phi\rangle}{r\partial\theta}\cos\theta\right) + \frac{\Omega_s}{B_\parallel^*}\left(\frac{1}{qR_0}\frac{\partial\langle\phi\rangle}{\partial\theta} + \frac{1}{R}\frac{\partial\langle\phi\rangle}{\partial\varphi}\right)\right]\frac{\partial F_s}{\partial v_\parallel}
\end{aligned} \tag{2-57}$$

2.3.2 Electromagnetic model

Gyrokinetic simulations of electromagnetic turbulence in magnetically confined plasmas is important for predicting the performance of fusion reactors but a great challenge in computational science due to multiple spatio-temporal scales related to electromagnetic ion and electron dynamics. The magnetic perturbation is proved to influence some key mechanisms of turbulent transport, including both linear instability and zonal flow production. The parallel component of the perturbed magnetic field and the finite beta term in the magnetic drift velocity are neglected by assuming that the plasma beta is not so high and does not affect the equilibrium.

The 5D GK Vlasov equation is used to describe the evolution of perturbed gyro-center distribution function δf_s [40] as:

$$\frac{\partial \delta f_s}{\partial t} + v_{\parallel} \boldsymbol{b}_{\boldsymbol{s}}^{*} \cdot \boldsymbol{\nabla} \delta f_s - \frac{1}{m_s} \mu \nabla_{\parallel} B \frac{\partial \delta f_s}{\partial v_{\parallel}} + \langle \tilde{v}_E \rangle \cdot \nabla \delta f$$
$$= -\boldsymbol{v}_{\mathrm{c}+\nabla B} \cdot \boldsymbol{\nabla} \left(\delta f_s + \frac{e_s}{T_{s\parallel}} \langle \phi \rangle F_s \right) - \frac{\boldsymbol{b} \times \boldsymbol{\nabla} \left(\langle \phi \rangle - v_{\parallel} \langle A_{\parallel} \rangle \right)}{B} \cdot \boldsymbol{\nabla} F_s \qquad (2\text{-}58)$$
$$- \frac{1}{m_s} e_s \langle E_{\parallel} \rangle \frac{\partial F_s}{\partial v_{\parallel}}$$

Comparing with the electrostatic model, the obvious difference is on the right side of the equation. In the second term at right side of Eq. (2-58), except for the velocity of the electrostatic drift in the electrostatic model, there is an extra streaming along the bent magnetic field line due to perturbed magnetic vector $\langle A_{\parallel} \rangle$. This term represents the parallel convection and is important for the Landau damping. The magnetic field line bending effect in this term will stabilize the ITG mode at finite beta. Not only that, but this additional perturbed magnetic vector also brings a perturbed induced electric field $-\frac{\partial \langle A_{\parallel} \rangle}{\partial t}$. Combined with the previous electrostatic field under the electrostatic model, the 1st-order acceleration, the third term at right side of Eq. (2-58), in the electromagnetic model is contributed together, where

$$\langle E_{\parallel} \rangle = -\boldsymbol{b}_{\boldsymbol{s}}^{*} \cdot \boldsymbol{\nabla} \langle \phi \rangle - \frac{\partial \langle A_{\parallel} \rangle}{\partial t}. \qquad (2\text{-}59)$$

On the ither hand, nonlinear interactions are preserved which are included in the convective derivative term by perturbed $E \times B$ flow $\langle \tilde{v}_E \rangle \cdot \nabla \delta f$ and in the parallel component of the spatial gradient with magnetic perturbation

$$\boldsymbol{b}_{\boldsymbol{s}}^{*} \cdot \boldsymbol{\nabla} \delta f_s = \boldsymbol{b} \cdot \boldsymbol{\nabla} \delta f_s + \langle \tilde{\boldsymbol{b}} \rangle_s \cdot \boldsymbol{\nabla} \delta f_s, \qquad (2\text{-}60)$$

where

$$\langle \tilde{\boldsymbol{b}} \rangle_s = -\boldsymbol{b} \times \boldsymbol{\nabla} \langle A_{\parallel} \rangle_s \qquad (2\text{-}61)$$

is the perturbed part of magnetic field. And note that the perturbed $E \times B$ drift velocity here is as same as it in electrostatic model without contribution from perturbed magnetic field $A_{\parallel}$.

$$\langle \tilde{v}_E \rangle = \frac{\boldsymbol{b} \times \boldsymbol{\nabla} \langle \phi \rangle}{B_{eq}}. \qquad (2\text{-}62)$$

ϕ is given by the GK quasi-neutrality condition,

$$\left\{e_i\left[1-\Gamma_0\left(k_\perp^2\rho_{i_T}^2\right)\right]\frac{T_{e_\parallel}}{T_{i_\parallel}}+e_e\left[1-\Gamma_0\left(k_\perp^2\rho_{e_T}^2\right)\right]\right\}\frac{\phi}{T_{e_\parallel}}= \iint\left[\frac{e_i\delta f_i}{m_i}J_0(k_\perp\rho_i)+\frac{e_e\delta f_e}{m_e}J_0(k_\perp\rho_e)\right]B_\parallel^* dv_\parallel d\mu \quad (2\text{-}63)$$

where $n_i = n_e \equiv n_0$ is assumed. Here $\rho_{s_T} = m_s v_{s_T}/e_s B$ is the Larmor radius evaluated with the thermal velocity v_{s_T}, so that ρ_i and ρ_e are the ion and electron gyro-radius, J_0 the Bessel function of the zeroth order, $\Gamma_0\left(k_\perp^2\rho_{s_T}^2\right) = I_0\left(k_\perp^2\rho_{s_T}^2\right)\exp\left(-k_\perp^2\rho_{s_T}^2\right)$, I_0 is 0th-order modified Bessel function. The first and second terms in the right-hand side are perturbed ion and electron densities, respectively. The non-adiabatic electron effect is included in the second term, which is essential to treat trapped electron dynamics. The parallel component of vector potential $A_\parallel$ is given by parallel Ampere's law,

$$-\nabla^2 A_\parallel = 4\pi\iint v_\parallel[e_i\langle\delta f_i\rangle_i + e_e\langle\delta f_e\rangle_e]B_\parallel^* dv_\parallel d\mu. \quad (2\text{-}64)$$

In our numerical simulation code, the time integration is made by the fourth-order Runge-Kutta method. The fourth-order finite difference method is used for the derivatives with respect to r, θ, and $v_\parallel$, and the Fourier expansion is used along the toroidal direction $f(r,\theta,\varphi,v_\parallel,\mu,t) = \sum_n f(r,\theta,v_\parallel,\mu,t)\exp(-in\varphi)$. The gyro-average is evaluated by using the Pade approximation $\langle f\rangle_s \approx \frac{f}{1+k_\perp^2\rho_{i_T}^2/4}$. The FLR equation is represented by $\left[1-\frac{\rho_{i_T}^2}{4}\left(\frac{\partial^2}{\partial r^2}-\frac{m^2}{r^2}\right)\right]\langle f\rangle_s = f$, and it is solved by using the Fourier expansion along the poloidal direction as well as Poisson equation and Ampere's law where m is the poloidal wavenumber.

Modify the F_0 and define Λ

On the other hand, the ECRH (NBI) will increase kinetic energy of electron (ion) on perpendicular/parallel direction. In addition, the Coulomb collision frequency is proportional to $T^{-3/2}$. At the high temperature achieved in thermonuclear fusion plasma, collisionless is acceptable widely. Therefore, the particle distribution in $v_\parallel$ is different from that in $v_\perp$, but we assume that the particle distribution still subjects to thermo-dynamic equilibrium distribution in velocity space. For describing this anisotropy, we introduce two temperatures, $T_\parallel$ and another is $T_\perp$, into physical model of Gyro-kinetic based Numerical Experiment of Tokamaks (GKNET). For describing the anisotropic temperature, the electron/ion temperature in equilibrium distribution

functions are modified as:

$$F_s = n\sqrt{\frac{m_s^3}{2\pi\left(\Lambda_s^2 T_{s_\parallel}^3\right)}}\exp\left[-\left(\frac{m_s v_\parallel^2}{2}+\frac{\mu B}{\Lambda_s}\right)\frac{1}{T_{s_\parallel}}\right], \tag{2-65}$$

where $\Lambda_s = T_{s_\perp}/T_{s_\parallel}$ is the ratio of perpendicular temperature to parallel temperature and $T_{s_\parallel}$ is kept unchanged.

2.3.3 Normalization

In order to facilitate numerical calculations, each variable must be normalized by using the corresponding reference quantities. A reference mass m_s, density n_0, electron/ion temperature $T_{i_0} = T_{e_0} = T_0$, and magnetic field B_0 is chosen artificially. Then we can define the reference thermal velocity and reference thermal Larmor radius

$$\begin{cases} v_{s_{T_0}} = \sqrt{\frac{2T_{s_0}}{m_s}} \\ \rho_{s_{T_0}} = \frac{\sqrt{2m_s T_{s_0}}}{B_0 e_s} \end{cases}. \tag{2-66}$$

$v_{s_{T_0}} = \rho_{s_{T_0}}\omega_{s_{c_0}}$, where $\omega_{s_{c_0}} = \frac{e_s B_0}{m_s}$ is the reference cyclotron (gyro) frequency. The reference quantities are used to define the dimensionless relative quantities

$$\begin{cases} n_s = \bar{n}_s n_0 \\ n_s = \bar{T}_s T_0 \\ v = \bar{v} v_{i_{T_0}} \end{cases}, \tag{2-67}$$

where the quantity with an overbar is normalized dimensionless quantity. The fluctuating fields are normalized as

$$\begin{cases} \phi = \bar{\phi}\frac{T_0}{e} \\ A_\parallel = \bar{A}_\parallel B_0 \rho_{i_{T_0}} \end{cases} \tag{2-68}$$

The time and the angular rotation frequency are normalized using the reference thermal velocity as

$$\begin{cases} t = \bar{t}\frac{R_0}{v_{i_{T_0}}} \\ \omega = \bar{\omega}\frac{v_{i_{T_0}}}{R_0} \end{cases} \tag{2-69}$$

Quantities		**Reference quantities**
Temperature	$T_{e,s}$	T_0
Density	n	n_0
Magnetic field	B	B_0
Spatial scale	R, a_0, r	$\rho_{i_{T_0}}$
Time scale, t	t	$R_0/v_{i_{T_0}}$
Parallel velocity space	$v_{\parallel}$	$v_{i_{T_0}}$
Magnetic moment	μ	$m_s v_{s_{T_0}}^2/2B_0$
Perturbed electrostatic potential	ϕ	T_0/e
Perturbed vector potential	$A_{\parallel}$	$B_0\rho_{i_{T_0}}$

The R_0 and a_0 are the major and minor radius of tokamak respectively.

Box size and mesh point

	Box size	**mesh point**
Minor radius	$0.8\bar{a}_0$	N_x
Poloidal direction	2π	N_y
Parallel velocity space	$\left(-\bar{v}_{\parallel,\max}, \bar{v}_{\parallel,\max}\right)$	N_v
Magnetic moment	$(0, \bar{\mu}_{\max})$	N_μ
Plasma time	$\bar{L}_t$	N_t

Since the equilibrium distribution function obeys Maxwell–Boltzmann distribution, so that the velocity is extended to infinity. The $\bar{v}_{\parallel,\max}$ is chosen for limiting the integral interval within the acceptable error range, as well as $\bar{\mu}_{\max}$. On the other hand, it is hard to solve such type of equation, Eqs. (2-57) and (2-58), several numerical schemes have been developed. Based on the Semi-Lagrangian approach, a splitting scheme by separating the convection dynamics along each coordinate in phase space was introduced [41], which is one of the explicit symplectic time integrations [42]. In this version of GKNET, we use 3D MPI decomposition for the (r, θ, μ) domain. The spatial derivatives in Eq. (2-57) or (2-58) are discretized through the fourth-order Morinishi scheme [43,44] and the time integration is performed using the fourth-order

explicit Runge–Kutta method.

And another point to note is the redefined equilibrium distribution function by introducing a ratio of perpendicular temperature to parallel temperature as Eq. (2-65). As the Fig. 2-3. shown, as the Λ increasing (decreasing), the distribution function will be extended (shrunk). The integration region $\bar{\mu}_{\max}$ and corresponding mesh point N_{μ} should be adapted to keep a conformal length interval in magnetic moment (perpendicular velocity) space.

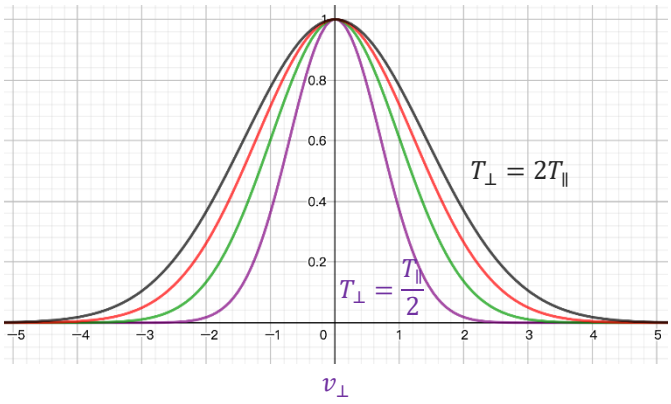

Fig. 2-3 The particle distribution function in perpendicular velocity space with anisotropic temperature: $\Lambda = T_\perp/T_\parallel$ is 0.5, 1.0, 1.5, 2.0.

As one can expect, this explicit method is very heavy, since it may require extremely small-time steps to prevent the error from diverging while implicit methods usually do not suffer from such strict limitations. To avoid the divergence of the error, time integration schemes must be used within their stability conditions, usually found through the so-called Courant-Friedrichs-Lewy (CFL) [45] condition. It is a necessary condition for convergence while solving certain partial differential numerically. As a consequence, the time step must be less than a certain time in many explicit time-marching computer simulations. In the GKNET, the more crucial term is poloidal direction which means that the length interval in poloidal direction $\Delta\theta$, time step Δt and streaming in Eq. (2-46) must satisfy with the relationship as follow:

$$\frac{d\bar{\theta}}{d\bar{t}} > \sqrt{\frac{m_i}{m_s}}\sqrt{\frac{T_{th_{0s}}}{T_{th_{0i}}}}\frac{\bar{v}_{\parallel,\max}}{q(\bar{r})} \Rightarrow \frac{1}{\Delta t} = \frac{\mathrm{N}_t}{\bar{L}_t} > \frac{\mathrm{N}_y}{2\pi}\sqrt{\frac{m_i}{m_s}}\frac{\bar{v}_{\parallel,\max}}{q(\bar{r})}. \tag{2-70}$$

Note that the streaming here has been normalized to a dimensionless relative quantity. The mass ratio is fixed in this study $\frac{m_i}{m_s} = 100$.

On the other hand, the equation (2-63) is 1D Fourier transformed along the φ direction and then 1D Fourier transformed along the θ direction after MPI_ALLtoALL transpose between the θ and φ directions. Then by using MPI_ALLtoALL transpose between the r and θ directions again, we can solve Eqs. (2-63) (2-64) in the (r, k_θ, k_φ) space, which has a tri-diagonal matrix form by applying the fourth-order finite difference method to the r direction. Note that the matrix is not decomposed along the r direction so that LU decomposition can be directly applied without any MPI communication. Note that the normalized magnetic moment μ as well as corresponding mesh point N_μ should change with Λ for ensuring the uniformity in integration of distribution function over magnetic moment space.

3 Finite-beta effect on linear micro-instability with anisotropic temperature

3.1 Introduction

In recent HL-2A experiment [32], an ion-ITB is formed around 60ms after NBI in almost flat q-profile region as shown in Fig. 3-1 (a)–(c). Flux-driven ITG (adiabatic electron) driven turbulence simulation with external momentum injection indicate the mean radial electric field induced by a co-toroidal rotation through the radial force balance plays an important role in sustaining ITB with flat q-profile [46], which is consistent with the HL-2A experiment. On the other hand, this ion-ITB is collapsed after ECRH and can't be rebuilt even terminated the ECRH, meanwhile, NBI was kept during the whole process. This phenomenon is also observed in JT-60U [47–49], DIII-D [50,51] and ASDEX Upgrade [52], whereas in these discharge experiments, the power of ECRH is lower than that of NBI. This is opposite to the shot 22388 in Hl-2A experiment.

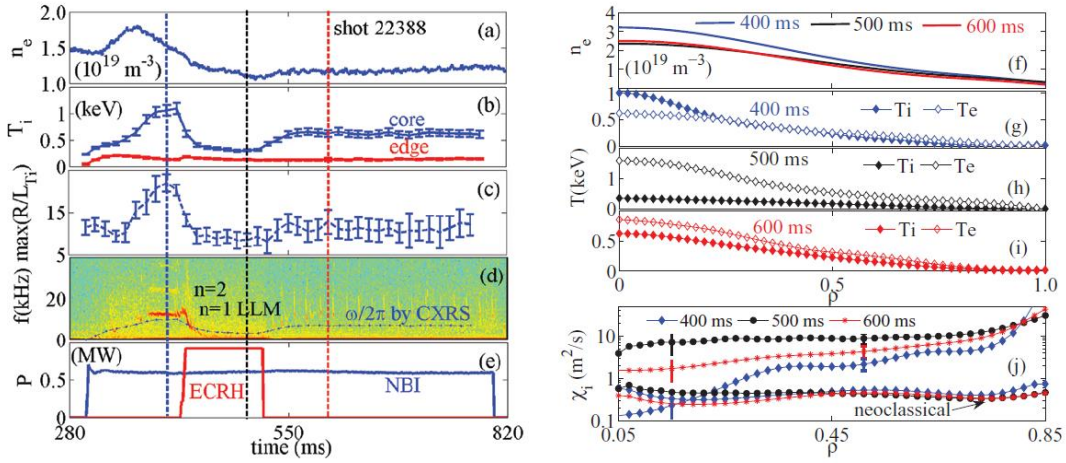

Fig. 3-1 Time traces of line averaged electron density (a), ion temperature (b), maximum normalized ITG (c), frequency of LLM and toroidal rotation (d), ECRH and NBI power (e); radial profiles of electron density (f) and temperatures (g)–(i) at 400, 500 and 600 ms, respectively; neoclassical and calculated ion thermal diffusivities at 400, 500 and 600 ms (j)

Temperature ratio T_e/T_i was considered to play a very important role in ITB formation: if $T_e/T_i \leq 1$ ITB can be observed otherwise cannot be formed, which is consistent with the viewpoint of M. Yoshida in positive magnetic shear plasma [53].

Moreover, H. Takenaga have confirmed that the temperature ratio T_e/T_i could not be a key parameter determining the ITB responses in reversed shear plasma [48]. The local gyrokinetic simulations studies using GKV [54,55] show that ITG modes were dominant in both positive and negative central shear plasmas with a low T_e/T_i, but the dominant mode switched from ITG to TEM in the positive shear region as T_e/T_i increased [53]. These investigations demonstrate that the ITB formation relates to the q-profile or magnetic shear. In the shot 22388 in Hl-2A experiment, there is a very weak magnetic shear in the core region. Therefore, these imply that TEM could play an important role for the ITB collapse, rather than the temperature ratio T_e/T_i, while the detail mechanism has not been studied yet.

In order to understand the which mode should be responsible for the onset and collapse of the ion-ITB in HL-2A plasma, we performed a series of linear global ITG/TEM simulations by utilizing a global gyrokinetic simulation code GKNET in both electrostatic [46,56,57] and electromagnetic [23,40] model. Our simulations have only computed a disturbance δf (gyrokinetic δf simulations) with respect to a given equilibrium function. On the other hand, the ECRH (NBI) will increase kinetic energy of electron (ion) on perpendicular direction. In addition, the Coulomb collision frequency is proportional to $T^{-3/2}$. At the high temperature achieved in thermonuclear fusion plasma, collisionless is acceptable widely. Therefore, the particle distribution in $v_{\parallel}$ is different from that in $v_{\perp}$, but we assume that the particle distribution still subjects to thermo-dynamic equilibrium distribution. For describing this anisotropy, we introduce two temperatures, $T_{\parallel}$ and another is $T_{\perp}$, into physical model of GKNET.

3.2 Linear analyses of micro-instabilities in HL-2A plasma

In this section, we perform linear analyses of micro-instability using parameters referring to HL-2A plasma by means of GKNET (electrostatic and electromagnetic) with full kinetic electron. In Sec. 3.1, at first, we study the micro-instability in HL-2A plasma. We found a new type of drift instability dominants the plasma before and after ECRH is applied. In all the following simulations, the equilibrium radial electric field is not taken into account for simplicity.

3.2.1 The parameters and initial profiles in HL-2A experiment

In the discharge of HL-2A, ion-ITB develops after NBI, but disappears shortly after ECRH is applied [32]. Through the fitting the experimental data by using the function

as

$$S(r) = \frac{a_S}{1+\left(\frac{r}{c_S}\right)^{b_S}}, \tag{3-1}$$

$$q(r) = 1.02 - 3.22\left(\frac{r}{a_0}\right)^2 + 6.93\left(\frac{r}{a_0}\right)^3. \tag{3-2}$$

Table 3-1 Main parameters in shot 22388 of HL-2A experiment

	n			T_i			T_e				
	a_n	b_n	c_n	a_{T_i}	b_{T_i}	c_{T_i}	a_{T_e}	b_{T_e}	c_{T_e}	ε	a_0
400 ms	3.17	2.59	80.45	0.99	2.15	42.49	0.60	2.82	71.18	0.24	162
500 ms	2.37	2.63	88.71	0.32	3.37	79.93	1.59	2.28	59.52	0.24	162

We get the equilibrium density, temperature and safety factor profile shown in Fig. 3-2, where $L_S = (d\ln S/dr)^{-1}$ is characteristic normalized gradient length of temperature or density. S is the density n or temperature $T_{i,e}$. The

Table 3-1 shows the main parameters at 400 ms (before ECRH) and 500 ms (after ECRH) in this shot which magnetic field strength is $B_0 = 1.31$T and the aspect ratio of HL-2A $\varepsilon = a_0/R_0 = 0.24$, where a_0 and R_0 are the minor and major radius respectively. They are normalized by the ion Larmor radius $\rho_{i_{T_0}} = \sqrt{m_i T_{i0}}/B_0 e_i$, $m_i/m_e = 100$. In our model, $T_{i0} = 1$KeV is used to normalize the electron and ion temperature and $n_0 = 10^{19}\mathrm{m}^{-3}$ is used to normalize the density. Concerning velocity space coordinates, we use the parallel velocity $v_\parallel$, which is given in units of $\sqrt{2T_{s0}/m_s}$ for species *s=i,e*, and the magnetic moment $\mu = m_s v_\perp^2/(2B)$ which is normalized accordingly. The ion temperature is relatively low, but its profile has a large gradient in core region due to the NBI heating, however it is reduced significantly after ECRH is applied even NBI is being kept. Accordingly, electron temperature become much higher through the ECRH, while the maximum of R_0/L_{T_e} becomes small. The density profile keeps steep, $R_0/L_n \sim 10$, especially in ITB phase before ECRH. Based on the experiment data, we also estimated the beta distribution over the minor radius as shown in Fig. 3-2 (e). The beta is reduced significantly after ECRH is applied.

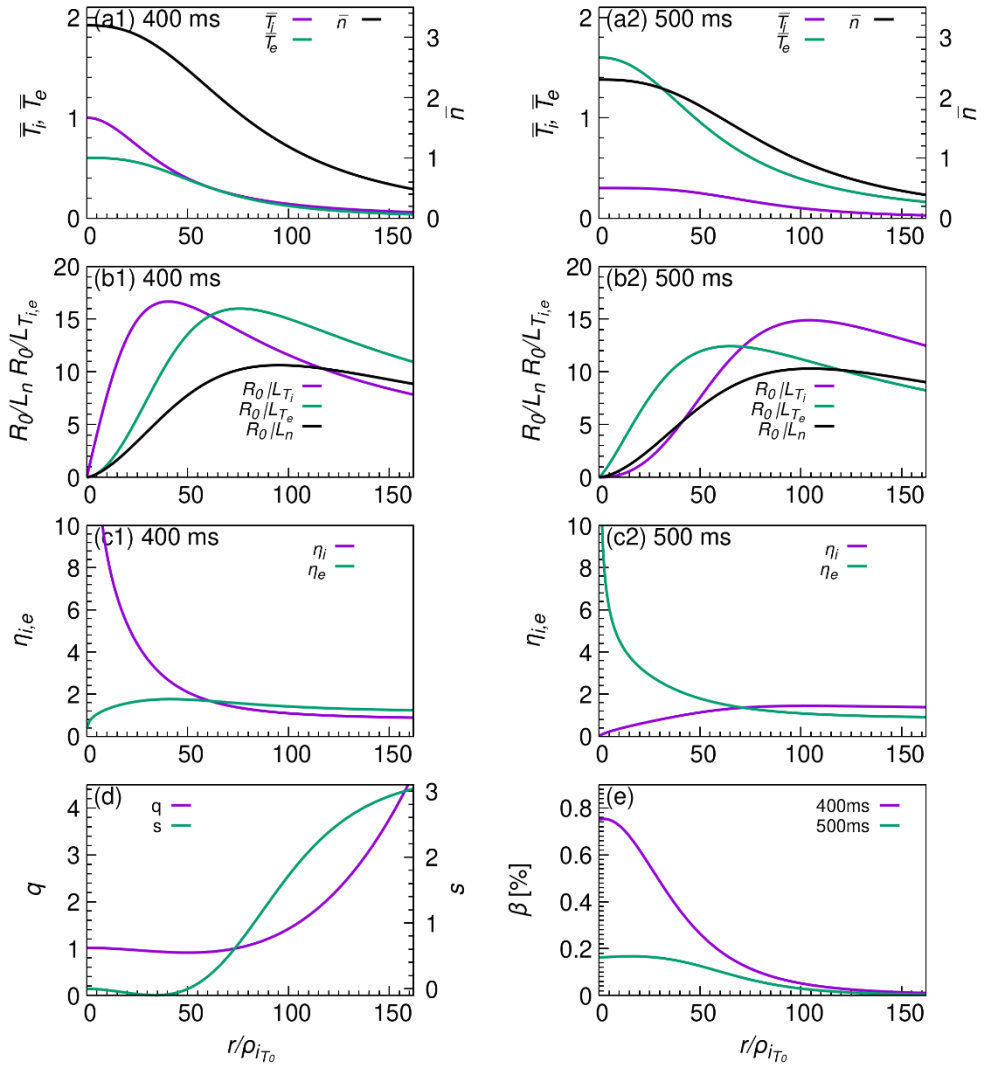

Fig. 3-2 The fitting temperature and density profiles at (a) 400 ms and (b) 500 ms, the fitting safety factor and (c) corresponding

3.2.2 Linear ITG/TEM simulation in electrostatic model

Based on the above two sets of parameters, we perform linear toroidal gyrokinetic simulations in electrostatic model first. Fig. 3-3 (a) and (b) show the real frequency and growth rate with respect to $k_\theta \rho_{i_T} = nq(r)\rho_{i_T}/r$ [58] estimated at $r = 70$, so that $k_\theta \rho_{i_T}$ is simply proportional to the toroidal mode number n. It is found that the real frequency is low and changes from positive to negative value continuously in ion-ITB phase (400 ms). This feature is different from the standard ITG mode and TEM which are characterized by negative and positive real frequency following the direction of ion and electron diamagnetic drift over the whole region of $k_\theta \rho_{i_T}$ in our model. After ECRH, the real frequency switch to positive (TEM side) but decrease with $k_\theta \rho_{i_T}$, which

is opposite to standard TEM [59]. So that the dominant mode still be considered as a same mode as that at 400 ms. On the other hand, the mode become more unstable due to the ECRH. The growth rate spectrums are peaked at $k_\theta \rho_{i_T}$~0.45 which is similar to standard ITG mode [60,61]. Fig. 3-4 (c1) and (c2) shows the electrostatic potential structures at 400 ms and 500 ms, respectively. It is found that they show nearly up-down symmetry on the poloidal cross section in both cases, which tilting angles from the mid-plane are nearly zero [22].

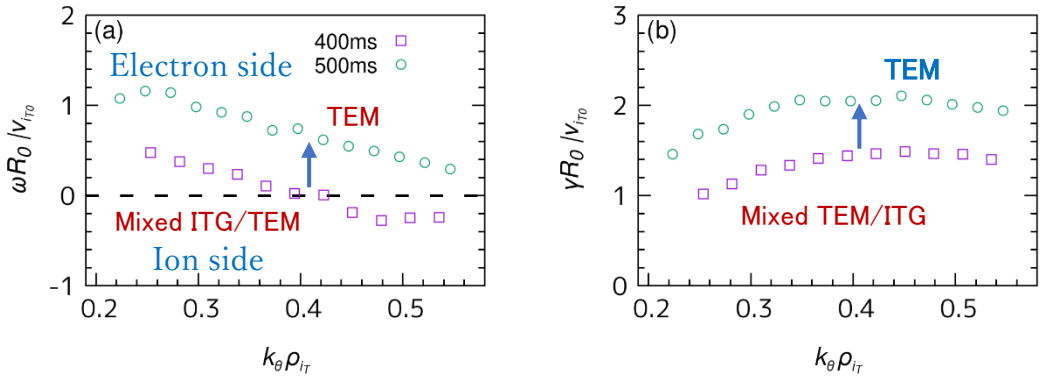

Fig. 3-3 (a) Real frequency spectrum and (b) linear growth rate spectrum.

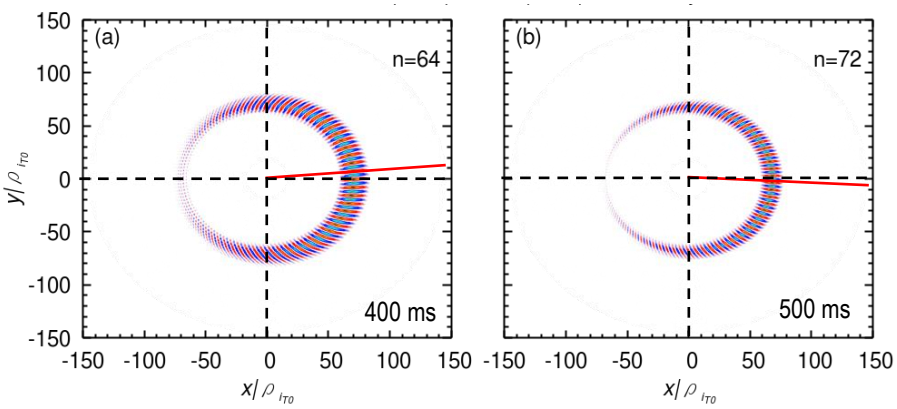

Fig. 3-4 The corresponding electrostatic potential structures with $k_\theta \rho_{i_T} = 0.44$ are shown in Fig (c1) and (c2).

3.2.3 Linear ITG/TEM simulation in electromagnetic model

Then, we examine this low frequency instability at finite beta, $\beta = \frac{n_0 T_{i0}}{B_0^2/2\mu_0}$, by using linear electromagnetic GKNET with non-adiabatic electron [23,40]. Fig. 3-5 (a)-(b) shows the normalized linear frequency and growth rate as a function of β for a toroidal

mode number n=36. It is notable that there is a discontinuity from positive side to negative side in the real frequency when beta value exceeds a threshold value of $\beta \approx 1.0\%$ whether in 400ms case or in 500ms case. The frequency changes from positive (TEM side) to negative (ITG side), and along with this change, the corresponding growth rate become to increase with increasing beta value more rapidly. Analogous to the results of electrostatic simulation, the real frequency shifts toward TEM side while the mode become more unstable due to the implementation of ECRH. The Fig. 3-6 shows the electrostatic potential ϕ and parallel component of vector potential $A_{\parallel}$ distribution on poloidal cross section when beta values are $\beta = 0.2\%$ and $\beta = 1.8\%$. The electrostatic potential ϕ profile exhibits a ballooning structure, which is the appearance of fluctuations in the unfavorable curvature region, for both the low and high beta value. An inconspicuous tilting angle of the mode with respect to the midplane, referred to as the ballooning angle is observed. The profile of the parallel component of vector potential $A_{\parallel}$ has opposite parity to the electrostatic potential along the magnetic field line so that it is weak in the unfavorable curvature region.

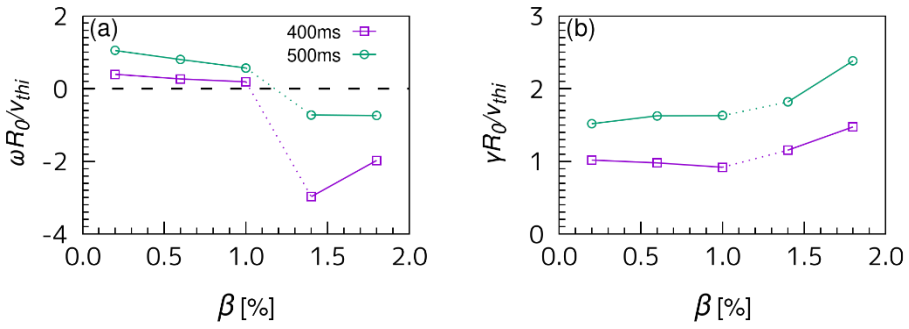

Fig. 3-5 (a) Real frequency and (b) linear growth rate as a function of β. The corresponding electrostatic and vector potential structures when n=36 are shown in (c)-(f).

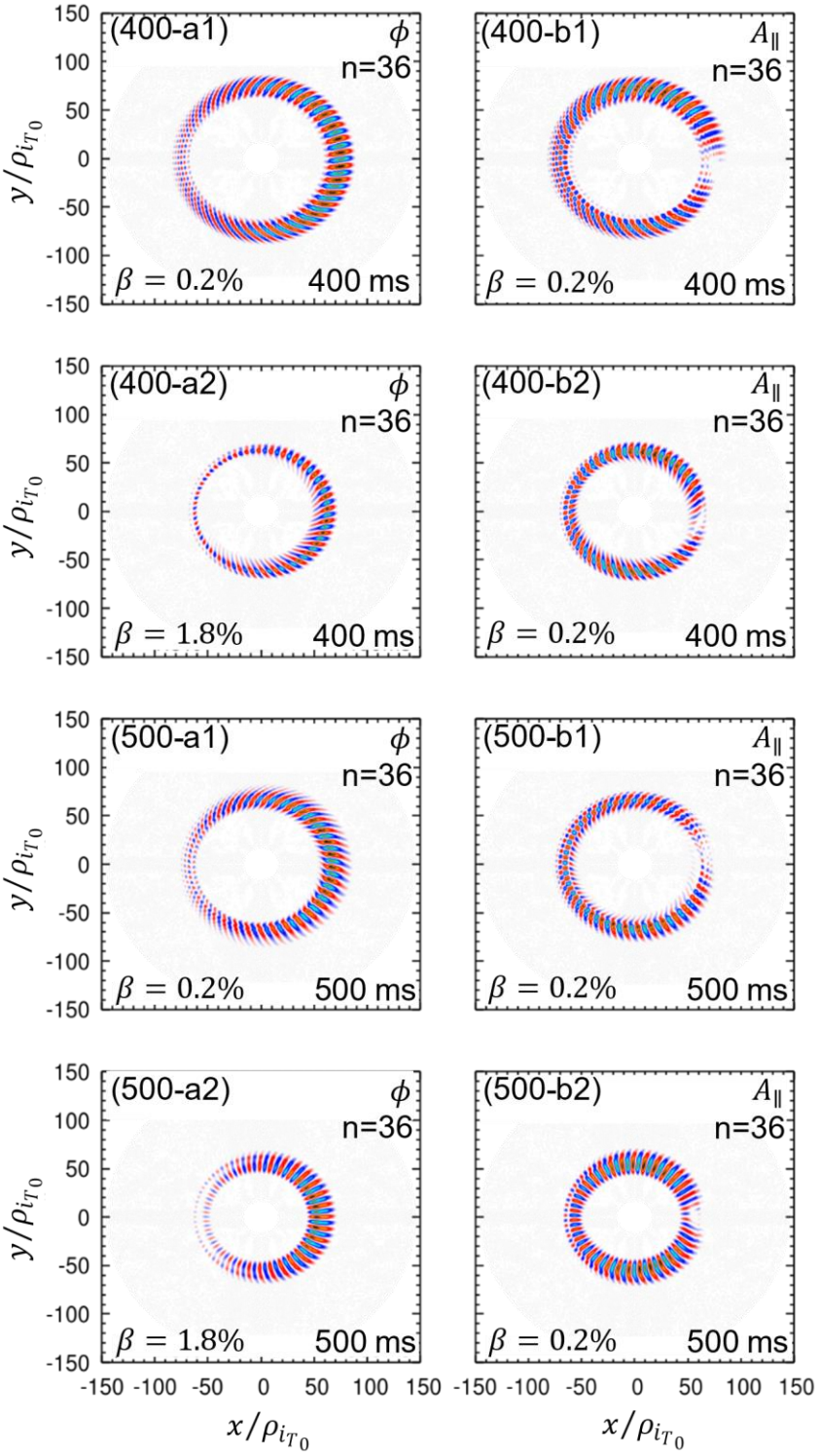

Fig. 3-6 (a) Real frequency and (b) linear growth rate as a function of β. The corresponding electrostatic and vector potential structures when n=36 are shown in (c)-(f).

3.3 Systematic study of linear modes targeting on HL-2A experiment

In order to study the nature of the mode with low frequency shown in Fig. 3-3, here we perform parameter scans for R_0/L_{Ti}, R_0/L_{Te} and R_0/L_n. The temperature and density profiles shown in Fig. 3-7 and the profiles are defined by function as

$$S(r) = \exp\left[-\frac{\Delta_S}{L_S}\tanh\left(\frac{r-0.5a}{\Delta_S}\right)\right] - \exp\left[-\frac{\Delta_S}{L_S}\tanh\left(\frac{0.5a}{\Delta_S}\right)\right] + 0.4 \qquad (3\text{-}3)$$

Table 3-2 Main parameters for parameter scan

Case	A	B	C1	C2	C3	C4
R_0/L_{T_i}	15.5	4.0	4.0			
R_0/L_{T_e}	4.0	15.5				
R_0/L_n	2.1	2.1	2.1	7.4	11.5	15.5
η_i	7.4	1.9	1.9	0.54	0.35	0.26
η_e	1.9	7.4				

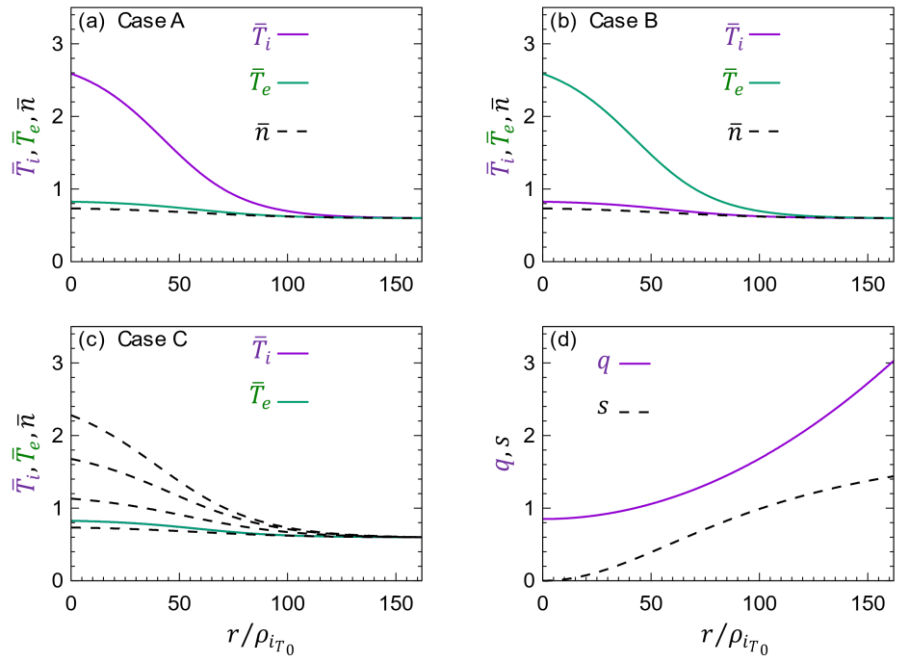

Fig. 3-7 The initial temperature and density profiles for (a) Case A, (b) Case B and (c) Case C. (d) is the safety and magnetic shear profile of cyclone base case for scan.

$\Delta_{T_i} = \Delta_{T_e} = 0.27$, $\Delta_n = 0.31$ in all cases and the reactor-relevant parameters are as same as HL-2A, $a_0 = 162$ normalized small radius, $\varepsilon = a_0/R_0 = 0.24$ aspect ratio. The other parameter sets are listed in Table 3-2. Case A has a steep ion temperature gradient ($R_0/L_{T_i} = 15.5$) and a flat electron temperature one ($R_0/L_{T_e} = 4.0$). Contrary to case A, case B has a steep electron temperature gradient ($R_0/L_{T_e} = 15.5$) and a flat ion temperature one ($R_0/L_{T_i} = 4.0$). Note that flat density gradient ($R_0/L_n = 2.1$) is set in both case A and B. On the other hand, in cases C1-C4, we change the density gradient ($R_0/L_n = 2.1, 7.4, 11.5, 15.5$), while keeping same relatively flat ion and electron temperature gradients ($R_0/L_{T_i} = R_0/L_{T_e} = 4.0$). In these scans, we use a safety factor profile in Cyclone Base Case [62] described by the function

$$q(r) = 0.85 + 2.18\left(\frac{r}{a}\right)^2 \tag{9}$$

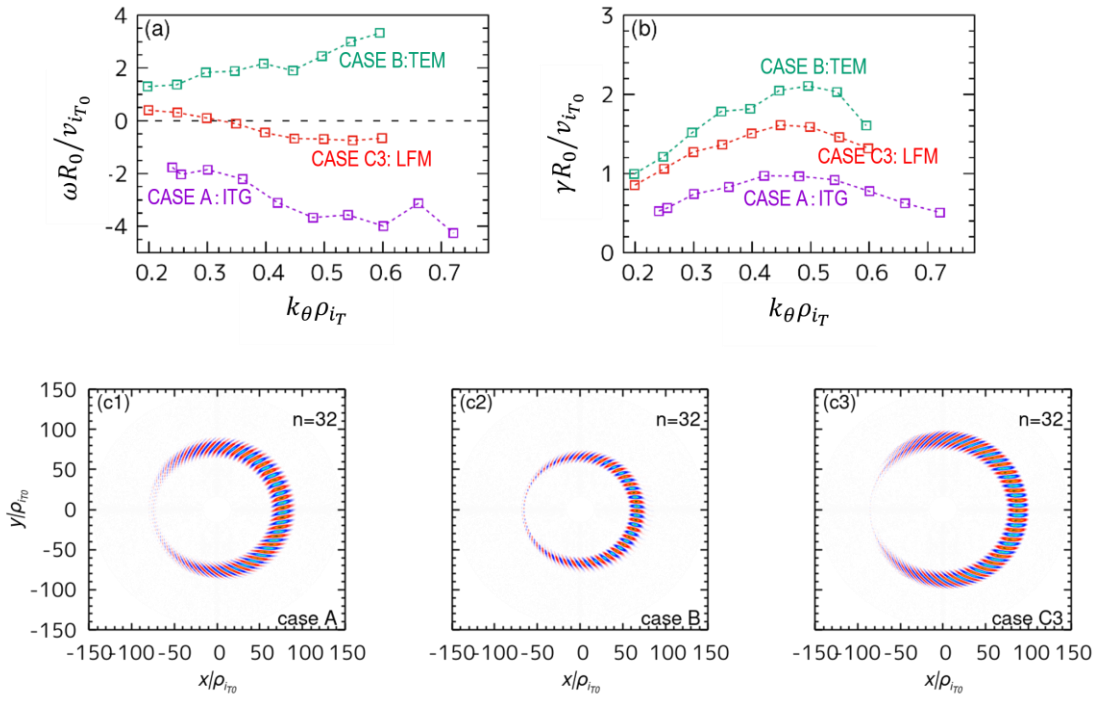

Fig. 3-8 (a) Real frequency and (b) linear growth rate as a function of the poloidal wavenumber $k_\theta \rho_{i_T}$ for case A, B and C3. The corresponding electrostatic potential structures are shown in (c1) - (c3).

Fig. 3-8 shows (a) real frequency and (b) linear growth rate as a function of $k_\theta \rho_{i_T}$

in case A, B and C3. In case A, we can see the characteristics of the standard ITG mode that the real frequency is negative which here means the ion diamagnetic direction, and the linear growth rate has a local maximum at $k_\theta \rho_{i_T}$~0.5. Meanwhile, in case B, the real frequency is positive and increase with $k_\theta \rho_{i_T}$. Additionally, the growth rate spectrum is peaked at $k_\theta \rho_{i_T}$~0.5. It is be considered to be the standard TEM. In Case C1, we observe no unstable mode. Whereas, in case C3 which has a steeper density gradient, modes with low frequency crossing zero should be pay attention, and the corresponding growth rates has a local maximum at $k_\theta \rho_{i_T}$~0.45. it is similar to the simulation results by using HL-2A parameters in Fig. 3-3. Fig. 3-8 (c1), (c2) and (c3) show electrostatic potential structures corresponding to case A, B and C3, respectively. We can see that the titling angle is positive in case A (ITG mode) while negative in case B (TEM), which results from the different signs of the real frequency of ITG mode and TEM in a global toroidal geometry.

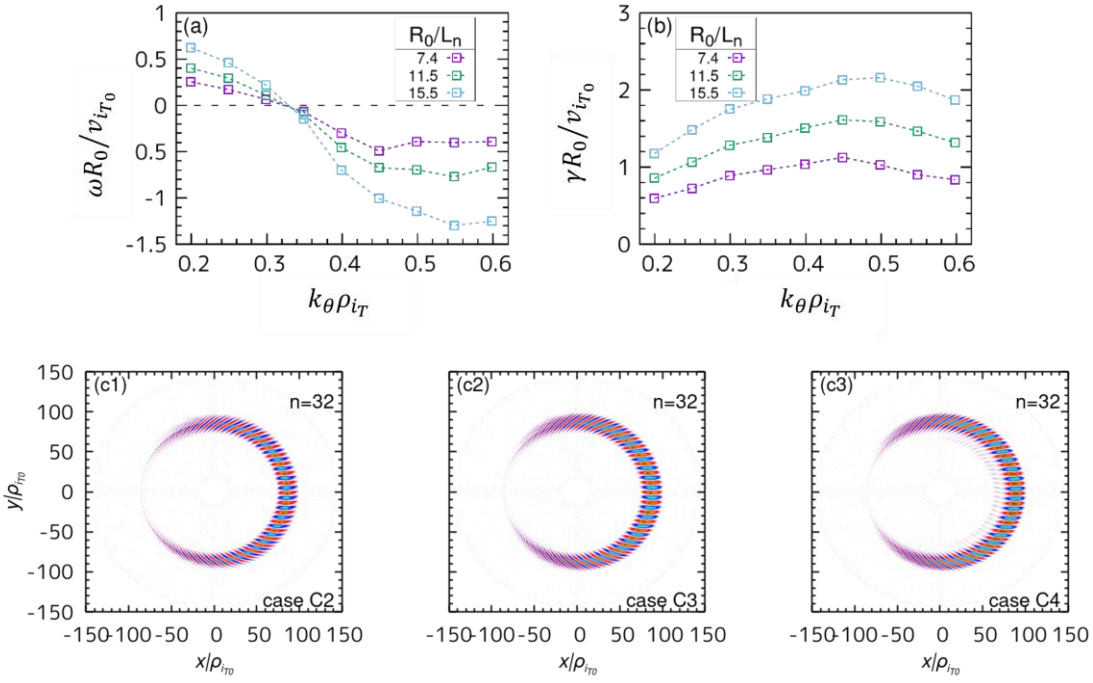

Fig. 3-9 (a) Real frequency and (b) linear growth rate as a function of $k_\theta \rho_{i_T}$ for case C2-C4. Corresponding R_0/L_n are 7.4, 11.5, 15.5. The electrostatic potential structures of case C3, C4 is shown in (c1-c2) with $k_\theta \rho_i = 0.6$.

Fig. 3-9 shows (a) real frequency and (b) linear growth rate in case C2-C4. From Fig. 3-9 (a), we can see that the feature of real frequency crossing zero become more obvious as density gradient increasing. Specifically, the positive part of real frequency

shifts to deeper positive and negative part shifts to deeper negative. On the other hand, the growth rate is enhanced significantly and its maximum value shifts to the high-$k_\theta \rho_{i_T}$ region. Therefore, this kind of low frequency mode(LFM) is considered to be induced mainly by the steep density gradient with small η_i and η_e which is also investigated by local eigen analysis [59]. It could have different feature from that of the standard ITG mode and TEM. In view of the appearance of this LFM in previous simulation using profiles at 400ms and 500ms in HL-2A experiment, the LFM should be responsible for the formation and collapse of ITB. Thereby, it is crucial that how this LFM respond to ECRH and NBI.

Furthermore, we compare it with standard ITG mode and TEM in electromagnetic model as shown in Fig. 3-10. In case A, The ITG mode is unstable at low beta value, while the KBM is unstable at high beta value, as expected. The stabilization of magnetic fluctuations on the ITG mode becomes prominent with increasing beta value, but there is little effect on real frequency of ITG mode. Once beta value exceeds a threshold value of 1.4%, KBM becomes unstable, and the linear growth rate increases quite rapidly. The real frequency exhibits a negative sign, moreover, the amplitude of this frequency clearly exceeds the ITG frequency. The beta value dependence of the growth rate for the CBC is similar to that obtained from another global electromagnetic gyrokinetic simulation code [63]. On the other hand, the real frequency of TEM is independent on beta value like that of ITG mode. But it become more unstable along with being increased beta value. In the case C3, the real frequency is positive but low, but notably, the frequency decreases with beta value very slightly and has a tendency changing into negative in high beta region. Along with this switch, the growth rate changes from increasing with beta value to decreasing with beta value.

According to Ref. [59], there exists a different kind of TEM. It is driven by the density gradient with the essential role of trapped electrons, which is called as the density gradient driven TEM (ε_n-TEM). Interestingly, the real frequency of ε_n-TEM is low and often goes across zero. This characteristic is similar to the present mode observed in case C2-C4.

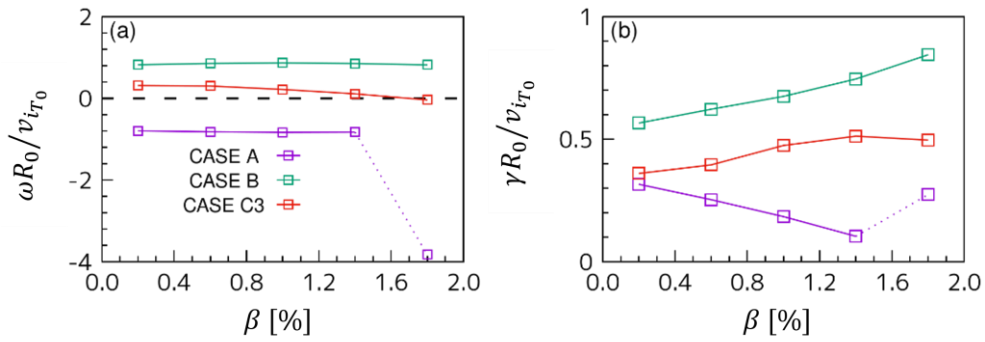

Fig. 3-10 (a) Real frequency and (b) linear growth rate as a function of β for case A(ITG mode), case B(TEM), case C3(LFM).

3.4 Anisotropic temperature effect

In Sec. 3.3, it is found that the density gradient is the main driven force for the present LFM which is considered to appear in the HL-2A experiment that the ITB being induced by NBI collapses after ECRH onset. In this subsection, The effect of anisotropic ion/electron temperature is studied to understand the role of auxiliary heating ,like ECRH ICRH NBI, in both electrostatic and electromagnetic model by changing the ratio, $\Lambda_s = T_{s_\perp}/T_{s_\parallel}$, from 0.5 to 2.0 in equilibrium distribution functions F_s, while parallel temperature, $T_{s_\parallel}$, is fixed.

3.4.1 Electrostatic simulations

Fig. 3-11 shows the effect of anisotropic temperature Λ_e and/or Λ_i on growth rate of the standard ITG (purple dotted line) TEM (green dotted lines), and LFM (red dotted lines), respectively. The linear growth rate spectrums of ITG mode show that that the growth rate of ITG mode is destabilized when increase the electron perpendicular temperature (from Λ_e = 0.5 to Λ_e = 2.0) but weakened when ion perpendicular temperature, $T_{i_\perp}$, become large. As regard the standard TEM, the growth rate has a strong sensitivity on electron perpendicular temperature, $T_{e_\perp}$, as the green dotted lines in Fig. 3-11 (a). It is enhanced by increase of $T_{e_\perp}$ obviously. Meanwhile, the corresponding instability is independent on $T_{i_\perp}$ completely as shown in Fig. 3-11 (b). That because the fraction of trapped electron becomes larger by increasing $T_{e_\perp}$. In addition, the higher $T_{e_\perp}$ leads to increase electron precession drift velocity, which usually makes TEM unstable. On the other hand, unlike the standard ITG mode and TEM, the growth rate of LFM shows a different tendency. The response to the $T_{e_\perp}$ is

similar to the standard TEM. Nevertheless, response to the $T_{i_\perp}$ is as same as ITG mode. The growth rate of LFM presents a hybrid feature mixing ITG mode and TEM.

Like to the response of growth rate, the real frequency of LFM also shows a hybrid feature as displayed in Fig. 3-12. As the purple dotted lines showing, the real frequency of standard ITG mode is not affected by anisotropic temperature. On the other hand, the real frequency of standard TEM is independent on anisotropic ion temperature totally but driven to positive side when $T_{e_\perp}$ is enhanced. As regard the LFM, along with the increase of $T_{e_\perp}$, the positive part of real frequency of prefer to shift to negative side (ITG side), meanwhile, the negative part shifts to positive side as TEM shown in Fig. 3-12 (a). The real frequency is driven to close to zero slightly. On the other hand, the dependence on the $T_{i_\perp}$ is shifts to negative side as Λ_i being changed from 0.5 to 2.0, furthermore the LFM is more sensitive to anisotropic electron temperature than ITG mode. In general, whether the change happens on $T_{e_\perp}$ or $T_{i_\perp}$, the real frequency of LFM tend to follow the ITG the response.

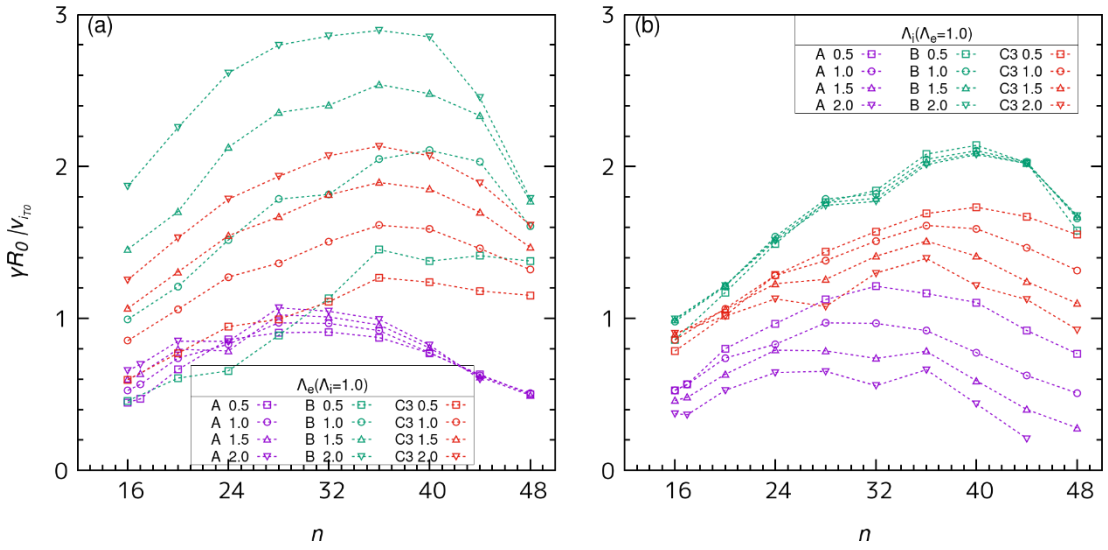

Fig. 3-11 linear growth rate as a function of n with different Λ_e or Λ_i. (a) changes Λ_e with fixing $\Lambda_i = 1$ and (b) changes Λ_i with fixing $\Lambda_e = 1$. Character 'A', 'B', C3' mean Case A (ITG mode), Case B (TEM), Case C3 (LFM) respectively.

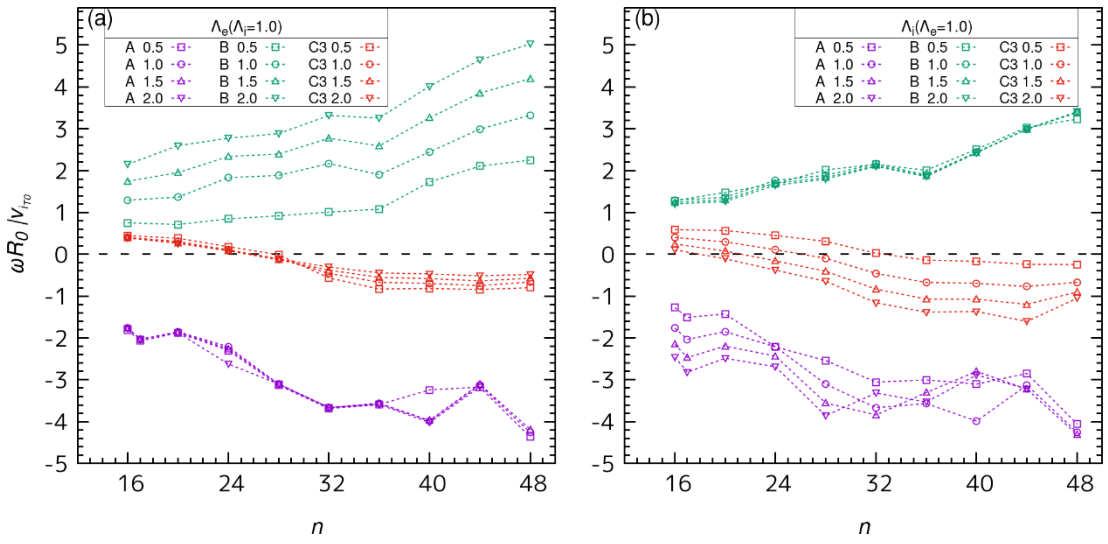

Fig. 3-12 Real frequency as a function of n with different Λ_e or Λ_i. (a) changes Λ_e with fixing $\Lambda_i = 1$ and (b) changes Λ_i with fixing $\Lambda_e = 1$. Character 'A', 'B', C3' mean Case A (ITG mode), Case B (TEM), Case C3 (LFM) respectively.

3.4.2 Electromagnetic simulations

First, let us see the beta dependence of case A, B, C3 on anisotropic temperature. Fig. 3-13 shows that there is a jump point in case A when beta value exceeds a threshold. According to the analysis of Fig. 3-10, this discontinuity is due to the transition from ITG mode to KBM as beta value increasing. Furthermore, anisotropy in electron temperature has limited effect on that transition, but the higher ion perpendicular temperature, $T_{i_\perp}$ facilitates the transition as the purple dotted lines with triangle shown in Fig. 3-13 (b) and Fig. 3-14 (b). When $\Lambda_i = 2.0$ the threshold for mode transition become smaller than 1.4%. As regard the response of TEM to anisotropic temperature, it is evident that there is no mode transition, but the electromagnetic destabilization is improved by higher electron perpendicular temperature, $T_{e_\perp}$.

In case C3, as the Λ_e increasing, the character of real frequency crossing zero continuously become more obvious, but the corresponding growth rate shows special beta dependence. The destabilization of beta effect on LFM is enhanced by increased Λ_e when the real frequency is positive. Once the real frequency changes to negative except for $\Lambda_e = 2.0$, the LFM will be stabilized by increasing beta value. When $\Lambda_e = 2.0$ and beta value change from 1.4% to 1.8%, the mode is considered to change to KBM which will be confirmed latter. the real frequency changes the sign from positive to negative continuously except for higher ion perpendicular temperature ($\Lambda_i =$

1.5, 2.0). The response of beta dependence of LFM to anisotropic ion temperature will give a clearer picture. As ion perpendicular temperature, $T_{i_\perp}$, increasing, the real frequency shifts to negative side. Notably, the real frequency jumps into deeper negative side for higher ion perpendicular temperature ($\Lambda_i = 1.5, 2.0$). considering the $\Lambda_i = 1.5$, when beta value exceeds 1.0%, the real frequencies are negative even with a jump. The corresponding growth rates decrease with beta continuously similar to beta dependence of ITG mode. On the other hand, when real frequency of LFM is positive in low beta region, the growth rate increase with beta which is as same as TEM. In higher $T_{i_\perp}$, e.g. $\Lambda_i = 2.0$, similar tendency is repeated. Whereas, when beta value changes from 1.4% to 1.8%, the growth rate increases rapidly even real frequency still negative, which indicates that the LFM change to KBM.

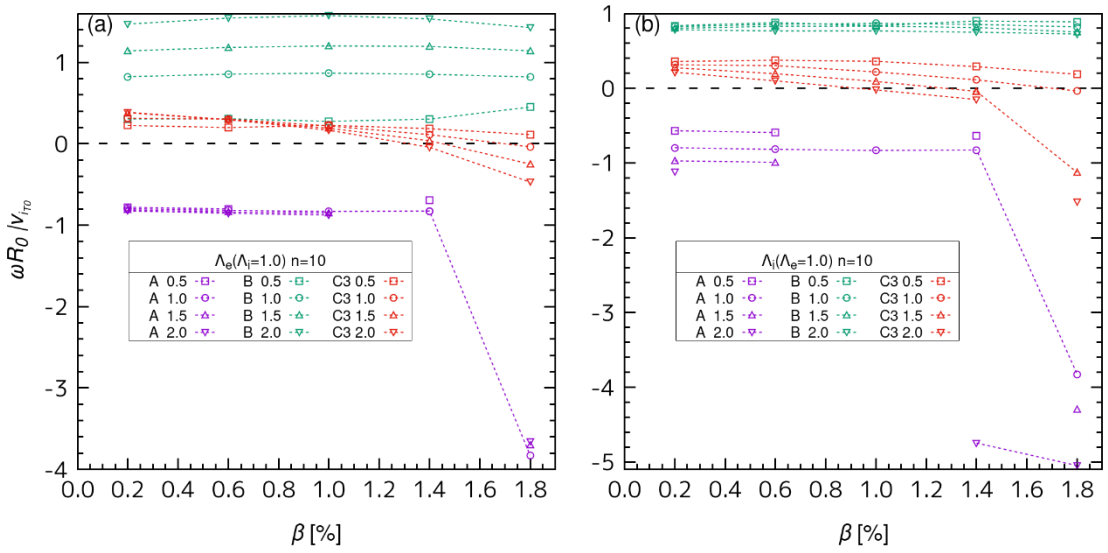

Fig. 3-13 The dependence of real frequency of given toroidal mode number $n = 10$ on β with different Λ_e or Λ_i. (a) changes Λ_e with fixing $\Lambda_i = 1$ and (b) changes Λ_i with fixing $\Lambda_e = 1$. Character 'A', 'B', C3' mean Case A (ITG mode), Case B (TEM), Case C3 (LFM) respectively.

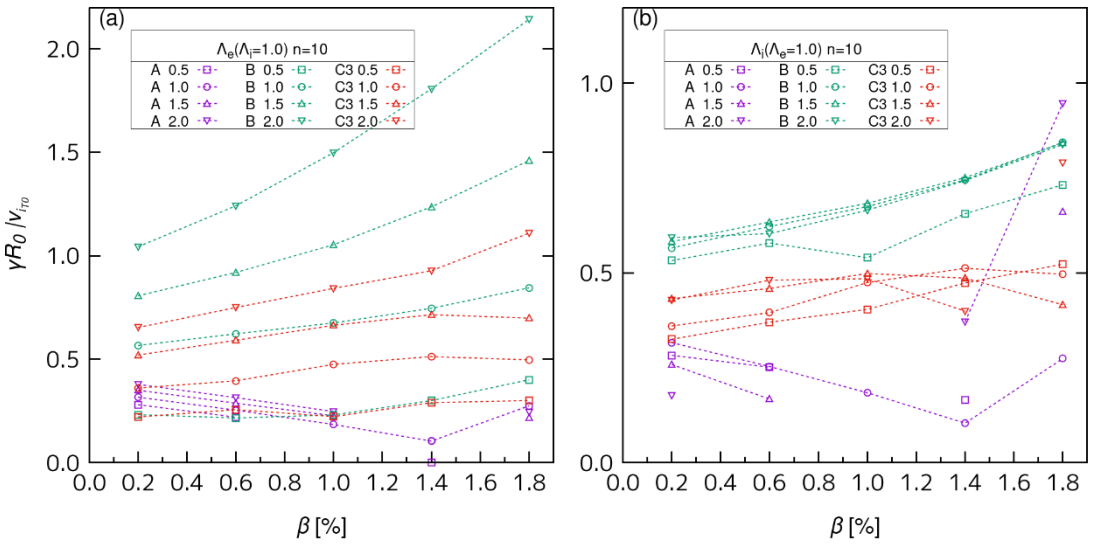

Fig. 3-14 The dependence of linear growth rate of given toroidal mode number $n = 10$ on β with different Λ_e or Λ_i. (a) changes Λ_e with fixing $\Lambda_i = 1$ and (b) changes Λ_i with fixing $\Lambda_e = 1$. Character 'A', 'B', C3' mean Case A (ITG mode), Case B (TEM), Case C3 (LFM) respectively.

In summary, the LFM shows a hybrid feature mixing ITG mode and TEM. Specifically, the LFM with positive real frequency destabilized by finite beta effect similar to standard TEM, correspondingly, the mode with negative real frequency is stabilized by magnetic fluctuation and change to KBM in high ion perpendicular temperature and high beta region.

For further comparing the $\Lambda_{i,e}$ dependence more simply in electromagnetic model, we just concentrate on the modes with low beta value $\beta = 0.2\%$ and/or high one $\beta = 1.8\%$. In case A, the low beta value means ITG modes (purple dotted lines with asterisks) and high beta value means KBMs (purple dotted lines with square) as shown in Fig. 3-15 and Fig. 3-16. The ITG modes with considering electromagnetic perturbation present a same $\Lambda_{i,e}$ dependence as that in electrostatic model. The KBM is independent on Λ_e, but when Λ_i is changed from 0.5 to 2.0 KBM become more unstable while the corresponding real frequency shifts to negative side more. The $\Lambda_{i,e}$ dependence of standard TEM in low and high beta region is kept same as it in electrostatic simulation which is unchanged with Λ_i. But increasing Λ_e would drive it to be more unstable, especially in high beta region, the enhancement of linear growth rate is significant. Comparing the red dotted lines with green dotted lines in Fig. 3-15, it is evident that, the low frequency instability is as same as the standard TEM which is

enhanced by increasing Λ_e whether the beta value is low or high. But as the Λ_e increasing, real frequency of LFM shifts toward TEM side in low beta region. On the contrary, shifts toward ITG mode side in high beta region, along with a mode change from LFM to KBM when Λ_e is increased from 1.5 to 2.0. If we keep $\Lambda_e = 1.0$ fixed and increase the ion perpendicular temperature, $T_{i_\perp}$, the LFM would be changed into KBM (when $\Lambda_i = 2.0$) in high beta region ($\beta = 1.8\%$). As the red dotted line with triangle displayed in Fig. 3-16, the amplitude of frequency clearly exceeds the LFM frequency when Λ_i exceeds 1.5, meanwhile, the corresponding linear growth rate is enhanced drastically. When $\Lambda_i \leq 1.5$ in in high beta region ($\beta = 1.8\%$), the low frequency instability is suppressed by increasing ion perpendicular temperature, $T_{i_\perp}$, similar to the response of ITG mode. On the other hand, the LFM with positive real frequency in low beta region ($\beta = 0.2\%$) does not present significant dependence on Λ_i like the standard TEM.

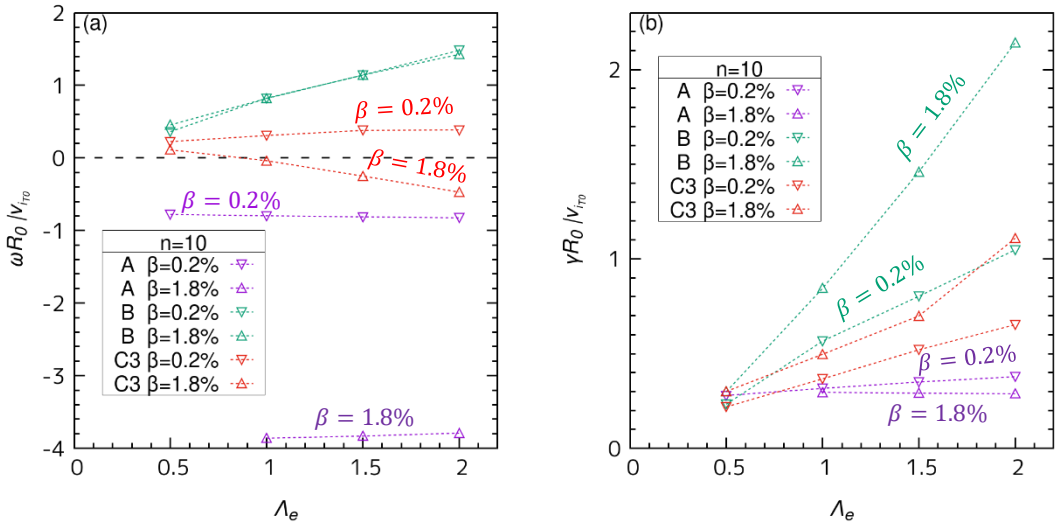

Fig. 3-15 (a) real frequency and (b) growth rate of given toroidal mode number $n = 10$ as a function of Λ_e in low $\beta_i = 0.2\%$ and high $\beta_i = 1.8\%$ when $\Lambda_i = 1$ is fixed.

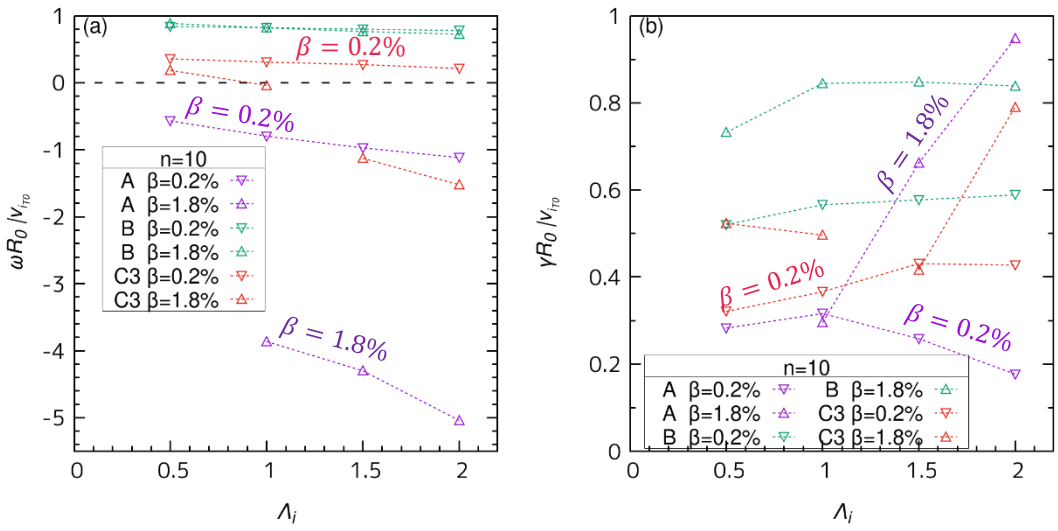

Fig. 3-16 (a) real frequency and (b) growth rate of given toroidal mode number $n = 10$ as a function of Λ_i in low $\beta_i = 0.2\%$ and high $\beta_i = 1.8\%$ when $\Lambda_e = 1$ is fixed.

3.5 Conclusion

In this work, we studied micro-instabilities referring the parameters in the HL-2A plasma with peaked density together with relatively flat ion and electron temperature profiles. an ion-ITB is found to be formed just after the onset of co-NBI in the almost flat *q*-profile region but collapsed after more powerful ECRH is applied. Considering kinetic electron dynamics in a global toroidal geometry, the linear gyro simulations presented a new type of density gradient driven drift mode which is expected to be responsible for the collapse of ion-ITB. The mode is destabilized by trapped electrons as TEM while exhibits different features as found from the study with anisotropic ion/electron temperature. The main characteristics are summarized as follow;

(1) the real frequency is close to zero and change the sign from electron diamagnetic direction to that of ion with the increase of $k_\theta \rho_{i_T}$, and the higher electron perpendicular temperature drives the real frequency to close to zero. (2) the growth rate is increased with larger density gradient, which is different from that of the standard ITG mode and TEM. (3) the instability is enhanced by being increased electron perpendicular temperature similar to the standard TEM, meanwhile suppressed by higher ion perpendicular temperature which is as same as ITG mode. (4) considering the electromagnetic perturbation, the LFM with positive real frequency destabilized by finite beta effect similar to standard TEM. Correspondingly, the mode with negative

real frequency is stabilized by magnetic fluctuation and change to KBM in high ion perpendicular temperature and high beta region like the ITG mode. in summary, the LFM shows a hybrid feature mixing ITG mode and TEM.

As a result, what could be acceptable is that: the presented low frequency instability was suppressed by NBI. This suppression is helpful to build the ITB. But the more powerful ECRH enhanced the instability even the NBI was being kept. This change made the ITB to be collapsed. We will perform more detailed analysis on LFM driven by the density gradient by changing other parameters such as aspect ratio and safety factor and compare the results with the local dispersion analyses [59]. Nonlinear simulation is also requested to understand the role of the mode on the transport in a future work.

4 The behavior of micro-instabilities in weak magnetic shear plasma

4.1 Introduction

In confined laboratory plasmas and those in space and astrophysical objects, linear instabilities due to specific free energy sources that intrinsically exist in each system, e.g. ion and electron temperature gradients, and their density gradients, sheared plasmas flows and rotations, etc., and their nonlinear evolutions leading to secondary and tertiary dynamics and structures including those of turbulence and various zonal modes and large scale eddies have been widely interested and intensively studied [58,64]. In magnetically confined toroidal systems such as tokamaks and stellarators targeting on fusion, they are of specific importance since they regulate plasma beta value [65], the ratio of plasma pressure and that of magnetic field, and confinement characteristics of the system, which are key parameters prescribing fusion performance.

Among various ingredients regulating such linear and nonlinear processes in a toroidal system, the structure of magnetic field characterized by the safety factor $q(r) \equiv (r/R_0)\, B_\varphi/B_\theta$ and magnetic shear $\hat{s}(r) \equiv r(\partial q/\partial r)$ plays a central role since they determine the mode structure predominantly. It is noted that long wavelength modes along the magnetic field line with $k_\parallel = -\delta\mu/qR \sim 0$ with $\delta\mu = (m - nq)$ tends to be survived due to a resonance nature between magnetic field and mode [58,65], where (m, n) denotes the poloidal and toroidal mode numbers, respectively.

In a standard operation, the q-profile exhibits a radially increasing function with the magnet shear of order unity, i.e. $\hat{s} \sim \mathcal{O}(1)$ [56] as we used in chapter 3. In such a case, micro-instabilities with so-called ballooning type eigen-mode are known to be excited by the successive coupling between adjacent resonant poloidal harmonics with the distance approximately given by $\Delta r_m \sim r/\hat{s}nq$ satisfying $\delta\mu \sim 0$ [66–68] due to the nature of a lattice symmetry of the system, where the mode is more unstable outside torus than inside with exhibiting a structure characterized by the radial envelop width Δr and tilting angle θ_t from the outside mid-plain, which represents up-down asymmetry structure determined from the first order ballooning theory due to the effect

of global profile variation [22,68]. The eigenvalue ω is determined from the local dispersion in the lowest order with respect to $1/n$ while the spatial structure in the first order by the global profile variation as $(\Delta r, \theta_t)$, the radial envelop width and tilting (Bloch) angle.

On the other hand, an advanced operation trying to access to high beta plasmas with ITB, which exhibit a steep pressure gradient in a limited radial region leading to a high confinement incorporated with a large fraction of self-induced bootstrap current, has been intensively studied [69,70]. In such an operation, magnetic field with a nearly flat safety factor (q) profile [21,32,71] in the core with vanishing magnetic shear, i.e. $\hat{s}$~0, and/or that with a revered q-profile [72–74], which changes the sign from $\hat{s}$>0 to $\hat{s}$<0 across the radius providing minimum safety factor value, i.e. $q = q_{min}$ at $r = r_{min}$ where $\hat{s}$=0, are found to be established. The optimum q-profile to realize such states have been discussed [71,75]. In such cases, the local ballooning theory and the related mode are hardly applied since no rigid factor to prescribe the mode exists in the lowest order due to the lack of resonance [26,76]. Instead, an infernal type non-resonant mode with $\delta\mu \neq 0$ is found to be excited not only in MHD regime driven by the pressure gradient causing a ITB collapse [27,29,77], but also in drift waves such as ion temperature gradient (ITG) modes, trapped electron modes (TEMs), kinetic ballooning modes (KBMs), leading to a turbulence regulating the transport [23,28]. However, the ballooning theory based on either local [78] or non-local [22,66,68] treatment is invalid since no counterpart to determine the eigenvalue ω in the lowest order exists, while higher order non-local effect associated with the global profile variation plays an essential role.

To contract the theoretical basis for exploring such an advanced operation, we study linear and non-linear dynamics with a nearly flat safety factor $q \sim q_c$ (constant) with the shear-free magnetic field, i.e. $\hat{s} \sim 0$, in a global toroidal system using the δf-based electromagnetic version of GKNET [23,40,46,56,57]. It is found that the infernal type non-resonant mode is excited predominantly and developed to a turbulence causing an order of magnitude large heat flux compared with that of normal q-profile. However, the linear dispersion and nonlinear spectrum show hardly deterministic complex corrugated structures, which is thought to reflect the non-local and/or global nature of the system.

Based on the hypothesis that the free energy driving non-resonant mode is regulated by the mismatch $\Delta\mu$, we present a law prescribing them by rearranging the toroidal mode number $\{n\}$ to Δn groups $G_{i=1-\Delta n}$ using the arithmetic progression $n_{Gi} \equiv \{i + \Delta n \cdot \ell\}$ with a common difference of Δn and the dispersion to same *primary groups*, where $i = (1,2\cdots,\Delta n)$ and $\ell = (0,1,2\cdots)$. Each primary group is further divided into sub-groups σ_{ij} with $j = (1,2\cdots)$ so as the free energy to be sequenced for the mismatch. Such a regrouped dispersion leads to a new class of turbulence expressed by the superposition of Δn sets of quasi-independent hierarchized spectra with different power laws due to the selective energy transfer among the groups. leading to quasi-coherent hierarchized structures, causing large heat flux. The radial extent of the regrouped dispersion σ_{ij} provides a measure of the effective radial correlation length ℓ_c of the turbulence [22,68,79].

4.2 The parameters and initial profiles

Here, we consider a large aspect ratio tokamak with concentric circular magnetic surfaces with no Shafranov shift. Temperature and density are given based on the following function as

$$F(r) = \exp\left[-\frac{\Delta_S}{L_s}\tanh\left(\frac{r-0.5a}{\Delta_S}\right)\right] - \exp\left[-\frac{\Delta_S}{L_s}\tanh\left(\frac{0.5a_0}{\Delta_S}\right)\right] + F_a \qquad (4\text{-}1)$$

by choosing $\Delta_{T_s} = 0.25$ and $R/L_{T_s} = 8.0$ for the temperatures, and $\Delta_n = 0.31$ and $R/L_n = 1.0$ for the density, where $L_{T_s} = -\partial \ln T_s/\partial r$ and $L_n = -\partial \ln n/\partial r$, respectively, which are shown in Fig. 4-1 (a). We also choose the inverse aspect ratio $a_0/R_0 = 0.36$, the normalized minor radius to average ion gyro-radius $a_0/\rho_{i_{T_0}} = 120$, the mass ratio $m_i/m_e = 100$.

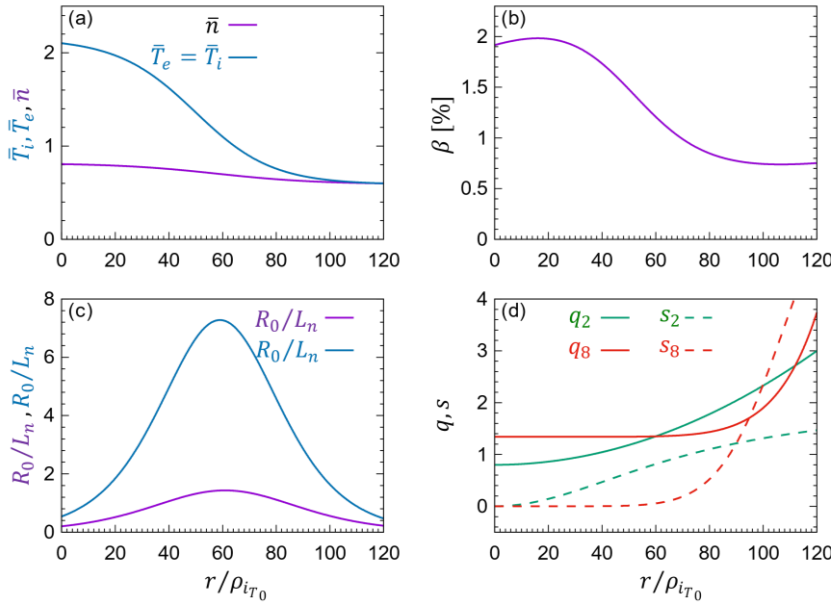

Fig. 4-1 (a) Distribution of initial temperature density, (b) corresponding beta profile, (c) scale length, R_0/L_{T_s} and R_0/L_n. (d) distribution of safety factor(solid lines) and magnetic shear(dash lines).

Here, we study plasma with a nearly flat safety factor profile given by $q_8(r) = q_c + c_8(r/a_0)^8$ with $q_c = 1.34$ and $c_8 = 2.4$ (q_8-case), and corresponding magnetic shear $\hat{s}(r) = r\,\partial \ln q/\partial r$ ($\hat{s}$-profile) as shown in Fig. 4-1 (d). The results are compared with the normal case given by $q_2(r) = q_0 + c_2(r/a)^2$ with $q_0 = 0.80$ and $c_2 = 2.2$ (q_2-case), where $\hat{s}\sim 0.8$ at the half-minor radius ($r/a_0 = 0.5$) where pressure gradient becomes maximum. On the other hand, the q_8-case leads to $\hat{s}\sim 0$ in the core, while it quickly increases toward the edge exceeding $\hat{s}\sim 1$ around $r/a_0 = 0.75$.

4.3 Linear analyses of micro-instabilities by using electromagnetic GKNET

4.3.1 The beta dependence of micro-instabilities

To identify the micro-instability of the plasma with a nearly flat q-profile, i.e. the q_8-case, we study the β-value dependence for (a) real frequency ω and (b) growth rate γ together with the case of normal q-profile for comparison, i.e. q_2-case, for the toroidal mode number to n =10, 11 and 20 as representatives, as shown in Fig. 4-2

The β dependences of electromagnetic instabilities within these two q-profiles are much different. In the normal q-profile similar to CBC, i.e. the q_2-case, we found

that at low beta values ($\beta < \beta_a$), the dominant micro-instability is an ITG mode as expected and its real frequency is negative ($\omega < 0$), which implies that the mode rotates toward the ion diamagnetic direction on a cross section of the torus. With increasing beta value, the growth rate γ of this mode is diminished, however, until a TEM takes over, while the absolute value of real frequency ω increases slightly. As the beta value continues to increase ($\beta_a < \beta < \beta_b$), TEM become dominant along with the frequency changing from negative to positive ($\omega > 0$). The growth rate γ of TEM is smaller than that of the ITG mode. As the beta value enters the higher region ($\beta > \beta_b$), a KBM starts to dominate and the growth rate γ increases quite rapidly once the respective beta threshold is crossed. The real frequency of KBM is negative ($\omega < 0$) and its amplitude clearly exceeds that of the ITG mode and TEM. The rotation direction of KBM is in the ion diamagnetic direction and as same as that of the ITG mode. The beta value that the mode changes the type, i.e. β_a and β_b, weakly depends on the toroidal mode number n as seen in Fig. 4-2 (a1) (b1), as

1) for $n = 10$: β_a~1.3% and β_b~2.1%
2) for $n = 11$: β_a~1.7% and β_b~2.3%
3) for $n = 11$: β_a~1.7% and β_b~1.9%

However, the dispersion shows a qualitatively similar feature with respect to the β-value. The growth rate and real frequency obtained in q_2-case is similar to those in the previous work [80,81] but the beta value for triggering mode change is higher in our simulations.

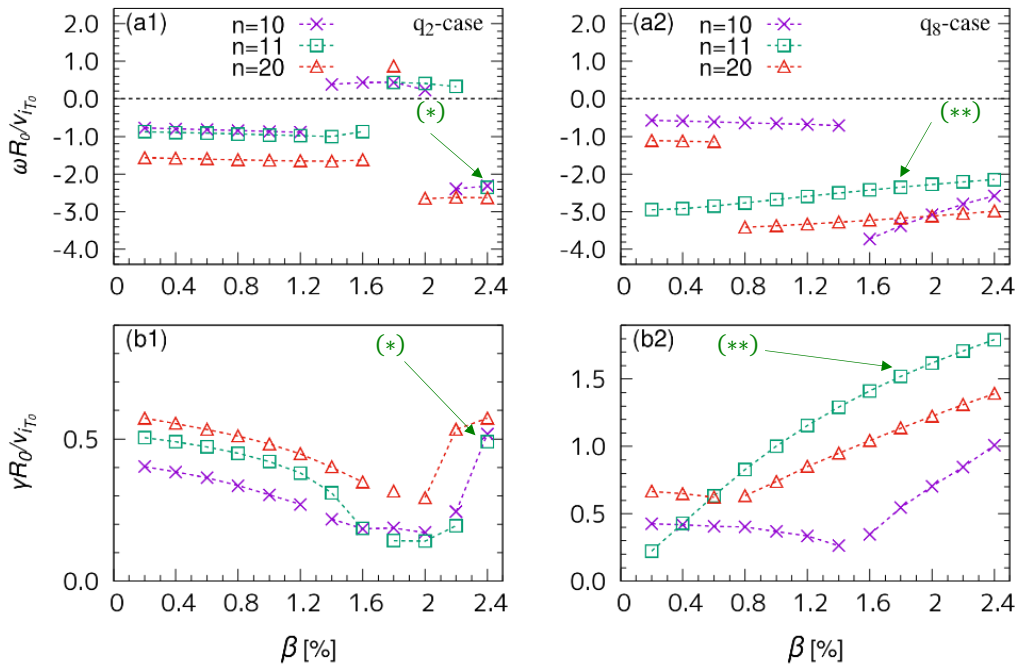

Fig. 4-2 . β-value dependence of real frequency ω and growth rate γ for q_2-case with normal profile in (a1) and (a2) and q_8-case with flat profille in (a2) and (b2) in the case n =10 (cross), 11(square) and 20 (triangle). Mode structure indicated by $(*)$ of $\beta = 2.4\%$ in (a1)(b1) and that by $(**)$ of $\beta = 1.8\%$ are shown in Fig.3.

Fig. 4-3 shows the profile of the eigenfunction of the ITG mode ($n = 10$) at $\beta = 0.2\%$, KBM at $\beta = 1.8\%$, KBM at $\beta = 2.4\%$ on a cross section. The electrostatic potential profiles in figures marked by '1' exhibit a ballooning structure, which is the appearance of fluctuations in the bad curvature region no matter ITG mode, TEM or KBM. And a tilting angle of the mode with respect to the midplane, referred to as the ballooning angle is observed which results from the global profile effect [22]. Since the ITG and the KBM both rotate toward the ion diamagnetic direction, their tilting angles are positive. On the contrary, the TEM's tilting angle is negative and more conspicuous than other two. The profile of the parallel component of vector potential along the magnetic field line $A_{\parallel}$ of these three kinds of mode have opposite parity to the electrostatic potential [82,83] , so that it is weak in the unfavorable curvature region as the figures marked by number '2' in Fig. 4-3. The figures marked by number '3' show the radial profiles of poloidal harmonics $\phi_m(r)$ which present a clear toroidal mode coupling. Other than that, the envelopes have a typical ballooning mode structure which is a set of toroidally coupled poloidal modes resonating at each rational surface located at $r = r_s$ that satisfies $q_2(r) = m/n$.

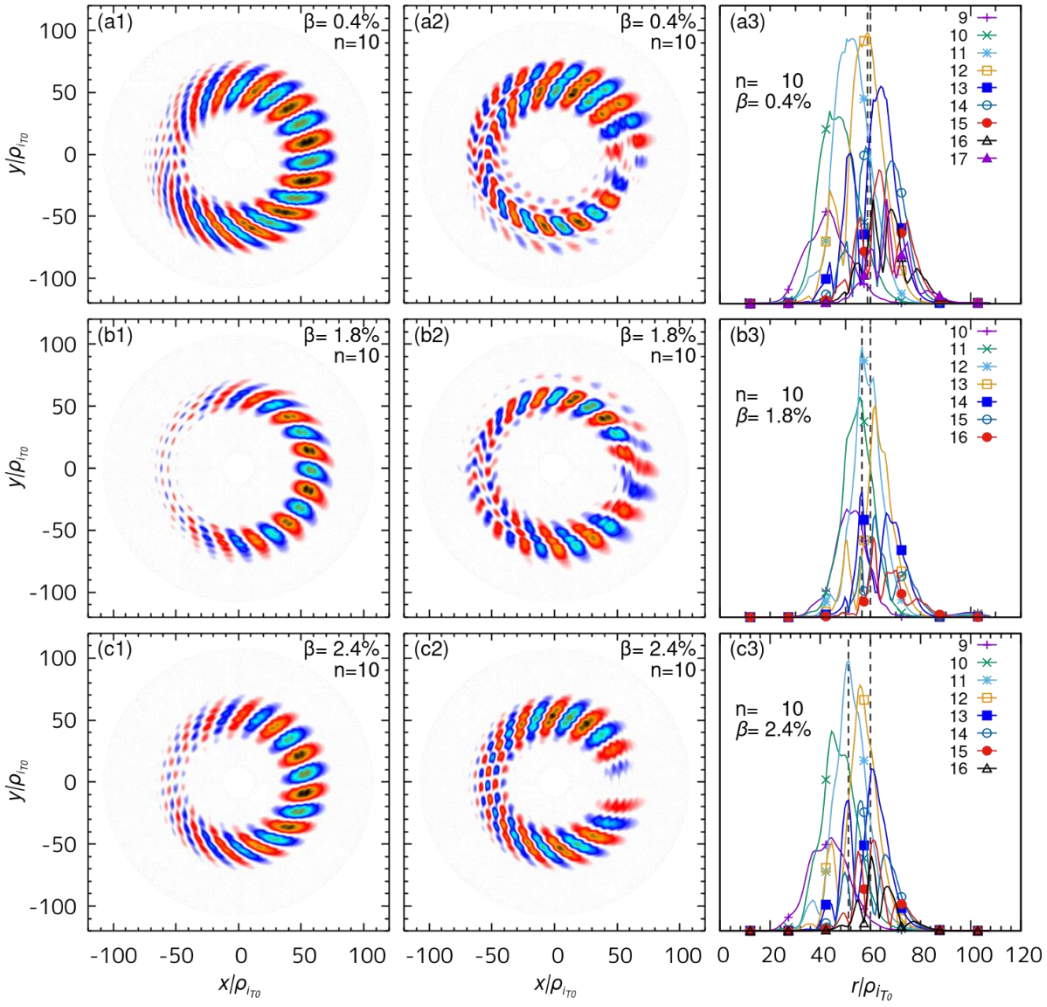

Fig. 4-3 The electrostatic potential marked by number "1", parallel component of vector potential marked by number "2" structure and the radial profile of the electrostatic potential of the eigenfunction marked by number "3" for mode n=10 in q_2-case: "a" ITG mode at $\beta = 0.4\%$, "b" KBM at $\beta = 1.8\%$, "c" KBM at $\beta = 2.4\%$.

On the other hand, when the q-profile become much flatter, like $q_8(r)$, the magnetic shear is almost close to zero. The beta dependence of micro-instabilities become complicated (Fig. 4-2 (a2) and (b2) respectively). For mode n=10, the linear growth rate decreases with increasing beta. When beta exceeds a threshold value $\beta_{c,10}$~1.6%, the growth rate increases with increasing beta. While the real frequency jump to a rather large region (negative side) and then its absolute value is decreased as β increasing. Even the behavior is similar to the characteristic of ITG mode changes to KBM with increasing beta value in q_2-case, however, the radial profiles of poloidal harmonics $\phi_m(r)$ in Fig. 4-4 (a3) or Fig. 4-5 (a3) does not present the ballooning mode structure. The corresponding sets of poloidal modes radially confined at a certain magnetic surface $r = 54.3$ for $\beta = 0.4\%$, $r = 50.6$ for $\beta = 1.8\%$. The $q(r =$

$54.3) \approx q(r = 50.6) \approx 1.34,$ These suggest that these poloidal harmonics are all non-resonant since they do not satisfy the relation $m = nq(r_s)$. From the figures marked by '3' in Fig. 4-4 and Fig. 4-5, these features are also observed in other modes $n = 11\ 20$ whether low beta ($\beta = 0.4$) or high beta ($\beta = 1.8$) and suggest that this kind of mode in q_8-case is an infernal type mode which is pointed out that the pressure gradient is the main force and is flat q profile is susceptible to it (either resistive or ideal) [25,30,84–86].

On the other hand, the characteristic of the next mode number $n = 11$ is found to be significantly different but simple. Both the real frequency and growth rate change with β monotonically and continuously. More specifically, the real frequency is reduced from a relatively large absolute value ($\omega < 0$) as beta increasing. Meanwhile, the growth rate is increased rapidly. And more notable point is that the instability ($n = 11$) is almost thresholdless in beta , as indicated by growth rate $\gamma \to 0$ when $\beta \to 0$. That means the dispersion is dominated by KBMs in whole beta region. Such a large difference of dispersion between even two adjacent toroidal mode numbers, i.e., $n = 10$ and 11, is of specific interest which is not seen in the q_2-case. Surprisingly, this feature can be seen in all other successive toroidal mode number, which we discuss later. It is also interesting to note that the dispersion for $n = 20$ return to that of $n = 10$, but the threshold $\beta_{c,20}$~0.8%, for mode switch is smaller than that for $n = 10$.

This different β dependence is also reflected in the mode structures on the poloidal cross section shown in Fig. 4-4 and Fig. 4-5. The modes $n = 10$, in both $\beta = 0.4\%$ and $\beta = 1.8\%$, are suppressed in good curvature region and prefer to the unfavorable curvature with a tilting angle. while the parallel component of vector potential $A_{\parallel}$ shown in figures (a2) of Fig. 4-4 and Fig. 4-5 presents opposite parity to the electrostatic potential along the magnetic field line [82,83] as the mode in q_2-case. The adjacent mode $n = 11$ is much different from mode $n = 10$ which shows that it is not affected by the finite toroidicity. In low beta region ($\beta = 0.4\%$), the electrostatic potential ϕ without the ballooning structure, shows nearly poloidal symmetry strong tilted in the counter-clockwise (ion-diamagnetic) direction as seen in Fig. 4-4 (b1) and so is the corresponding parallel vector potential $A_{\parallel}$ in Fig. 4-4 (b2), while the mode structure is broken up at both good and bad curvature. In the high region ($\beta = 1.8\%$), the tilting angle of the electrostatic potential ϕ shown in Fig. 4-5 (b1) becomes small comparing

with that of which beta vale is 1.8%, and the amplitude and radial mode width of electrostatic potential ϕ are larger and longer on the outside torus than those on the inner, showing the typical tendency of toroidal plasmas. On the other hand, the parallel vector potential $A_{\parallel}$ keep the same parity as it in low beta region ($\beta = 0.4\%$) even its the tilting angle also reduced.

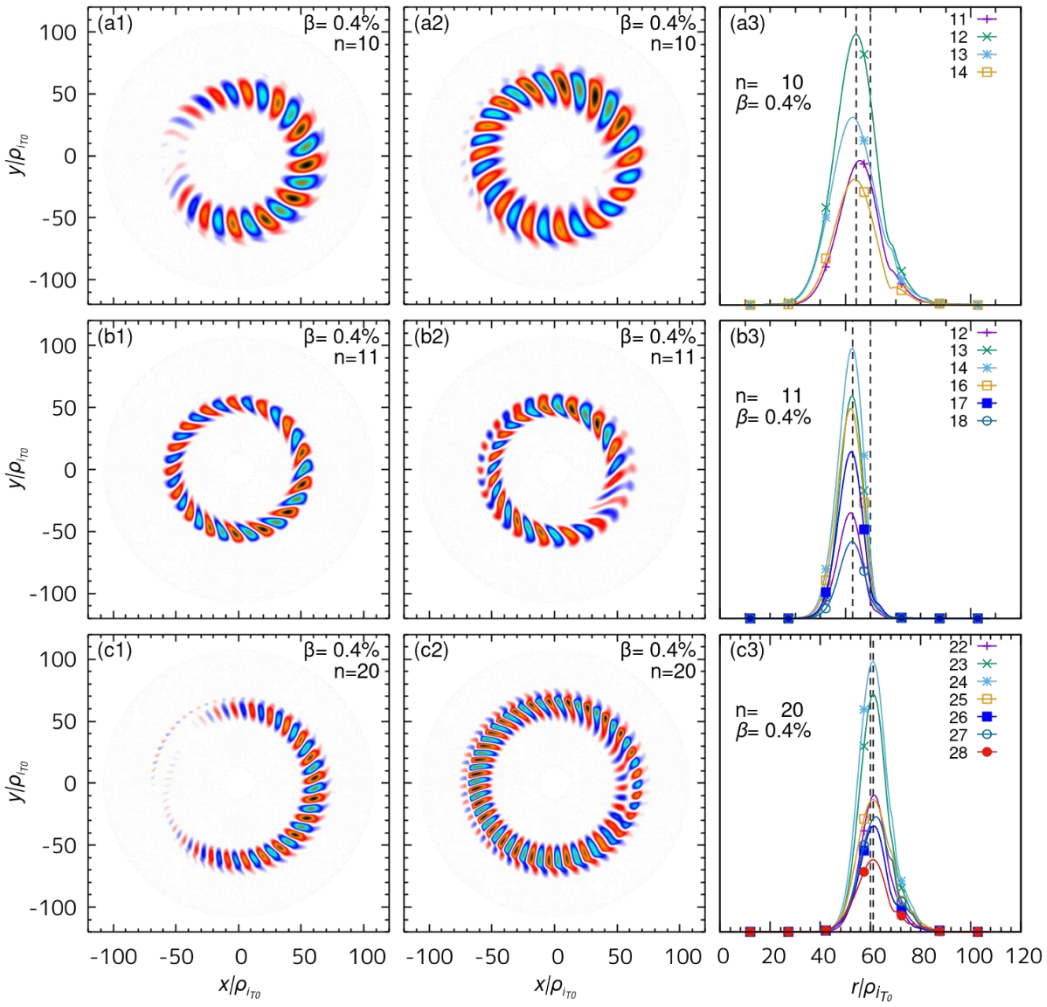

Fig. 4-4 The electrostatic potential marked by number "1", parallel component of vector potential marked by number "2" structure and the radial profile of the electrostatic potential of the eigenfunction marked by number "3" for mode $\beta = 0.4\%$ in q_8-case: "a" mode $n = 10$, "b" $n = 11$, "c" $n = 20$.

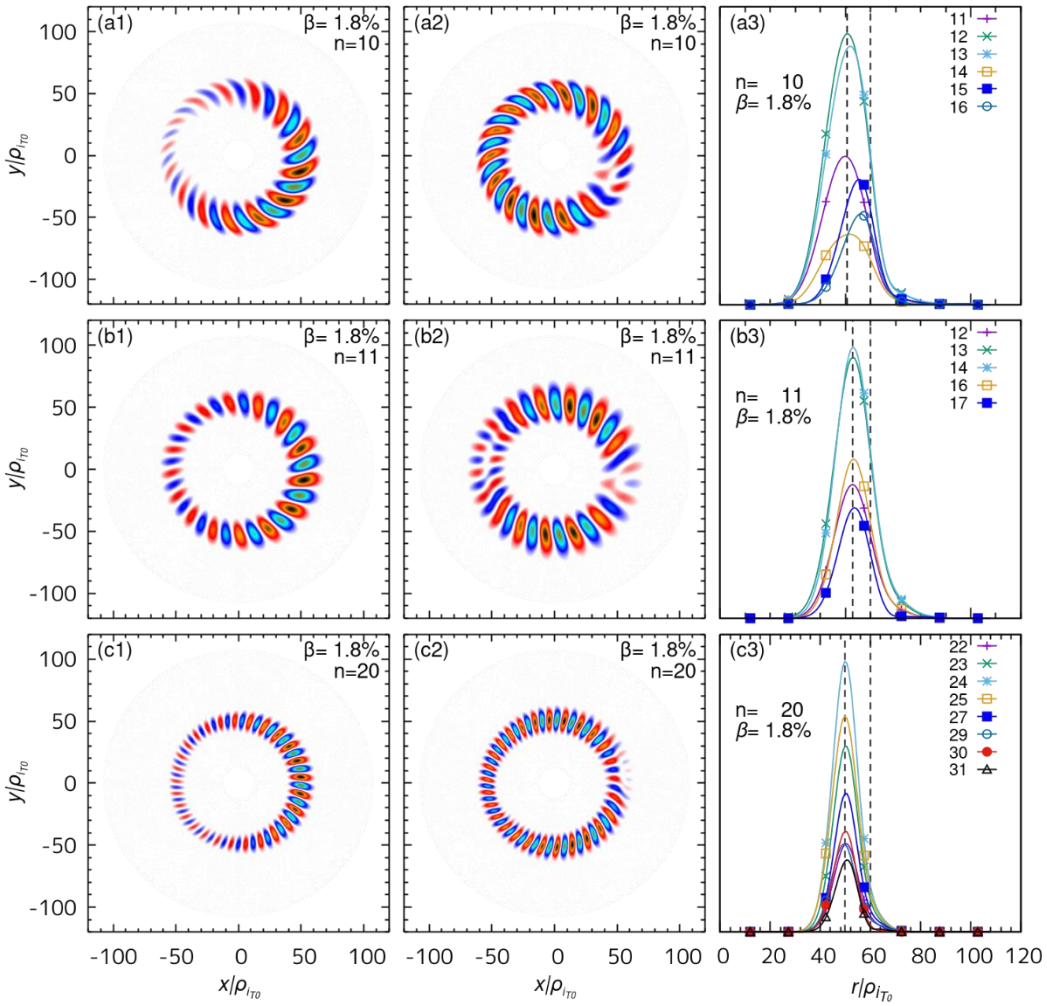

Fig. 4-5 The electrostatic potential marked by number "1", parallel component of vector potential marked by number "2" structure and the radial profile of the electrostatic potential of the eigenfunction marked by number "3" for mode $\beta = 1.8\%$ in q_8-case: "a" mode $n = 10$, "b" $n = 11$, "c" $n = 20$.

Through the above analysis, we mote that the observed infernal mode (IMs) [23] in the nearly flat q-profile driven by the pressure gradient is not dependent on the origin of free energy source, whether β-value is either ITG mode region or that of KBM. In order to measure of free energy driving instability for non-resonant mode in nearly flat q-profile, i.e., the mismatch from the resonance, we introduce the effective mode number in the poloidal direction, i.e. the number of wave in that direction M_θ. This is due to the fact that the poloidal harmonics m exhibit a distribution around the dominant Fourier harmonic m_0, which does not always coincide with the number of waves observed in the poloidal cross section due to the interference. Actually, $m_0 = 14$ is observed for $n = 11$ (see 4-5 (b2)), while $M_\theta = 15$ in Fig. 4-5 (a2). Then, using the effective mode number, we introduce two quantities representing the mismatch between

wave and magnetic field by the "mode number" difference $\Delta\mu \equiv M_\theta - nq_c$ and that of "helicity" $\Delta h \equiv M_\theta/n - q_c$. When $\Delta h > 0$ ($\Delta h < 0$), the magnetic helicity is larger (smaller) than that of wave. we define the mismatch from the resonance by $\Delta\mu \equiv M_\theta - nq(r_s)$. Applying to the q_8-case with $\beta = 1.8\%$, we found that $n = 10$ ($M_\theta = 14$) leads to γ~0.55 with $\Delta\mu$~0.58 and Δh~0.06, $n = 11$ ($M_\theta = 15$) to $\gamma = 1.60$ with $\Delta\mu$~0.23 and Δh~0.017, respectively, are obtained from Fig. 4-5 (also see Table 4-1 or Fig. 4-8). These results indicate that the smaller mismatch $\Delta\mu$ leads to larger growth rate without being sensitive to n and M_θ.

4.3.2 Discrete spectra with respect to toroidal mode number

For analyzing the beta effect on micro-instability more deeply, we investigated the linear real frequency and growth rate spectrum. Considering the great difference of beta dependence between mode $n = 10$ and $n = 11$ in q_8-case. The toroidal mode number is set to integers that changes continuously.

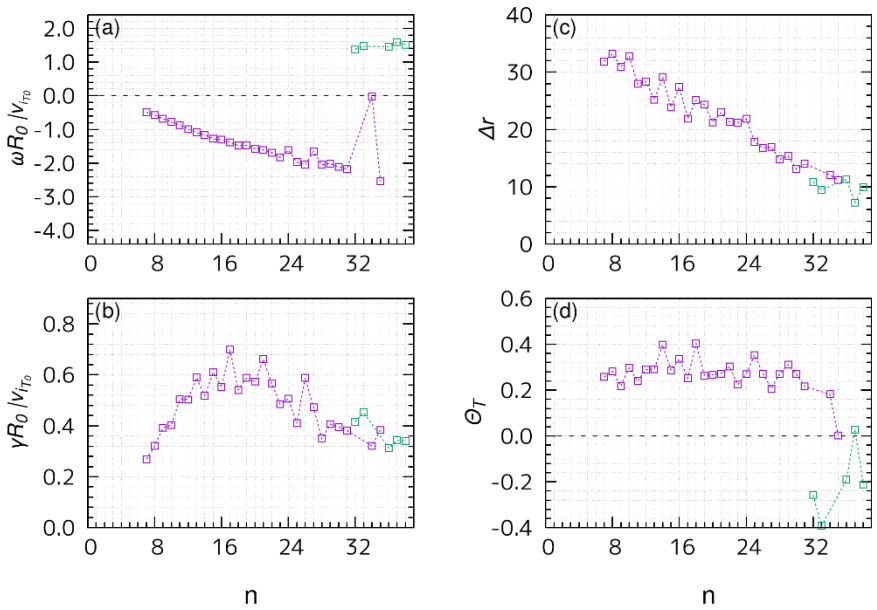

Fig. 4-6 (a) linear real frequency, (b) growth rate, (c) the mode width, (d) the tilting angle as function of toroidal mode number n for q_2-case when $\beta = 0.2\%$

For q_2-case, we selected a low beta value, $\beta = 0.2\%$, for simulations due to the modes could have a relatively large growth rate. The results are shown in Fig. 4-6. For $n \geq 7$, the ITG mode is unstable until TEM being driven, and its real frequency is changed as expected that increases proportionally toward ion diamagnetic direction as toroidal mode number n increasing. But the growth rate is shown to be an oscillatory

function of n, the toroidal mode number, treated as a continuous parameter. By investigating the electrostatic potential structures over poloidal cross section, we found that the oscillation also appears in mode width Δ_r and tilting angle θ_T as shown in Fig. 4-6 (c), (d). Furthermore, the higher growth rate corresponds to a narrower radial extension and smaller titling angle than those of adjacent modes. For example, in the modes $n = 13\ 14\ 15\ 16\ 17\ 18$, the odd modes are more unstable than the even modes. The corresponding mode width Δ_r is narrow and titling angle θ_T is small. On the other hand, the overall trend of change is in line with other ITG simulation that the linear growth rate is increased first and then reduced in general due to the finite Larmor radius (FLR) stabilizing effect.

To understand the nature of drift wave in a flat safety factor profile such as q_8-case observed in Fig. 4-2 (a2) and (b2), we study how the eigen frequency of the mode (ω, γ) and the radial location r_p change with the toroidal mode number n. The results are shown in Fig. 4-7 (a1), (b1) and (c1), respectively, where beta value, $\beta = 1.8\%$, is chosen as an example. Overall tendency of above quantities (green line) exhibits typical features of linear ion drift waves characterized by $k_\theta \rho_{i_T}$, which is proportional to the toroidal mode number n, i.e. the real frequency $|\omega|$ increases with n, while the growth rate γ shows a peak at n corresponding to $k_\theta \rho_{i_T}$~0.38 and is damped at larger n, and the mode location r_p shifts outward with n. However, we observe an oscillatory nature with respect to the toroidal mode number n, which is not seen in the normal safety factor profile such as q_2. This is considered to results from the non-resonant nature of infernal modes (IMs) discussed in Fig. 4-2 (a2) and (b2), where the form to extract instability free energy form the system is different from that in the resonance case. From the discussion in Fig. 4-2 (a2) and (b2), we found that the mismatch from the resonance, i.e. $\Delta\mu$, more sensitively influence on the eigen frequency (ω, γ) than the toroidal mode number n. This leads to an idea that a certain set of discreate toroidal mode numbers $\{n\}$ yield similar values of $\Delta\mu \equiv M_\theta - nq(r_s)$ as discussed in the following, which then provides continuous eigen frequencies with no discontinuity and/or jump. Note that M_θ is considered to be determined to minimize the mismatch to the value $|\Delta\mu| < 1$ to efficiently extract free energy of the instability.

Based on this idea, we assume that the safety factor with a weak magnetic shear is described by $q(r) = q_0 + q_\mu + \delta q(r)$, where q_0 is the constant integer whereas q_μ

is also the constant but that of non-integer residual. $\delta q(r)$ is the part that depends on the radus. In the present q_8-case, $q_0 = 1$ and $q_\mu = 0.34$ are given, while $\delta q(r) \propto r^8$, which is small in core region. It is then found that $\Delta\mu \equiv M_\theta - nq$ with satisfying $|\Delta\mu| < 1$ depends on the toroidal mode number n and the non-integer residual q_μ with proper effective polodal mode number M_θ. Then the dispersion is allowed to be rearranged to primary groups G_i, each of which is constituted by the descrete Δn sets of the toroidal mode number prescribed by the arithmetic progression with Δn as the common difference given by $n_{G_i} \equiv \{i + \Delta n \cdot \ell\}$ with $i = (1,2\cdots, \Delta n)$ and $\ell = (0,1,2\cdots)$, respectively. Here, we determine Δn from $1/q_\mu$ due to the condition $|\Delta\mu| \leq 1$.

In the present case, $1/q_\mu \sim 2.93$ is given, so that $\Delta n = 3$ is estimated, leading to three primary groups (G_1, G_2, G_3), each of which is prescribed by the set of toroidal mode number given by $n_{G1} = (1,4,7\cdots)$, $n_{G2} = (2,5,8\cdots)$ and $n_{G3} = (3,6,9\cdots)$, respectively as shown in Table 4-1. Fig. 4-7 (a2), (b2) and (c2) show same results as Fig. 4-7 (a1), (b1) and (c1) while each quantity is connected with respect to the arithmetic progression in each group for the toroidal mode number n_σ following the above rule. Here, it is noted that $n_{G_1} = 1$ and 4 in group A and $n_{G_2} = 2$ in group G_2 are absent since they are linearly stable modes.

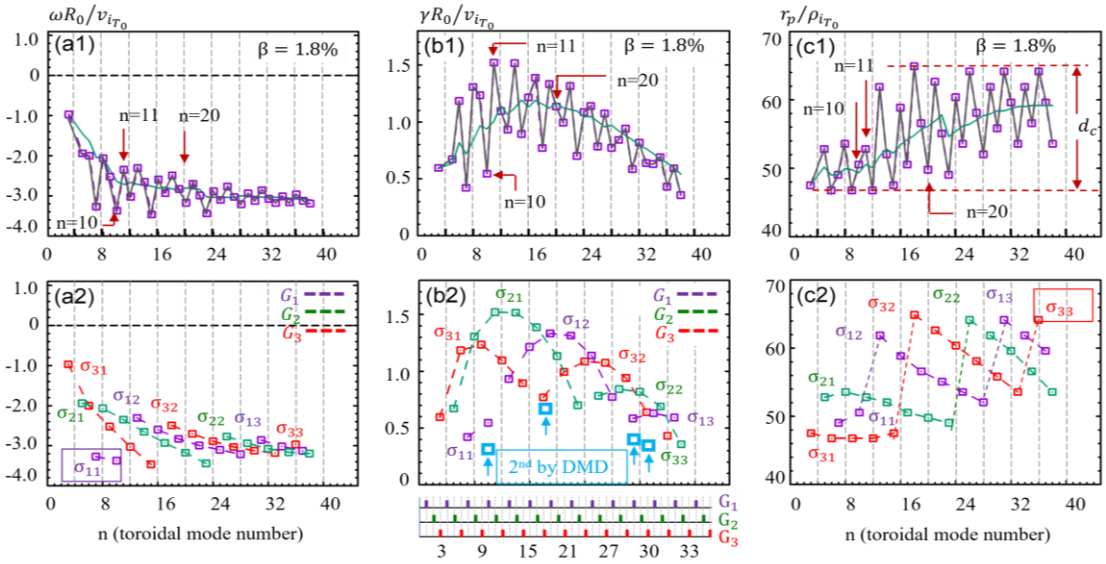

Fig. 4-7 'a' linear real frequency spectrum, 'b' growth rate spectrum and 'c' the radial position of the electrostatic potential of q_8-case for $\beta = 1.8\%$. The results that toroidal mode number is treated as consecutive integers are marked by number '1' in left side. The figures marked by number '2' in right side show the regrouped results.

It can be seen that oscillations in eigen-frequency (ω, γ) and the mode radial location r_p seen in Fig. 4-7 (a1), (b1) and (c1) disappear in each group, as expected, and then show continuous features except several discontinuities. The discontinuous jumps are seen in ω in Fig. 4-7 (a2) and r_p in Fig. 4-7 (c2) inside the primary group G_i as n_{G_i} changes, e.g. $n_{\mathrm{G}_1} = 10 \rightarrow 13$ and $28 \rightarrow 31$, $n_{\mathrm{G}_2} = 23 \rightarrow 26$, and $n_{\mathrm{G}_3} = 15 \rightarrow 18$, respectively.

This jump is thought to be the discontinuous change of the mismatch $\Delta\mu$ in each primary group. This can be seen in Table 4-1, which shows the value of $(\Delta\mu, M_\theta, r_p)$ for three primary-groups (G_1, G_2, G_3) with regrouped toroidal mode number $\left(n_{G_1}, n_{G_2}, n_{G_3}\right)$. Combining the discussion in Fig. 4-2 that the instability free energy source is regulated by the mismatch value. Therefore, assuming that the group with the same mismatch level $\Delta\mu$ constitutes the independent dispersion, we further rearrange each primary-group G_i into sub-groups σ_{ij} with $j = (1,2\cdots)$, so as the mismatch $\Delta\mu$ in each sub-group to have the same level. The entire dispersion is represented by the superposition of subgroups, i.e. $G_1 = \{\sigma_{11},\sigma_{12}\cdots\}$ (purple), $G_2 = \{\sigma_{21},\sigma_{22}\cdots\}$ (green), and $G_3 = \{\sigma_{31},\sigma_{32}\cdots\}$ (red), respectively. It is found that the growth rate spectrum of each sub-group forms a series of humps with largest growth rate in it. Meanwhile, it is of specific interest that the mode radial location r_p shifts outward with n as a whole as discussed above, while that inside each sub-group shifts inward with n against the FLR effect, but it is the direction to acquire larger free energy around $r_p \sim 52$ where modes $n_{G2} = 11/14$ in σ_{21} leads to the largest γ exist. This is also an evidence that the global dispersion is determined by the higher order global profile effect as the counterpart. Meanwhile, as seen in Fig. 4-8, the mismatch in the sub-group σ_{ij}, both $\Delta\mu$ and Δh, shows a weak dependence on n_{Gi}, exhibiting a smooth function. Especially, the mode $n_{G1} = 3$ in the sub-group σ_{31}, which is the first term of the arithmetic progression starting from the common difference $\Delta n = 3$, exhibits the smallest mode mismatch $\Delta\mu \sim -0.02$ (see Fig. 4-8 (a)). In addition, all modes in σ_{31} show almost the same helicity mismatch $\Delta h \sim -0.07$, indicating a single helicity nature localized at the same radial location $r_p \sim 47$ (see Fig. 4-8 (b) and Fig. 4-7 (c2)), which influences the nonlinear dynamics.

According to this grouping, the overlap of dispersion takes place between σ_{ij} and $\sigma_{ij\pm1}$ for the same toroidal mode number n in the same primary group n_{G_i} where only the mode with the largest growth rate is observed in the simulation while secondary and tertiary unstable mode are masked. Here, we study the secondary unstable mode by applying the dynamic mode decomposition (DMD) method [87] to the simulation data for $n = 10, 31, 18,$ and $33.$ as plotted in Fig. 4-7 (b2) and (b3) (marked by read square), we successfully find the secondary unstable mode for the growth rate for them, which belong to the subgroup σ_{12} for $n_{G_1} = 10$ and 31, σ_{31} for $n_{G_3} = 18$, and σ_{33} for $n_{G_3} = 33$, respectively, indicating that the sub-groups σ_{ij} are mutually independent as dispersion.

Here, we again confirm the relation between the growth rate γ and mismatch $\Delta\mu$ discussed in Fig. 4-2. The order of the subgroup σ_{ij} and corresponding $(\bar{n}_{G_i}, \Delta\mu)$, i.e. the toroidal mode number with the largest growth rate in the sub-group and the corresponding mismatch is as follows in descending order, i.e. σ_{21} with $(11, 0.23)$, σ_{12} with $(19, 0.43)$, $\sigma_{32}$with $(24, 0.63)$, σ_{22} with $(29;\ 0.79)$, σ_{13} with $(34, 1.03)$, ⋯. The results clearly indicate that the maximum growth and mismatch are tightly correlated, i.e. the smaller mismatch $\Delta\mu$, the larger growth rate γ is, supporting the hypothesis. It is noted that the largest growth rates in each sub-group constitutes the envelope of the growth rate spectrum for the consecutive toroidal mode number n, which is consistent with the overall tendency shown by green lines in Fig. 4-7 (b1).

Table 4-1 The regrouped modes in q_8-case

$\boldsymbol{G_1}$					G_2					G_3				
$\boldsymbol{\sigma}$	$\boldsymbol{\Delta\mu}$	$\boldsymbol{n}$	r_p	$\boldsymbol{M_\theta}$	$\boldsymbol{\sigma}$	$\boldsymbol{\Delta\mu}$	$\boldsymbol{n}$	r_p	$\boldsymbol{M_\theta}$	$\boldsymbol{\sigma}$	$\boldsymbol{\Delta\mu}$	$\boldsymbol{n}$	r_p	$\boldsymbol{M_\theta}$
σ_{11}	0.61	7	49.0	10	$\boldsymbol{\sigma_{21}}$	0.28	5	53.6	7	$\boldsymbol{\sigma_{31}}$	-0.02	3	47.5	4
σ_{11}	0.57	10	51.3	14	σ_{21}	0.25	8	54.3	11	σ_{31}	-0.05	6	46.8	8
σ_{12}	0.42	13	61.9	18	σ_{21}	0.23	11	52.8	15	σ_{31}	-0.07	9	46.8	12
σ_{12}	0.43	16	58.9	22	σ_{21}	0.20	14	52.1	19	σ_{31}	-0.09	12	46.8	16
σ_{12}	0.43	19	56.6	26	σ_{21}	0.18	17	50.6	23	$\boldsymbol{\sigma_{31}}$	-0.12	15	46.8	20
σ_{12}	0.42	22	55.1	30	σ_{21}	0.16	20	49.8	27	$\boldsymbol{\sigma_{32}}$	0.56	18	64.9	25
σ_{12}	0.41	25	53.6	34	σ_{21}	0.14	23	49.0	31	σ_{32}	0.58	21	62.7	29
σ_{12}	0.40	28	52.1	38	σ_{22}	0.78	26	63.4	36	σ_{32}	0.63	24	59.6	33
σ_{13}	0.96	31	64.2	43	σ_{22}	0.79	29	61.9	40	σ_{32}	0.62	27	58.1	37
σ_{13}	1.03	34	61.9	47	σ_{22}	0.84	32	59.6	44	σ_{32}	0.64	30	55.8	41
σ_{13}	1.09	37	59.6	51	σ_{22}	0.89	35	56.6	48	σ_{32}	0.66	33	53.6	45
					σ_{22}	0.94	38	53.6	52					

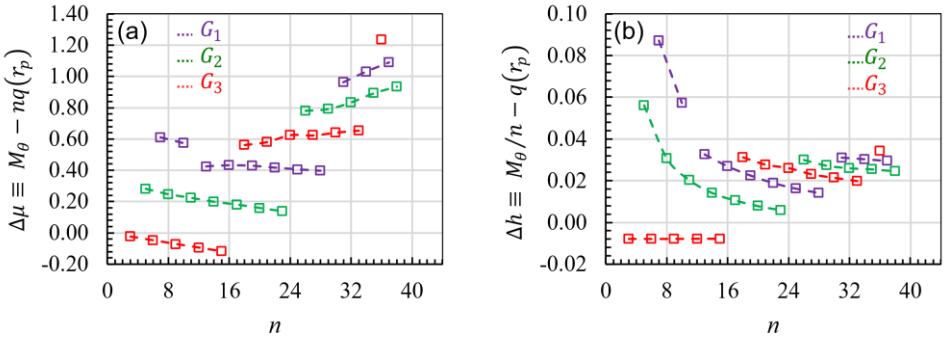

Fig. 4-8 Mismatch for (a) mode number $\Delta\mu$ and (b) helicity Δh on $\{n\}$ and also regrouped n_{G1-3} corresponding to Fig.2 in q_8-case with $\beta = 1.8\%$. The mode coupling of the modes $n = 11/14$ leading to $n = 3$ by subtraction (S) and $n = 25$ by addition (S) is shown as an example.

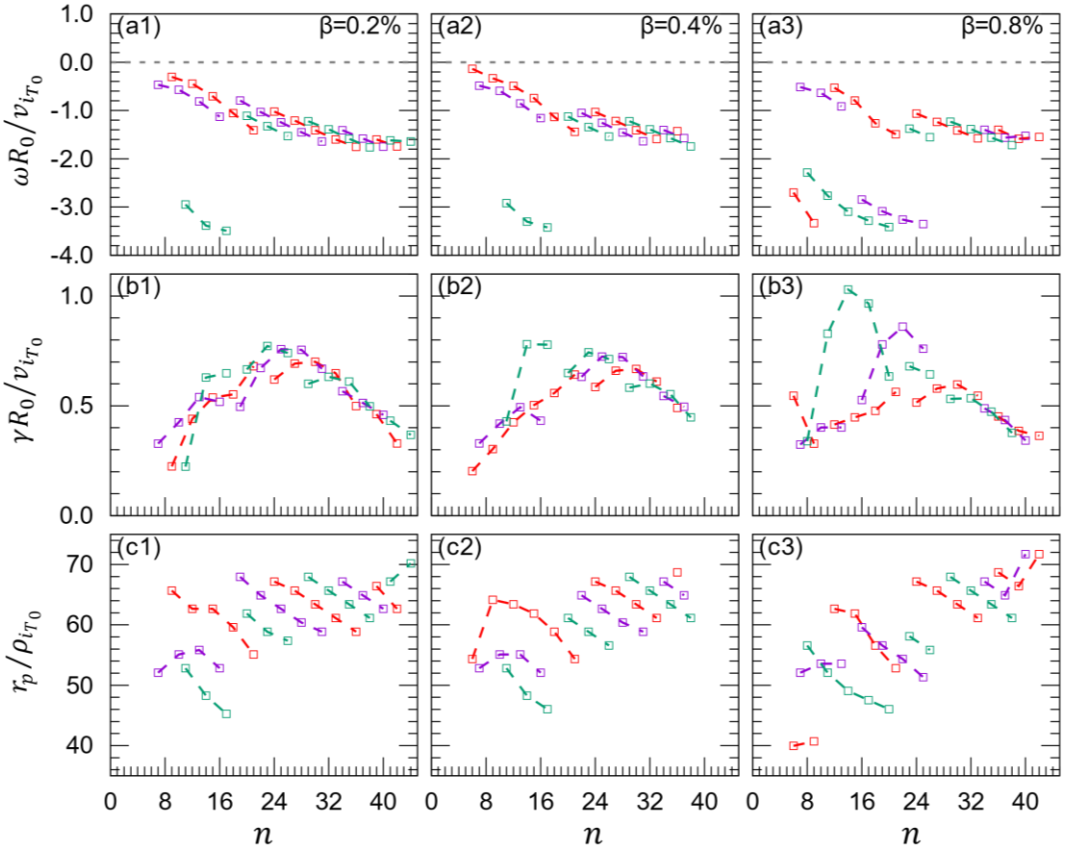

Fig. 4-9 "a" linear real frequency spectrum, "b" growth rate spectrum and "c" the radial position of the electrostatic potential of q_8-case for $\beta = 0.2\%, 0.4\%, 0.8\%, 1.8\%$ marked by number "1, 2, 3, 4"

The present complicated results in flat q-profile $q_8(r)$ do not only appear in high beta region $\beta = 1.8\%$ but also low beta region as shown in Fig. 4-9, where beta is set

as $\beta = 0.2\%\ 0.4\%\ 0.8\%$.. Unlike the q_2-case, even in large toroidal mode number region $n \geq 40$ there is no TEM being driven unstable whether beta is low or high. In general, it is found that, the amplitude of the oscillation in growth rate become large with β increasing. As for another characteristic of frequency, what we can clearly see is that the real frequency is divided into two intervals in ion diamagnetic direction. The first is $-2.0 < \omega R_0/v_{i_{T_0}} < 0$ and the second is $-2.0 < \omega R_0/v_{i_{T_0}} < 0$. More specifically, as the β increasing, more modes shift from first interval into second interval and the modes of low toroidal mode number are more likely to be driven to the second interval. For example, when $\beta = 0.2\%$, there are only three modes $n = 11, 14, 17$ in second interval as the Fig. 4-9 (a1), which is an arithmetic progression with a common difference of 3 due to $q_\mu = 0.34$. This is supporting our hypothesis. When $\beta = 1.8\%$, all the modes are shifted into the second interval shown in Fig. 4-7 (a1) or (a2). as the beta increases, the grouping method seems to become more feasible due to that the functions of real frequency and growth rate over toroidal mode number n become much smoother and the number of modes in some dominant sub-groups also increased. In addition, it is worth noting that the sub-group distributed in front of the spectrum, having relatively low toroidal mode number, become dominant. e.g., the group connected with a green dotted line in Fig. 4-9 (a4) (b4).

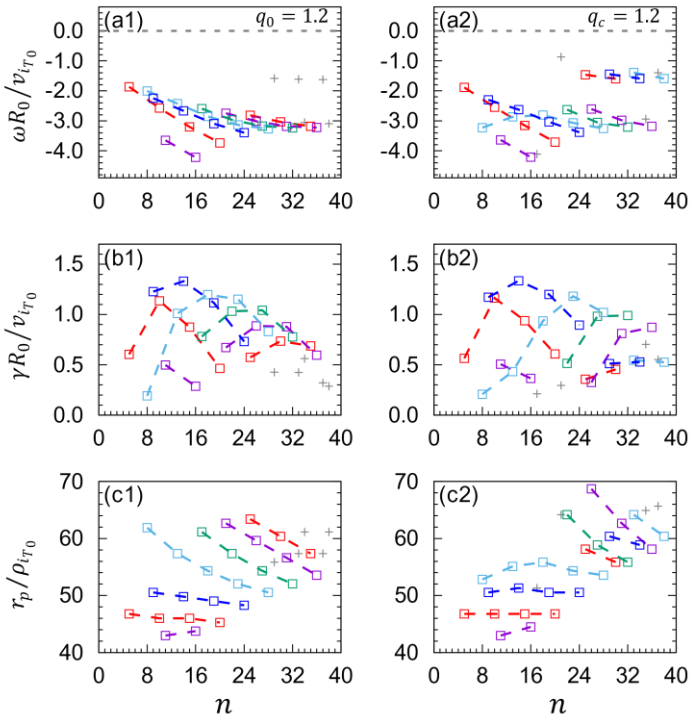

Fig. 4-10 “a” linear real frequency spectrum, “b” growth rate spectrum and “c” ratio of the radial position of the electrostatic potential of q_8-case for $q_\mu = 0.2$ marked by

number, '1' $q(r) = \text{const.} = 1.2$ marked by number '2'.

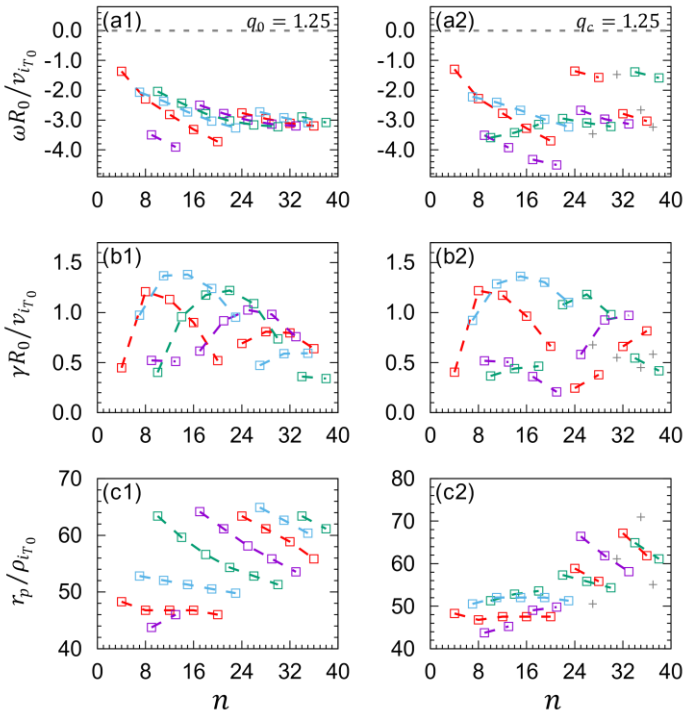

Fig. 4-11 "a" linear real frequency spectrum, "b" growth rate spectrum and "c" ratio of the radial position of the electrostatic potential of q_8-case for $q_\mu = 0.25$ marked by number, '1' $q(r) = \text{const.} = 1.25$ marked by number '2'.

In previous dicussion, we divide the safety factor $q(r)$ into three parts as $q(r) = 1 + q_\mu + \delta q(r)$. $\delta q(r)$ in core region is very small but it is still meaningful which will be discussed later. The non-integer residual constant q_μ determines the common difference of toroidal mode number n in groups, common difference $\Delta n \cong 1/q_\mu$. This conclusion is confirmed by other two cases defined through shifting the q_8-case. Comparing with basic q_8-case, the difference is only q_μ, one is $q_\mu = 0.2$ and another $q_\mu = 0.25$. The results are shown in figures marked by '1' of in Fig. 4-10 and in Fig. 4-11 respectively. As expected, the common difference $\Delta n = 5$ and $\Delta n = 4$ respectively.

Based on previous shifted flat q-profiles, we make the q-profiles flatter even a constant, $q(r) = 1.2$ corresponds results marked by number '2' in Fig. 4-10 and $q(r) = 1.25$ corresponds results marked by number '2' in Fig. 4-11. Comparing the monotonic q-profile cases $\delta q'(r) > 0$ with the corresponding constant q-profiles $\delta q(r) \equiv 0$, we found that the grouping phenomena in case $\delta q'(r) > 0$ is more well-

defined than that in case $\delta q(r) \equiv 0$. More specifically, the real frequency, growth rate and radial position of modes present smoother functions over toroidal mode number n and the numbers of modes in some dominant groups are more than that in cases $\delta q(r) \equiv 0$. in addition, in cases with constant q-profiles, the real frequency of a few modes of large toroidal mode number still lands in the first interval $-2.0 < \bar{\omega} < 0$ even $\beta = 1.8\%$. Combined with the difference of Δn produced by different q_μ, we consider that the KIM is sensitive to $q(r)$. Moreover, the Manickam concluded [27] that oscillations to appear it is necessary to have both low shear and a large enough pressure gradient in the regions of low shear or a moderate pressure gradient with high β. To sum up, the instability has two degrees of freedom for given β: one is pressure gradient ∇p and another is safety factor q. In the case of meeting a working pressure gradient ∇p, a very flat but monotonically increasing q-profile allows mode seeks a favorable magnetic surface within a certain range rather than a given fixed one by $q(r) = \text{const}$ as shown in Fig. 4-12. So that, the mode is driven better when $\delta q'(r) > 0$.

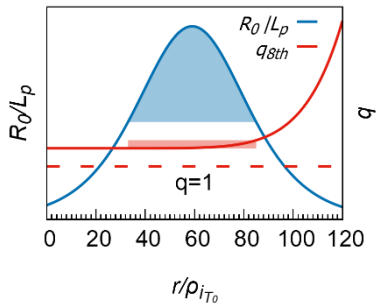

Fig. 4-12 the working R_0/L_p area filled with light blue and corresponding safety factor q area filled with light red

4.4 Nonlinear dynamics

Here, we present the results of non-linear simulation for the normal safety factor profile q_2 with $\beta = 2.4\%$ and that for the flat safety factor profile q_8 with $\beta = 1.8\%$ keeping consecutive toroidal mode number of $0 \leq n \leq 31$. Note that the q_2-case corresponds to that of KBMs with resonant characteristics satisfying $\Delta\mu = 0$ for all poloidal harmonics constituting ballooning type coupling as discussed in Fig. 4-2 (a1) (b1) and Fig. 4-3 (a1) (b1), while the q_8-case to that of KIMs with non-resonant characteristics, i.e. $\Delta\mu \neq 0$ with exhibiting oscillatory nature with respect to the toroidal mode number n, which can be apparently eliminated by rearranging the toroidal mode number n to groups and also sub-groups expressed by an arithmetic

progression with a common difference of Δn as discussed in Fig. 4-7.

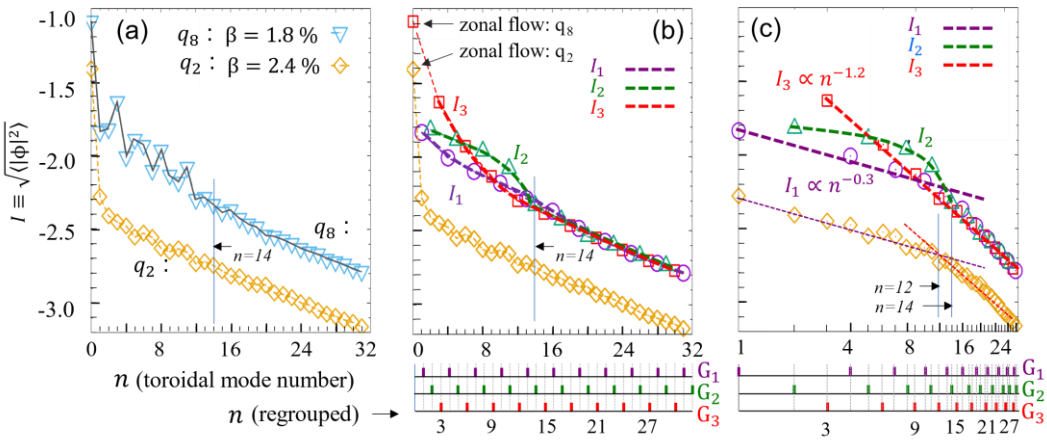

Fig. 4-13 (a) Turbulent spectrum of electrostatic potential I in q_2-case with $\beta = 2.4\%$ and q_8-case with $\beta = 1.8\%$ on the toroidal mode number $\{n\}$, (b) those divided to three primary groups for the q_8-case on regrouped n_{G1-3}, (c) those same as (b) on regrouped n_{G1-3} expressed by logarithmic plot. Dashed lines in (c) are fitting curves by $n^{-0.3}$ and $n^{-1.2}$.

The turbulent spectrum of electrostatic potential averaged over a time in the quasi-steady state as a function of the toroidal mode number n for both q_2 and the q_8-cases as shown in Fig. 4-13, where horizontal axis, i.e. n, is denoted by the linear scale in Fig. 4-13 (a) including $n = 0$ zonal components, while logarithmic scale in Fig. (c) excluding $n = 0$ but including whole n. In the q_2-case, contrary to the linear spectrum, which shows larger growth rate for $n = 18 - 22$, disappear as discussed in Ref. [23,40], the energy is found to be inverse cascaded and condensate to lower mode numbers with a large fraction of zonal flows. As also seen in Fig. 4-13 (c), the spectrum changes the character at n~11 exhibiting different power laws by $\langle|\phi|^2\rangle \propto n^{-0.3}$ for lower mode number, $n \leq 12$, while $\langle|\phi|^2\rangle \propto n^{-1.2}$ for higher ones, $n \geq 12$. It is also noted that the mode of $n = 1$~4 are linearly stable. A large fraction of zonal flows is considered to be responsible for the saturation of linear KBMs leading to a steady state turbulence incorporated with zonal pressure causing pressure relaxation, which are essentially same as those discussed in Ref. [40].

In the q_8-case, the general form of turbulent spectrum is similar to that in the q_2-case. Especially, the spectrum in the higher mode number region $n \geq 14$ follows a power law $\sqrt{\langle|\phi|^2\rangle} \propto n^{-1.2}$ similar to the q_2-case as seen in Fig. 4-13 (c). However, the energy level for q_8 is 2-3 times higher in the whole region of toroidal mode number. This is consistent with the observation that the growth rate for q_8 is about three time

larger than that for q_2. The difference is the oscillatory nature in lower mode number region of $n \leq 14$ as seen in Fig. 4-13 (a). Considering that the nature is correlated with those observed in the linear mode spectrum seen in Fig. 4-7, we also express the spectrum as the superposition of those corresponding to three primary groups (G_1, G_2, G_3) for the regrouped toroidal mode numbe (n_{G1}, n_{G2}, n_{G3}),and the result are shown in Fig. 4-13 (b) and (c).

As expected, the corrugated structure disappears while the spectrum is represented by three different smooth functions as seen in Fig. 4-13 (b) and (c). It is noted that no discontinuous jump is observed while all three spectra coincide for $n \geq 12$, indicating that the structure related to sub-group seen in the linear dispersion is disappeared in the nonlinear regime. Further analyses can be done based on Fig. 4-13 (c). That is, G_1 is fitted by almost same two power laws as the q_2 -case, i.e. $\sqrt{\langle|\phi|^2\rangle} \propto n^{-0.3}$ and $\sqrt{\langle|\phi|^2\rangle} \propto n^{-1.2}$, but with a knee at $n{\sim}10$. On the other hand, G_3, starting from $n = 3$, is represented by a sole power law $\sqrt{\langle|\phi|^2\rangle} \propto n^{-1.2}$ in entire region of n_{G_3}. G_2 is rather expressed by a Gaussian-type $\exp(-n^2)$ [88,89] for $n \leq 14$, above which it tends to $\sqrt{\langle|\phi|^2\rangle} \propto n^{-1.2}$, integrated with G_1 and G_3. Namely, three primary groups G_i tightly couple with each other in higher mode number region of $n \geq 14$, leading to the equipartition of turbulent anergy among them. Here, it is noted that linearly stable modes such as $n_{G_1} = 1$ and 4 in group G_1 and $n_{G_2} = 2$ in group G_2 show higher amplitudes in non-linear turbulent state together with the $n = 0$ zonal flow component resulting from the nonlinear interaction, which is categorized in group G_3.

In Fig. 4-14, we show the electrostatic potential in a poloidal cross section in the cases of (a) q_2 with $\beta = 2.4\%$ and (b) q_8 with $\beta = 1.8\%$, corresponding to those in Fig. 4-13 (a) and (c), where all toroidal numbers are contained besides the zonal flows, i.e., $\sum_{n\neq 0} \phi_n(r, \theta)$, at the end of the quasi-steady state. In the normal q-profile, i.e., q_2, a turbulent structure with mixed smaller scale eddies and those of relatively larger scale exhibiting weak ballooning characteristic can be seen. On the other hand, in the flat q-profile, i.e., q_8, a large-scale structure with $n = 3$, so that $M_p = nq{\sim}4$, where small scale eddies are embedded, can be seen, while showing almost homogeneous distribution in the poloidal cross section with no ballooning characteristics. This feature is consistent with the heat and particle fluxes observed in Fig. 4-16 (a2) and (b2).

In Fig. 4-15, same electrostatic potential in the q_8-case is shown as Fig. 4-14 (b) but divided into three primary groups G_j, i.e. $\phi_{G_j}(r,\theta) = \sum_{n=n_{G_j}} \phi_n(r,\theta)$. in (a), (b) and (c), respectively. The ϕ_{G_3} of group G_3 in Fig. 4-15 (c) is found to be roughly same as Fig. 4-14 (b) since $M_p = 4$ ($n_{G_3} = 3$) is the dominant mode as discussed in the above. The ϕ_{G_1} in Fig. 4-15 (a) shows a ballooning structure similar to q_2-case in Fig. 4-14 (a), which is consistent with the result that both spectra of q_2-case and G_1 are composed of two power laws. On the other hand, ϕ_{G_2} in Fig. 4-15 (b) shows a multi-scale nature where radially localized eddies with the mode number about $n\sim11\left(M_p\sim14\right)$, which roughly coincides with the largest growth rate in sub-group σ_{21} as seen in Fig. 4-7 (b2), appear inside around $r/\rho_{i_{T_0}}\sim50$ while radially extended large scale eddies outside.

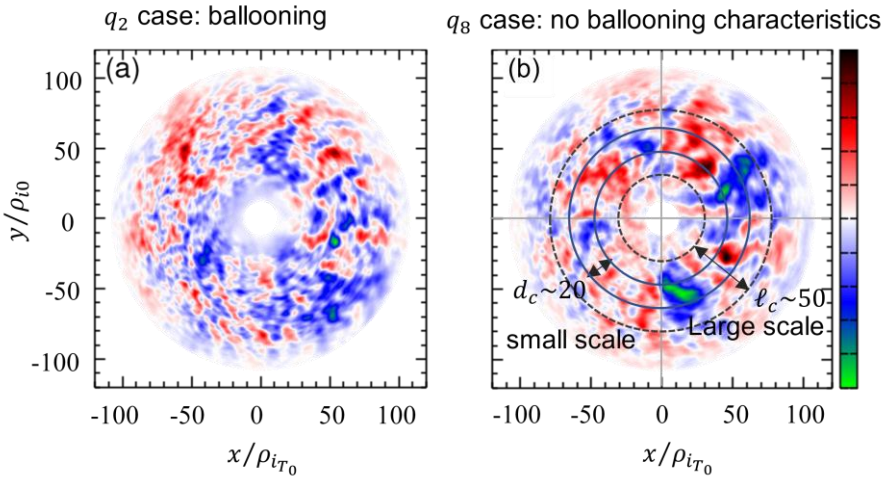

Fig. 4-14 Color maps of electrostatic potential of turbulence (a) in q_2-case $\beta = 2.4\%$ and (b) in q_8-case marked by '2'.

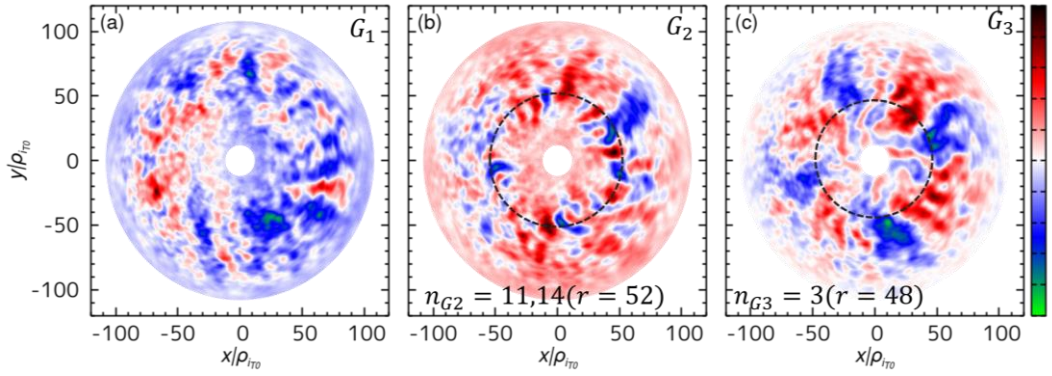

Fig. 4-15 Color maps of electrostatic potential of turbulence for (a) group G_1, (b) group G_2, (c) group G_3 (a) in q_8-case.

Based on the turbulent spectrum shown in Fig. 4-13, we investigate the spectrum

of heat flux $\langle Q_{\mathrm{n}} \rangle$ and particle flux $\langle \Gamma_{\mathrm{n}} \rangle$ with the toroidal mode number n for both q_2-case β=2.4% ((a1) (b1)) and q_8-case $\beta = 1.8\%$ ((a2) (b2)) in Fig. 4-16, respectively. In the normal safety factor profile, i.e. q_2, both $\langle Q_{\mathrm{n}} \rangle$ and $\langle \Gamma_{\mathrm{n}} \rangle$ exhibit relatively broader distributions with maximum values at $n = 10$. the heat flux is maintained by the mode around $n = 8{\sim}16$ which is lower than that with larger linear growth rate around $n = 16{\sim}24$, which shows weak inverse-cascade [23]. The heat flux $\langle Q_{\mathrm{n}} \rangle$ is found to be larger than the particle flux $\langle \Gamma_{\mathrm{n}} \rangle$ (about 5 times), which is also considered to result from weak density gradient as set in Fig. 4-1.

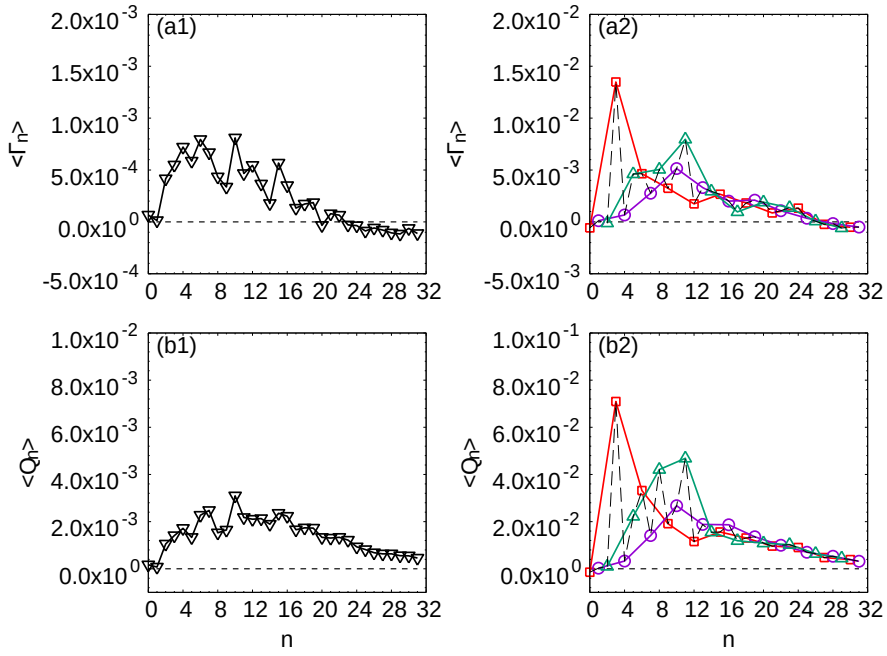

Fig. 4-16 The toroidal mode number spectrum of 'a' the ion particle flux Γ^i and 'b' the ion heating flux Q^i of q_2-case $\beta = 2.4\%$ marked by '1' and q_8-case $\beta = 1.8\%$ marked by '2'.

In the flat safety factor profile, i.e. q_8, both $\langle Q_{\mathrm{n}} \rangle$ and $\langle \Gamma_{\mathrm{n}} \rangle$ show corrugated structure in the region of lower toroidal mode number $n \leq 12$ as shown by dashed lines in Fig. 4-16 (a2) (b2), corresponding to those observed in the turbulent spectrum. Following the same procedure as that of turbulence, they can be expressed as the superposition of three primary groups (G_1, G_2, G_3), each of which exhibit contineous distribution and peaks at $n = 3$ in group G_3, $n = 11$ in group G_2, and $n = 10$ in group G_1, respectively. Here, the heat flux $\langle Q_{\mathrm{n}} \rangle$ is found to be also larger than the particle flux $\langle \Gamma_{\mathrm{n}} \rangle$ (about 5 times) as the same reason in the q_2-case. It is found that an order of magnitude larger heat and particle flux than those in the q_2-case is induced by the

components of low toroidal mode number around $n_{G_3} = 3$, which exhibits large scale structures around $M_p = 4$, followed by $n_{G_2} = 8$ and 11, while the contribution from G_1 is small. It is noted that all primary groups G_i are found to show the equipartition for $n \geq 14$, reflecting the turbulent spectral discussed in Fig. 4-13 (c).

Here, we discuss the origin of the characteristics of the turbulent spectrum in Fig. 4-13 and resultant heat flux in Fig. 4-16 based on the nonlinear interaction among rearranged primary groups G_i in the following. It is considered in Fig. 4-7 (b2) that the sub-group σ_{21} in the primary group G_2 includes the modes with the largest growth rate among all sub-groups, i.e. $n_{G_2} = 11$ and 14, and dominantly supplies turbulent energy to the system, while G_1 and G_3, which include those with smaller growth rates in sub-group σ_{12} ($n_{G_1} \sim 9$) and σ_{31} ($n_{G_3} \sim 19$), receive turbulent energy from G_2. It is interesting to note that any mode coupling resulting from the subtraction inside group G_1 and G_2 leads to modes given by $n_{G_3} = \Delta n \cdot j = 3, 6, 9 \ldots$ ($j = 1,2,3 \ldots$) which belong to group G_3. Among them, the mode $n = 3$ is fundamental since the subtraction of any adjacent two modes in group G_1 and G_3, which are considered to provide larger contribution, connects to $n = 3$. On the other hand, the mode coupling due to the addition inside G_1 leads to the mode in G_2 and vice versa, i.e. that inside G_2 leads to the mode in G_1, indicating that G_1 and G_2 exchange energy while no energy transfer to group G_3. Meanwhile, any couplings inside G_3, either subtraction or addition, leads to the own group G_3. Namely, in the present non-resonant system characterized by three primary groups (G_1, G_2, G_3), the energy flow by $G_1 \rightarrow G_3$ and $G_2 \rightarrow G_3$ exists while the reverse process such as $G_3 \rightarrow G_1$ and $G_3 \rightarrow G_1$ is forbidden. It is then considered that the turbulent energy tends to condensate to the primary group G_3, especially to the mode $n_{G_3} = 3$, which is consistent to the results seen in Fig. 4-13 and Fig. 4-15.

As we discussed, the primary group G_3 leads to the power law spectrum with sole power law index as $\sqrt{\langle |\phi|^2 \rangle} \propto n^{-1.2}$ in the entire region of toroidal mode number with no bending point as that of G_1 and G_2. This is also consistent with the above discussion, i.e., the turbulent energy is supplied predominantly to the mode $n_{G_3} = 3$ in G_3 from G_2 along with G_1 through nonlinear mode coupling. Then, the energy is forward-cascaded to higher mode numbers inside G_3 assuming that the contribution due to the inverse cascade from linearly unstable mode around $n_{G_3} = 9$, which is smaller compared with

that in group G_2, to lower mode number is small. The non-power law feature of the spectrum in group G_2 is considered to be influenced by the presence of the linear free energy source.

The global dispersion as the superposition of independent sub-groups σ_{ij} distribute at different radial location with typical radial extent as seen in Fig. 4-7 (c2). Since they directly interact through the spatila dimension, the radial extent of the dispersion is considered to be a measure of the correlation length of resulting tubulence ℓ_c instead of simple radial mode width Δr. In the present q_8-case, $\ell_c = 30\sim40$ is estimated.

The safety factor profile $q(r) = 1 + 0.25 + \delta q(r)$ in nonlinear simulation

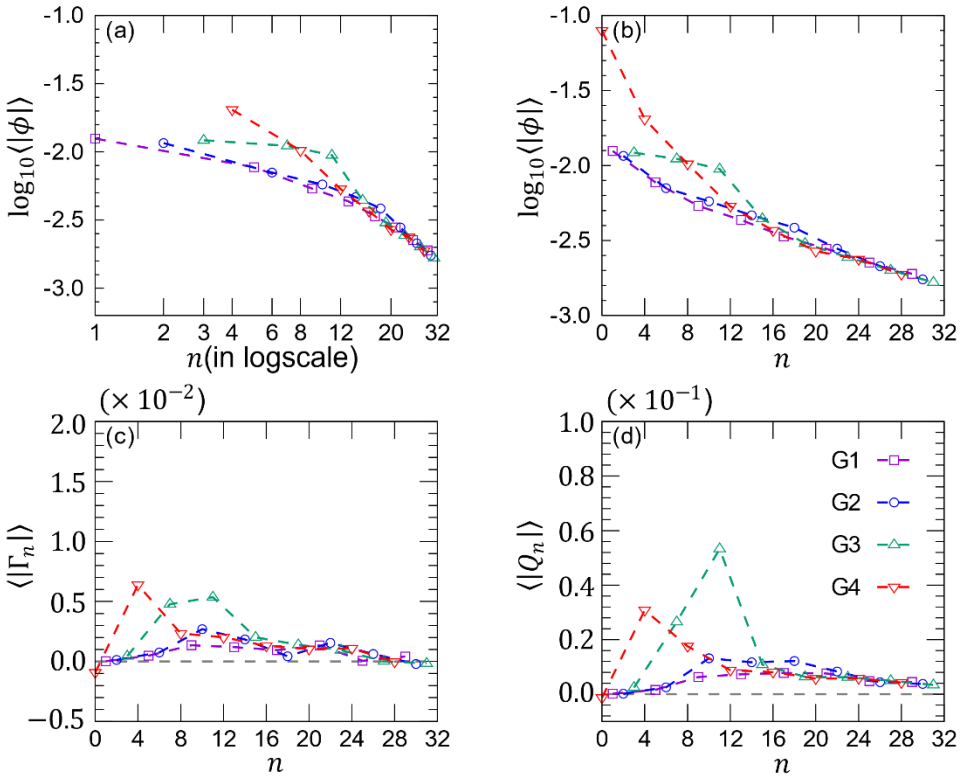

Fig. 4-17 The regrouped turbulent spectrum of electrostatic potential (a), (b) where n in (a) is expressed by logarithmic plot. The regrouped particle and heating flux spectra of q_8-case with $q_\mu = 0.25$ are shown in (c) and (d) respectively.

Based on the previous q_8-case, we shift down the q-profile to that $q_\mu = 0.25$ as we did in linear simulation whose results are shown in Fig. 4-10. As expected, the corrugated structure disappears while the spectrum is represented by four different smooth functions, as well as the particle and heating fluxes in Fig. 4-17. Due to the

selective and/or directional energy flow among primary groups, the turbulence of group G_4 ,starting from $n = \Delta n = 4$, is dominant and represented by a sole power law $\sqrt{\langle|\phi|^2\rangle} \propto n^{-1.2}$ in entire region of n_{G_4} as shown in Fig. 4-17 (a). it is similar to the group G_3 in previous basic q_8-case which $q_\mu = 0.34$. The group G_1 is fitted by two power laws those are $\sqrt{\langle|\phi|^2\rangle} \propto n^{-0.39}$ for $1 \leq n \leq 9$ and $\sqrt{\langle|\phi|^2\rangle} \propto n^{-0.98}$ for $13 \leq n \leq 29$. The group G_2 is also fitted by two power laws those are $\sqrt{\langle|\phi|^2\rangle} \propto n^{-0.44}$ for $2 \leq n \leq 16$ and $\sqrt{\langle|\phi|^2\rangle} \propto n^{-1.62}$ for $18 \leq n \leq 30$. On the other hand, the group G_3, which the most linear unstable modes $n = 11, 15$ are belong to, is rather expressed by a Gaussian-type $\exp(-n^2)$ for $n \leq 15$. In general, the turbulence spectrum of q_8-case with $q_\mu = 0.25$ presents same characteristics as that in previous basic q_8-case with $q_\mu = 0.34$.

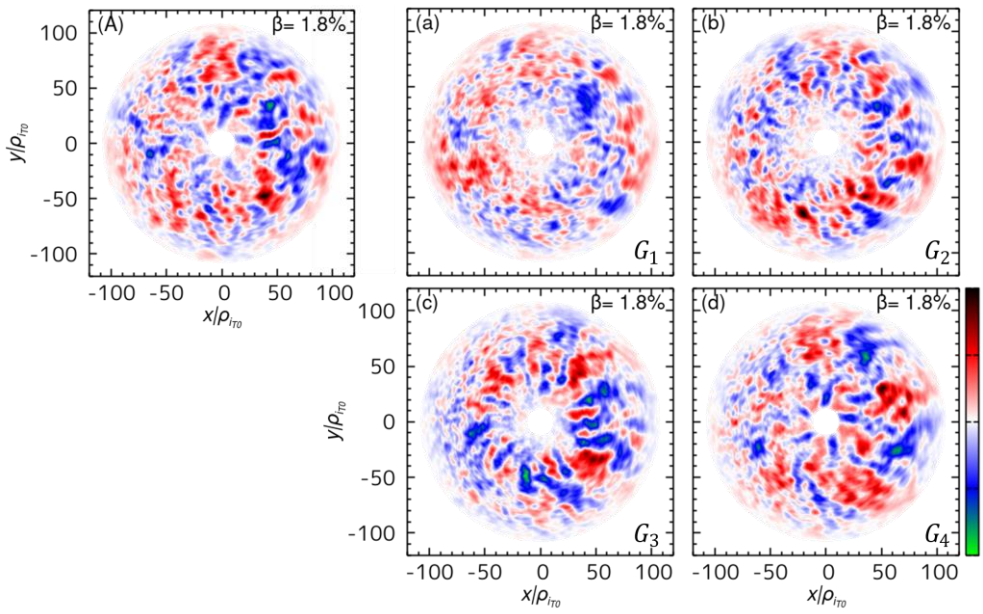

Fig. 4-18 Color maps of electrostatic potential of turbulence for (A) total, (a) group G_1, (b) group G_2, (c) group G_3 (a) in q_8-case with $q_\mu = 0.25$.

On the other hand, the figures (c) and (d) in Fig. 4-17 show that the particle and heating fluxes in each primary group also can be connected with relatively smooth function but the level of those fluxes is lower than those previous basic q_8-case with $q_\mu = 0.34$ (in Fig. 4-16). The large difference in particle and heating fluxes spectra from previous basic q_8-case is that the group G_4 is no longer main contribution source, instead, the group G_3 dominates the particle and heating fluxes. The highest heat flux

is driven by the mode $n = 11$ which is most unstable mode in linear phase as shown in Fig. 4-10 (b4). This difference can be explained by investigating the electrostatic potential structure on poloidal cross-section shown in Fig. 4-18. In Fig. 4-18, the total electrostatic potential is shown in (A) and the each primary groups' $\phi_{G_j}(r,\theta) = \sum_{n=n_{G_j}} \phi_n(r,\theta)$, is in (a) (b) (c) (d) in turn. The ϕ_{G_1} in Fig. 4-18 (a) consists of some small-scale structures and shows a weak ballooning structure. From G_1 to G_4, the structure of electrostatic potential tends to become large-scale and non-ballooning. Especially, the ϕ_{G_4} of G_4 in Fig. 4-18 (d) is found to have roughly largest scale structure whose poloidal mode number $M_p = 5$ ($n_{G_4} = 4$) is the dominant mode as discussed in the above. But the radial structure was interrupted around $r/\rho_{i_{T_0}} \sim 50$, especially at bad curvature side. On the other hand, the ϕ_{G_3} of G_3 in Fig. 4-18 (c) shows a clear structure with the mode number about $n \sim 11 (M_p \sim 14)$, which is consistent with the largest growth rate in as seen in Fig. 4-10 (b4). Another important feature is that the ϕ_{G_3} of G_3 exhibits much more extended structures in radial direction which could drive large transport.

4.5 Conclusion

Linear and nonlinear evolution of micro-instability and associated turbulent transport are studied by means of the electromagnetic version of gyro-kinetic based global toroidal system GKNET using δf method for plasmas with a nearly flat safety factor profile around the half minor radius as $q(r = a/2) \sim q_0 + q_\mu$, where q_0 and q_μ are integer and non-integer residual constant parts, respectively, where the magnetic shear is $\hat{s} \sim 0$. In such plasmas, non-resonant modes localized around the radial region of the maximum pressure gradient become linearly unstable in the wider region of β-value, which is similar to those found in a reversed safety factor profile referred to as infernal modes (IMs). The associated linear dispersion and non-linear turbulent spectrum show hardly deterministic complex corrugated structures for the consecutive toroidal mode number n resulting from a quasi-random distribution of the resonance mismatch $\Delta\mu \equiv M_\theta - nq_c$ which prescribes the free energy.

Such a structure is disappeared by rearranging the dispersion to primary groups G_i and further sub-group σ_{ij} for discrete Δn sets of the toroidal mode number n_{G_i} given by the arithmetic progression with Δn as the common difference which is determined

by the non-integer residue of the constant safety $\Delta n \sim 1/\delta q_\mu$. Here, the sub-group σ_{ij}, by which the linear dispersion is reordered by the superposition, is obtained by further regrouping each primary-group G_i so as the modes within it to have the same level of free energy.

The regrouped discrete dispersion leads to a new class of hierarchized turbulence. That is, all nonlinear coupling pairs due to the subtraction of any modes inside same primary group G_i connect to the modes of $n_{G_{\Delta n}}$ in specific primary group $G_{i=\Delta n}$ indicating that the energy flow among primary groups is selective and/or directional. It is specifically noted that all adjacent two modes in each primary group, which is considered to provide a large contribution, connect to the lowest mode $n_{G_{\Delta n}} = \Delta n$, to which the energy tends to be condensated. Each priANISmary group then forms a quasi-independent spectrum regurated by differnet enegy enegy flows, both input and output, so that the entire spectrum is constituted by their superposition. In the present basic q_8-case with $q_\mu = 0.34$, the large amount of energy is condensated to $n_{G_3} = 3$, which exhibits a quasi-coherent large scale homogenized structure mixed with those with smaller scales. The concept of regrouped discrete dispersion and selective turbulence is considered to provide the basis to understand the turbulent transport in advance operation leading to higher confinement state.

The particle and heat fluxes are induced as a superposition of continuous turbulence spectrum corresponding to the groups, while the low mode number of $n = \Delta n$, which is weakly unstable in linear regime provides larger fluxes, exhibiting an oscillatory nature with respect to toroidal mode number. In contrast to the normal safety factor profile such as the q_2-case, the turbulent exhibits quasi-coherent homogeneous structure predominantly regulated by the poloidal mode number given by $m = \Delta n(q_0 + q_\mu)$ incorporated with small scale turbulent eddies.

The transport in plasmas with flat safety factor profile where the turbulence is induced by a non-resonant free energy source regulated by the mismatch form the resonance condition, i.e. $\Delta\mu \equiv M_\theta - nq_0$ is higher than that with normal safety factor profile in spite of the large fraction of zonal flows in KIMs. In the present simulation, we studied the turbulent transport in a global toroidal geometry where the effect of global profile variation is taken into account self-consistently while used a δf-scheme where a quasi-static equilibrium with no neo-classically determined radial electron field.

Studies of transport barrier formation which are found to be emerged in plasmas with flat and/or reversed safety factor profile, where self-consistent evolution of background profile incorporated with quasi-static radial electric coupled with zonal flows. These are our next target which is discussed in subsequent papers.

5 Summary and discussion

5.1 Summary

This work started with a question for an abundant and environmentally friendly source of energy at an affordable cost. Tokamak, a toroidal magnetic confinement system for fusion plasma, is considered to be a main away to achieve controlled nuclear fusion. For overcoming the electrostatic repulsion, the charged particles must be heated to have very high temperature by using NBI and/or ECRH. The gradients of density and temperature will provide the free energy to drive various types of drift modes categorized as micro-instability like ITG mode and TEM which are the candidates causing anomalous transport and then degrading the confinement performance. Additionally, it is confirmed that these micro-instabilities are influenced by the auxiliary heating through the modification of distribution function in velocity space. On the other hand, as a magnetic confinement system, the magnetic field in tokamak defined by the safety factor and magnetic shear plays a central role since they regulate the mode structure predominantly. In standard tokamak operation, a normal safety factor profile increasing radially induces a ballooning type mode, such as TEM and ITG mode, by the toroidal coupling between adjacent poloidal harmonics. The eigenvalue is determined by the local dispersion in the lowest order and the spatial structure in the first order determined by the global profile variation.

By separating the temperature into parallel and perpendicular parts in GKNET which are expected to describe briefly the modification of distribution function in velocity space induced by NBI and ECRH, in the plasma with a normal safety factor profile we found that the ITG mode is suppressed obviously by higher ion perpendicular temperature but independent on electron perpendicular temperature, and TEM is enhanced significantly by being increased electron perpendicular temperature but independent on ion perpendicular temperature. It's interesting that a new type of density gradient driven drift mode exhibiting low real frequency shows a hybrid feature mixing ITG mode and TEM. This low frequency instability could be enhanced by higher ion perpendicular temperature and suppressed by higher ion perpendicular temperature which is consistent with the experiment results on HL-2A. The low frequency instability was suppressed when only NBI is implemented, thereby, a ITB is built. But

the following more powerful ECRH enhances the instability and then leads the collapse of ITB even the NBI was being kept.

In advanced operation for accessing high performance plasmas with steep pressure gradient, plasmas with nearly flat or reversed safety factor profile where the magnetic shear vanishes is established. Due to the lack of the resonance, the instability becomes to be an infernal type of non-resonant mode rather than the ballooning type mode. The ballooning theory is invalid since no counterpart to determine the eigenvalue in the lowest order exists, and higher order non-local effect associated with the global profile variation plays an essential role. The associated linear dispersion and non-linear turbulent spectrum show hardly deterministic complex corrugated structures for the consecutive toroidal mode number n. Here, based on the resonance mismatch $\Delta\mu \equiv M_\theta - nq$ prescribing the free energy, we present a law prescribing the system by regrouping the toroidal mode number and corresponding global dispersion using the arithmetic progression by properly choosing the common difference which is determined by the non-integer residue of the constant safety $\Delta n \sim 1/\delta q_\mu$. The regrouped dispersion leads to a new class of turbulence regulated by quasi-independent hierarchized spectra due to the selective and/or directional enegy flows. The concept explored here provides the fundamental basis to understand the turbulent transport in advance operation where non-local and non-diffusive play an important role.

5.2 Future work

In the present simulations, the parameter $\Lambda = T_\perp/T_\parallel$ is introduced into background equilibrium distribution function to stand for the effect of auxiliary heating such as NBI ECRH ICRH which means that all the background plasma is heated in same level. However, in experiments, the power of auxiliary heating is deposited in narrow region in radial direction and the deposition location is crucial for foot position of ITB usually. Therefore, the flux-driven simulation with a certain power deposition profile using the full-f version of GKNET should be considered to make the realistic simulation. On the other hand, the low frequency instability is found to exhibit a hybrid feature mixing ITG mode and TEM but limited in linear analysis. The corresponding nonlinear dynamics will be investigated to understand the role of the mode on the transport in nest step.

When safety factor profile become extremely flat, the dispersion can be

rearranged into Δn groups whose toroidal mode is given by the arithmetic progression with common difference $\Delta n = 1/q_\mu$. In all cases to date, the constant part of safety factor, $1 < q_0 + q_\mu < 2$. For exploring the mechanisms of grouping behind, it is necessary to make the $q_0 + q_\mu < 1$ or $q_0 + q_\mu > 2$ in future simulations.

In all simulations of this thesis, we used a δf-scheme where a quasi-static equilibrium with no neo-classically determined radial electric field. Nevertheless, transport barrier formation is found to be emerged in plasmas with flat and/or reversed safety factor profile, where self-consistent evolution of background profile incorporated with quasi-static radial electric field coupled with zonal flows. These are our next target which will be discussed in subsequent works.

6 Bibliograph

[1] *UNITED NATIONS DEVELOPMENT PROGRAMME*, Http://Hdr.Undp.Org/ (n.d.).

[2] B. P. E. Outlook, *2019 Edition*, London, United Kingdom2019 (2019).

[3] C. Iliadis, *Nuclear Physics of Stars* (John Wiley & Sons, 2015).

[4] W. Booth, *Fusion's $372-Million Mothball*, Sci. (Washington, DC) **238**, (1987).

[5] D. A. Gates, D. Anderson, S. Anderson, M. Zarnstorff, D. A. Spong, H. Weitzner, G. H. Neilson, D. Ruzic, D. Andruczyk, and J. H. Harris, *Stellarator Research Opportunities: A Report of the National Stellarator Coordinating Committee*, J. Fusion Energy **37**, 51 (2018).

[6] T. H. Stix, *Heating of Toroidal Plasmas by Neutral Injection*, Plasma Phys. **14**, 367 (1972).

[7] R. F. Post, *High-Temperature Plasma Research and Controlled Fusion*, Annu. Rev. Nucl. Sci. **9**, 367 (1959).

[8] L. G. Kuo, E. G. Murphy, M. Petravić, and D. R. Sweetman, *Experimental and Theoretical Studies of Instabilities in a High-Energy Neutral Injection Mirror Machine*, Phys. Fluids **7**, 988 (1964).

[9] W. Bernstein, V. V Chechkin, L. G. Kuo, E. G. Murphy, M. Petravic, A. C. Riviere, and D. R. Sweetman, *Plasma Produced by Neutral Injection into a Magnetic Mirror/Well Geometry*, in *Plasma Physics and Controlled Nuclear Fusion Research. Vol. II. Proceedings of a Conference on Plasma Physics and Controlled Physics Research Nuclear Fusion Research* (1966).

[10] T. H. Stix, *The Theory of Plasma Waves McGraw-Hill Book Co*, Inc., New York 169 (1962).

[11] Thomas H. Stix, *Waves in Plasmas* (New York, 1992).

[12] W. Horton, *Drift Waves and Transport*, Rev. Mod. Phys. **71**, 735 (1999).

[13] X. Garbet, *Turbulence in Fusion Plasmas: Key Issues and Impact on Transport*

Modelling, Plasma Phys. Control. Fusion **43**, A251 (2001).

[14] L. Villard, S. J. Allfrey, A. Bottino, M. Brunetti, G. L. Falchetto, V. Grandgirard, R. Hatzky, J. Nührenberg, A. G. Peeters, and O. Sauter, *Full Radius Linear and Nonlinear Gyrokinetic Simulations for Tokamaks and Stellarators: Zonal Flows, Applied E× B Flows, Trapped Electrons and Finite Beta*, Nucl. Fusion **44**, 172 (2003).

[15] T. Dannert and F. Jenko, *Gyrokinetic Simulation of Collisionless Trapped-Electron Mode Turbulence*, Phys. Plasmas **12**, 1 (2005).

[16] X. Garbet, Y. Idomura, L. Villard, and T. H. Watanabe, *Gyrokinetic Simulations of Turbulent Transport*, Nucl. Fusion **50**, 43002 (2010).

[17] a. M. Dimits, T. J. Williams, J. a. Byers, and B. I. Cohen, *Scalings of Ion-Temperature-Gradient-Driven Anomalous Transport in Tokamaks*, Phys. Rev. Lett. **77**, 71 (1996).

[18] M. Kikuchi, *Prospects of a Stationary Tokamak Reactor*, Plasma Phys. Control. Fusion **35**, B39 (1993).

[19] R. J. Goldston, S. H. Batha, R. H. Bulmer, D. N. Hill, A. W. Hyatt, S. C. Jardin, F. M. Levinton, S. M. Kaye, C. E. Kessel, E. A. Lazarus, J. Manickam, G. H. Neilson, W. M. Nevins, L. J. Perkins, G. Rewoldt, K. I. Thomassen, and M. C. Zarnstorff, *Advanced Tokamak Physics-Status and Prospects*, Plasma Phys. Control. Fusion **36**, B213 (1994).

[20] A. G. Peeters, *The Bootstrap Current and Its Consequences*, Plasma Phys. Control. Fusion **42**, B231 (2000).

[21] F. M. Levinton, M. C. Zarnstorff, S. H. Batha, M. Bell, R. E. Bell, R. V Budny, C. Bush, Z. Chang, E. Fredrickson, and A. Janos, *Improved Confinement with Reversed Magnetic Shear in TFTR*, Phys. Rev. Lett. **75**, 4417 (1995).

[22] Y. Kishimoto, J. Y. Kim, W. Horton, T. Tajima, M. J. LeBrun, and H. Shirai, *Toroidal Mode Structure in Weak and Reversed Magnetic Shear Plasmas and Its Role in the Internal Transport Barrier*, Plasma Phys. Control. Fusion **41**, A663 (1999).

[23] Y. Ishida, A. Ishizawa, K. Imadera, Y. Kishimoto, and Y. Nakamura, *Global*

Gyrokinetic Nonlinear Simulations of Kinetic Infernal Modes in Reversed Shear Tokamaks, Phys. Plasmas **27**, (2020).

[24] D. Brunetti, J. P. Graves, F. D. Halpern, J. F. Luciani, H. Lütjens, and W. A. Cooper, *Extended MHD Simulations of Infernal Mode Dynamics and Coupling to Tearing Modes*, Plasma Phys. Control. Fusion **57**, (2015).

[25] L. A. Charlton, R. J. Hastie, and T. C. Hender, *Resistive "Infernal" Modes*, Phys. Fluids B **1**, 798 (1989).

[26] R. J. Hastie and J. B. Taylor, *Validity of Ballooning Representation and Mode Number Dependence of Stability*, Nucl. Fusion **21**, 187 (1981).

[27] J. Manickam, N. Pomphrey, and A. M. M. Todd, *Ideal Mhd Stability Properties of Pressure Driven Modes in Low Shear Tokamaks*, Nucl. Fusion **27**, 1461 (1987).

[28] R. Ganesh and J. Vaclavik, *Global Gyrokinetic Stability of Pressure-Gradient-Driven Electromagnetic Modes in Tokamaks with Regions of Low Shear*, Phys. Rev. Lett. **94**, 1 (2005).

[29] T. Ozeki, M. Azumi, Y. Kamada, S. Ishida, Y. Neyatani, and S. Tokuda, *Ideal MHD Stability of High Bp Plasmas and Bp Collapse in JT-60U*, Nucl. Fusion **35**, 861 (1995).

[30] T. Ozeki, M. Azumi, S. Tokuda, and S. Ishida, *Effects of a Hollow Current Profile on the Ideal MHD Stability of High Beta p Plasmas in a Tokamak*, Nucl. Fusion **33**, 1025 (1993).

[31] R. L. Dewar, J. Manickam, R. C. Grimm, and M. S. Chance, *N-Dependence of Ballooning Instabilities*, Nucl. Fusion **21**, 493 (1981).

[32] D. L. Yu, Y. L. Wei, L. Liu, J. Q. Dong, K. Ida, K. Itoh, A. P. Sun, J. Y. Cao, Z. B. Shi, Z. X. Wang, Y. Xiao, B. S. Yuan, H. R. Du, X. X. He, W. J. Chen, Q. Ma, S.-I. Itoh, K. J. Zhao, Y. Zhou, J. Wang, X. Q. Ji, W. L. Zhong, Y. G. Li, J. M. Gao, W. Deng, Y. Liu, Y. Xu, L. W. Yan, Q. W. Yang, X. T. Ding, X. R. Duan, and Y. Liu, *Ion Internal Transport Barrier in Neutral Beam Heated Plasmas on HL-2A*, Nucl. Fusion **56**, 056003 (2016).

[33] A. J. Brizard, *Nonlinear Gyrokinetic Tokamak Physics*.

[34] D. H. E. D. Dubin, J. Krommes, and C. Oberman, *Nonlinear Gyrokinetic Equations*, Phys. Fluids **26**, 3524 (1983).

[35] T. S. Hahm, *Nonlinear Gyrokinetic Equations for Tokamak Microturbulence*, Phys. Fluids **31**, 2670 (1988).

[36] J. R. Cary, *Lie Transform Perturbation Theory for Hamiltonian Systems*, Phys. Rep. **79**, 129 (1981).

[37] J. R. Cary and R. G. Littlejohn, *Noncanonical Hamiltonian Mechanics and Its Application to Magnetic Field Line Flow*, Ann. Phys. (N. Y). **151**, 1 (1983).

[38] G. Szepsi, *Derivation of the Fully Electro-Magnetic, Non-Linear, Gyrokinetic Vlasov–Maxwell Equations in a Rotating Frame of Reference for GKW with Lie Transform Perturbation Method*.

[39] A. J. Brizard and T. S. Hahm, *Foundations of Nonlinear Gyrokinetic Theory*, Rev. Mod. Phys. **79**, 421 (2007).

[40] A. Ishizawa, K. Imadera, Y. Nakamura, and Y. Kishimoto, *Global Gyrokinetic Simulation of Turbulence Driven by Kinetic Ballooning Mode*, Phys. Plasmas **26**, (2019).

[41] C.-Z. Cheng and G. Knorr, *The Integration of the Vlasov Equation in Configuration Space*, J. Comput. Phys. **22**, 330 (1976).

[42] H. Yoshida, *Construction of Higher Order Symplectic Integrators*, Phys. Lett. A **150**, 262 (1990).

[43] S. Jolliet, A. Bottino, P. Angelino, R. Hatzky, T.-M. Tran, B. F. Mcmillan, O. Sauter, K. Appert, Y. Idomura, and L. Villard, *A Global Collisionless PIC Code in Magnetic Coordinates*, Comput. Phys. Commun. **177**, 409 (2007).

[44] Y. Morinishi, T. S. Lund, O. V Vasilyev, and P. Moin, *Fully Conservative Higher Order Finite Difference Schemes for Incompressible Flow*, J. Comput. Phys. **143**, 90 (1998).

[45] C. A. De Moura and C. S. Kubrusly, *The Courant–Friedrichs–Lewy (Cfl) Condition*, AMC **10**, (2013).

[46] K. Imadera, J. Q. Li, and Y. Kishimoto, *ITB Formation in Gyrokinetic Flux-*

Driven ITG Turbulence, in *IAEA-FEC* (Kyoto, 2016), p. TH/P3-3.

[47] S. Ide, H. Takenaga, A. Isayama, Y. Sakamoto, M. Yoshida, and C. Gormezano, *Studies on Impact of Electron Cyclotron Wave Injection on the Internal Transport Barriers in JT-60U Weak Shear Plasmas*, Nucl. Fusion **47**, 1499 (2007).

[48] H. Takenaga, N. Oyama, H. Urano, Y. Sakamoto, N. Asakura, K. Kamiya, Y. Miyo, T. Nishiyama, T. Sasajima, K. Masaki, a. Kaminaga, H. Ichige, J. Bucalossi, V. Marty, S. Ide, Y. Koide, and Y. Kamada, *The Characteristics of the Internal Transport Barrier under Reactor Relevant Conditions in JT-60U Weak Shear Plasmas*, Nucl. Fusion **49**, 075012 (2009).

[49] M. Yoshida, M. Honda, E. Narita, N. Hayashi, H. Urano, M. Nakata, N. Miyato, H. Takenaga, S. Ide, and Y. Kamada, *Effects of Toroidal Rotation Shear and Magnetic Shear on Thermal and Particle Transport in Plasmas with Electron Cyclotron Heating on JT-60U*, Nucl. Fusion **55**, 73014 (2015).

[50] C. M. Greenfield, C. L. Rettig, G. M. Staebler, B. W. Stallard, M. E. Austin, K. H. Burrell, J. C. DeBoo, J. S. deGrassie, E. J. Doyle, and P. Gohil, *Behaviour of Electron and Ion Transport in Discharges with an Internal Transport Barrier in the DIII-D Tokamak*, Nucl. Fusion **39**, 1723 (1999).

[51] L. Schmitz, C. Holland, T. L. Rhodes, G. Wang, L. Zeng, A. E. White, J. C. Hillesheim, W. A. Peebles, S. P. Smith, and R. Prater, *Reduced Electron Thermal Transport in Low Collisionality H-Mode Plasmas in DIII-D and the Importance of TEM/ETG-Scale Turbulence*, Nucl. Fusion **52**, 23003 (2012).

[52] F. Sommer, J. Stober, C. Angioni, E. Fable, M. Bernert, A. Burckhart, V. Bobkov, R. Fischer, C. Fuchs, and R. M. McDermott, *Transport Properties of H-Mode Plasmas with Dominant Electron Heating in Comparison to Dominant Ion Heating at ASDEX Upgrade*, Nucl. Fusion **55**, 33006 (2015).

[53] M. Yoshida, G. R. McKee, M. Murakami, B. A. Grierson, M. Nakata, E. M. Davis, A. Marinoni, M. Ono, T. L. Rhodes, C. Sung, L. Schmitz, C. C. Petty, J. R. Ferron, F. Turco, A. M. Garofalo, C. T. Holcomb, C. M. Collins, and W. M. Solomon, *Magnetic Shear Effects on Plasma Transport and Turbulence at High Electron to Ion Temperature Ratio in DIII-D and JT-60U Plasmas*, Nucl. Fusion

57, (2017).

[54] M. Nakata, M. Honda, M. Yoshida, H. Urano, M. Nunami, S. Maeyama, T. H. Watanabe, and H. Sugama, *Validation Studies of Gyrokinetic ITG and TEM Turbulence Simulations in a JT-60U Tokamak Using Multiple Flux Matching*, Nucl. Fusion **56**, (2016).

[55] T. H. Watanabe and H. Sugama, *Velocity-Space Structures of Distribution Function in Toroidal Ion Temperature Gradient Turbulence*, Nucl. Fusion **46**, 24 (2006).

[56] K. Obrejan, K. Imadera, J. Li, and Y. Kishimoto, *Development of a New Zonal Flow Equation Solver by Diagonalisation and Its Application in Non-Circular Cross-Section Tokamak Plasmas*, Comput. Phys. Commun. **216**, 8 (2017).

[57] K. Imadera, J. Lin, D. Nakajima, and Y. Kishimoto, *Study of Plasma Shaping E Ff Ects on ITG Instability Using Global Gyrokinetic Code GKNET with Analytical Magnetic Equilibrium ∗)*, **15**, 1 (2020).

[58] W. Horton, *Turbulent Transport in Magnetized Plasmas* (World Scientific Publishing Co., 2012).

[59] J. Y. Kim and H. S. Han, *Linear Interaction and Relative Role of the Ion Temperature Gradient and Trapped Electron Modes in the Reactor-Relevant Finite Beta Plasma Condition*, Phys. Plasmas **24**, (2017).

[60] Y. Idomura, S. Tokuda, and Y. Kishimoto, *Global Gyrokinetic Simulation of Ion Temperature Gradient Driven Turbulence in Plasmas Using a Canonical Maxwellian Distribution*, Nucl. Fusion **43**, 234 (2003).

[61] M. K. Han, Z.-X. Wang, J. Q. Dong, and H. Du, *Multiple Ion Temperature Gradient Driven Modes in Transport Barriers*, Nucl. Fusion **57**, 046019 (2017).

[62] A. M. Dimits, G. Bateman, M. A. Beer, B. I. Cohen, W. Dorland, G. W. Hammett, C. Kim, J. E. Kinsey, M. Kotschenreuther, A. H. Kritz, L. L. Lao, J. Mandrekas, W. M. Nevins, S. E. Parker, A. J. Redd, D. E. Shumaker, R. Sydora, and J. Weiland, *Comparisons and Physics Basis of Tokamak Transport Models and Turbulence Simulations*, Phys. Plasmas **7**, 969 (2000).

[63] T. Goerler, X. Lapillonne, S. Brunner, T. Dannert, F. Jenko, F. Merz, and D.

Told, *The Global Version of the Gyrokinetic Turbulence Code GENE*, J. Comput. Phys. **230**, 7053 (2011).

[64] T. Tajima and K. Shibata, *Plasma Astrophysics*, 1st ed. (CRC Press, 2018).

[65] J. Wesson and D. J. Campbell, *Tokamaks*, 3rd ed. (Oxford university press, New York, 2004).

[66] J. Y. Kim, Y. Kishimoto, W. Horton, and T. Tajima, *Kinetic Resonance Damping Rate of the Toroidal Ion Temperature Gradient Mode*, Phys. Plasmas **1**, 927 (1994).

[67] J. W. Connor, R. J. Hastie, and J. B. Taylor, *Shear, Periodicity, and Plasma Ballooning Modes*, Phys. Rev. Lett. **40**, 396 (1978).

[68] Y. Kishimoto, T. Tajima, W. Horton, M. J. LeBrun, and J. Y. Kim, *Theory of Self-Organized Critical Transport in Tokamak Plasmas*, Phys. Plasmas **3**, 1289 (1996).

[69] Y. Koide, M. Kikuchi, M. Mori, S. Tsuji, S. Ishida, N. Asakura, Y. Kamada, T. Nishitani, Y. Kawano, and T. Hatae, *Internal Transport Barrier on Q= 3 Surface and Poloidal Plasma Spin up in JT-60U High-β p Discharges*, Phys. Rev. Lett. **72**, 3662 (1994).

[70] Y. Kamada, R. Yoshino, M. Nagami, and T. Ozeki, *Effect of the Q= 1 Surface and Sawtooth Activity on Pressure Profiles and Energy Confinement in Pellet Fuelled JT-60 Limiter Plasmas*, Nucl. Fusion **31**, 23 (1991).

[71] A. Becoulet, L.-G. Eriksson, Y. F. Baranov, D. N. Borba, C. D. Challis, G. D. Conway, V. Fuchs, C. Gormezano, C. W. Gowers, and N. C. Hawkes, *Performance and Control of Optimized Shear Discharges in JET*, Nucl. Fusion **40**, 1113 (2000).

[72] S. Ishida, T. Fujita, H. Akasaka, N. Akino, K. Annou, T. Aoyagi, T. Arai, K. Arakawa, N. Asakura, and M. Azumi, *Achievement of High Fusion Performance in JT-60U Reversed Shear Discharges*, Phys. Rev. Lett. **79**, 3917 (1997).

[73] T. Fujita, S. Ide, H. Shirai, M. Kikuchi, O. Naito, Y. Koide, S. Takeji, H. Kubo, and S. Ishida, *Internal Transport Barrier for Electrons in JT-60U Reversed Shear Discharges*, Phys. Rev. Lett. **78**, 2377 (1997).

[74] K. Ida and T. Fujita, *Internal Transport Barrier in Tokamak and Helical Plasmas*, Plasma Phys. Control. Fusion **60**, (2018).

[75] E. Joffrin, C. D. Challis, T. C. Hender, D. F. Howell, and G. T. A. Huysmans, *MHD Internal Transport Barrier Triggering in Low Positive Magnetic Shear Scenarios in JET*, Nucl. Fusion **42**, 235 (2002).

[76] Y. Kishimoto, J.-Y. Kim, W. Horton, T. Tajima, M. J. LeBrun, S. A. Dettrick, J. Q. Li, and S. Shirai, *Discontinuity Model for Internal Transport Barrier Formation in Reversed Magnetic Shear Plasmas*, Nucl. Fusion **40**, 667 (2000).

[77] A. You, M. A. Y. Be, and I. In, *Resistive '" Infernal "' Modes*, **798**, (2007).

[78] J. W. Connor, R. J. Hastie, and J. B. Taylor, *Shear, Periodicity, and Plasma Ballooning Modes*, Phys. Rev. Lett. **40**, 396 (1978).

[79] W. Wang, Y. Kishimoto, K. Imadera, H. R. Liu, J. Q. Li, M. Yagi, and Z. X. Wang, *Statistical Study for ITG Turbulent Transport in Flux-Driven Tokamak Plasmas Based on Global Gyro-Kinetic Simulation*, Nucl. Fusion **60**, (2020).

[80] M. Kotschenreuther, G. Rewoldt, and W. M. Tang, *Comparison of Initial Value and Eigenvalue Codes for Kinetic Toroidal Plasma Instabilities*, Comput. Phys. Commun. **88**, 128 (1995).

[81] M. J. Pueschel, M. Kammerer, and F. Jenko, *Gyrokinetic Turbulence Simulations at High Plasma Beta*, Phys. Plasmas **15**, (2008).

[82] A. Ishizawa, S. Maeyama, T. H. Watanabe, H. Sugama, and N. Nakajima, *Electromagnetic Gyrokinetic Simulation of Turbulence in Torus Plasmas*, J. Plasma Phys. **81**, (2015).

[83] A. Ishizawa, Y. Kishimoto, and Y. Nakamura, *Multi-Scale Interactions between Turbulence and Magnetic Islands and Parity Mixture—a Review*, Plasma Phys. Control. Fusion **61**, 54006 (2019).

[84] C. Wahlberg and J. P. Graves, *Stability Analysis of Internal Ideal Modes in Low-Shear Tokamaks*, Phys. Plasmas **14**, 110703 (2007).

[85] D. Brunetti, J. P. Graves, W. A. Cooper, and C. Wahlberg, *Fast Growing Resistive Two Fluid Instabilities in Hybrid-like Tokamak Configuration*, Plasma

Phys. Control. Fusion **56**, 75025 (2014).

[86] L. E. Zakharov, *The Theory of Hydromagnetic Stability of a Tokamak Plasma*, Nucl. Fusion **18**, 335 (1978).

[87] P. J. Schmid, *Dynamic Mode Decomposition of Numerical and Experimental Data*, J. Fluid Mech. **656**, 5 (2010).

[88] Ö. D. Gürcan, X. Garbet, P. Hennequin, P. H. Diamond, A. Casati, and G. L. Falchetto, *Wave-Number Spectrum of Drift-Wave Turbulence*, Phys. Rev. Lett. **102**, 255002 (2009).

[89] L. Jiquan and Y. Kishimoto, *Wave-Number Spectral Characteristics of Drift Wave Micro-Turbulence with Large-Scale Structures*, Plasma Sci. Technol. **13**, 297 (2011).

Scientific Contributions

Published paper

1) Z. H. Qin, K. Imadera, J. Q. Li and Y. Kishimoto , Global gyrokinetic simulation of linear micro-instability using parameters referring to HL-2A plasma with ion transport barrier, Plasma and Fusion Research 13, 3403083 (2018).

2) M. Jiang, Y. Xu, W. Chen, Z. B. Shi, J. Q. Li, W. X. Wang, Z. H. Qin, X. T. Ding, W. L. Zhong, X. Q. Ji, P. W. Shi, Z. C. Yang, B. S. Yuan, Y. Liu, Q. W. Yang, and M. Xu, Localized Modulation of Turbulence by m/n = 1/1 Magnetic Islands in the HL-2A Tokamak, Nucl. Fusion 59, (2019).

Paper in proceeding

1) Zhihao Qin, Kenji Imadera, Akihiro Ishizawa, Yasuaki Kishimoto, Regrouped discrete dispersion and associated turbulence in nearly zero magnetic shear toroidal plasmas (submitted to Physical Review Letters)

2) Zhihao Qin, Kenji Imadera, and Yasuaki Kshimoto, Global Gyrokinetic Simulation of Linear Micro-scale Instability Referring the Parameters of HL-2A Plasmas with Anisotropic Temperature (plan to submit to Physics of Plasmas)

Presentation at academic conference

1) Z. H. Qin, K. Imadera, A. Ishizawa, J.Q Li, Y. Kishimoto, “Effect of Magnetic Shear on Electromagnetic Instability and Turbulence in Global Toroidal System”, Japan-China Seminar, Jun. 18, 宇治 (Oral)

2) Z. H. Qin, K. Imadera, A. Ishizawa, Y. Kishimoto, “Finite-beta Effect on Linear Micro-instability in HL-2A Tokamak Plasmas with Anisotropic Temperature”, 第 36 回 プラズマ・核融合学会 年会, Nov. 29 –Dec. 2, 2019, 春日井 (Oral)

3) Z. H. Qin, K. Imadera, A. Ishizawa, Y. Kishimoto. “Beta Effect on Linear Micro-instability in HL-2A Tokamak Plasmas with Anisotropic Temperature”, 25th NEXT workshop, 8-9, Aug. 2019 (Oral)

4) Z. H. Qin, K. Imadera, J. Q. Li and Y. Kishimoto, “Global Gyrokinetic Simulation of Linear Micro-scale Instability in HL-2A Tokamak Plasmas with Anisotropic Temperature”, 第 22 回 若手科学者によるプラズマ研究会, Mar. 18 – 20, 2019, 那珂 (Oral)

5) Z. H. Qin, K. Imadera, K. Yoshida, J. Q. Li and Y. Kishimoto, “Global gyrokinetic simulation of linear micro-scale instability in HL-2A tokamak plasma with NBI/ECRH heating”, Ajou-Kyoto-Zhejiang Joint Symposium on Energy Science, Jan. 17 – 19, 2019, Ajou, Korea (Poster)

6) Z. H. Qin, K. Imadera, J. Q. Li and Y. Kishimoto, “Global gyrokinetic simulation of linear micro-scale instability in density-peaked plasma with NBI/ECRH heating”, 1st Japan-India Bilateral Symposium on Energy and Environmental Science, Dec 2 – Dec. 5, 2018, Bangalore, India (Poster)

7) Z. H. Qin, K. Imadera, J. Q. Li and Y. Kishimoto, “Global Gyrokinetic Simulation of Micro-scale Instability and Turbulence in Density-peaked Plasma with Ion Transport Barrier”, 24th NEXT workshop, 8-10, Aug. 2018 , 三沢 (Oral)

8) Z. H. Qin, K. Imadera, K. Yoshida, J. Q. Li and Y. Kishimoto, “Global Gyrokinetic Simulation of Micro-scale Instability and Turbulence in Density-peaked Plasma”, 第 12 回核融合エネルギー連合講演会, 2018.6.28-6.29 ピアザ淡海 (滋賀県立県民交流センター) (Poster)

9) Z. H. Qin, K. Imadera, K. Yoshida, J. Q. Li and Y. Kishimoto, “Global gyrokinetic simulation of linear micro-scale ITG/TEM instability in HL-2A tokamak plasmas with NBI/ECRH heating”, 73rd 日本物理学会(73 JPS), Mar 22 - Mar 25, 2018 , Tokyo, Japan (Oral)

10) Z. H. Qin, K. Imadera, J. Q. Li and Y. Kishimoto, “Global gyrokinetic simulation of linear micro-instability using parameters referring to HL-2A plasma with ion transport barrier”, 23rd NEXT workshop, Feb 28 - Mar 1, 2018 , Kyoto, Japan (Oral)

11) Z. H. Qin, K. Imadera, J. Q. Li and Y. Kishimoto, “Global gyrokinetic simulation of linear micro-instability in HL-2A tokamak plasmas with ion transport barrier”, 26th International Toki Conference (ITC), 5-8 Dec. 2017, Toki, Japan (Poster)